Jagiellonian University
Marian Smoluchowski Institute of Physics
Department of Solid State Physics

Tuning electronic properties of transition metal oxides at nanoscale by means of redox processes

Doctoral thesis
submitted by

Karol Cieślik

supervised by:
prof. Franciszek Krok

Kraków, 2022

Wydział Fizyki, Astronomii i Informatyki Stosowanej
Uniwersytet Jagielloński

Oświadczenie

Ja niżej podpisany Karol Cieślik (nr indeksu: .....) doktorant Wydziału Fizyki, Astronomii i Informatyki Stosowanej Uniwersytetu Jagiellońskiego oświadczam, że przedłożona przeze mnie rozprawa doktorska pt. „Tuning electronic properties of transition metal oxides at nanoscale by means of redox processes" jest oryginalna i przedstawia wyniki badań wykonanych przeze mnie osobiście, pod kierunkiem prof. dr. hab. Franciszka Kroka. Pracę napisałem samodzielnie.

Oświadczam, że moja rozprawa doktorska została opracowana zgodnie z Ustawą o prawie autorskim i prawach pokrewnych z dnia 4 lutego 1994 r. (Dziennik Ustaw 1994 nr 24 poz. 83 wraz z późniejszymi zmianami).

Jestem świadom, że niezgodność niniejszego oświadczenia z prawdą ujawniona w dowolnym czasie, niezależnie od skutków prawnych wynikających z ww. ustawy, może spowodować unieważnienie stopnia nabytego na podstawie tej rozprawy.

....

Kraków, dnia Podpis autora pracy

Acknowledgements

First and foremost, I would like to express my gratitude to Professor Franciszek Krok for all the years he has been my supervisor. Prof. Franciszek Krok has supported me in my academic journey. Whenever I had a problem, be it experimental or bureaucratic, he would have the solution. He helped me develop as a researcher and nurtured my passion and appreciation for physics, for which I am very grateful.

I would like to thank Dr. Dominik Wrana for many long, helpful discussions and for motivating me to pursue redox processes in transition metal oxides as my field of study. I am grateful to Dr. Benedykt Jany for teaching me about the principles of electron microscopy, and for showing me the ways in which data can be analyzed using machine-learning algorithms. I would also like to extend my thanks to Dr. Maciej Rogala, Dr. Christian Rodenbücher, Dr. Paweł Dąbczyński, Professor Jakub Rysz and Professor Kristof Szot for their help and collaboration during the writing of my first publication. For providing me with TEM measurements, I am grateful to Dr. Oleksandr Kryshtal. For making the investigations into the photocatalytic properties of TiO_2 powders possible, I would like to thank Marta Macyk, Dr. Joanna Kuncewicz and Professor Wojciech Macyk.

I would also like to extend my thanks to my colleagues: Wojciech Bełza, Dr. Konrad Szajna, Dr. Arkadiusz Janas, Marta Macyk, Piotr Popek and Janusz Ryrych for their help in the laboratory and for making it such a pleasant place to work in. I am thankful to the members of the Solid State Department, headed by Professor Rafał Abdank-Kozubski, for the pleasant and friendly atmosphere.

My sincere thanks go to my friends from university, Dariusz Augustowski and Sebastian Zieliński, for encouraging me to pursue my interests no matter the difficulties.

I would also like to thank Krystian Aparta for providing me with valuable suggestions and comments, which greatly improved the quality of this dissertation.

I am extremely grateful to my parents, Urszula and Waldemar, my sister Paulina, and my beloved Amna for their unwavering support, encouragement and kindness. Without you, I would have never finished this dissertation.

Podziękowania

Przede wszystkim chciałbym podziękować profesorowi Franciszkowi Krokowi wieloletnie wspieranie mnie w roli promotora. Prof. Franciszek Krok zawsze okazywał mi wsparcie podczas studiów i doktoratu. Gdy napotykałem problem, czy to w laboratorium czy poza nim, Prof. Krok znajdował rozwiązanie. Dzięki niemu stałem się lepszym naukowcem i rozwinąłem swoje zainteresowania w dziedzinie fizyki.

Chciałbym podziękować Dr. Dominikowi Wranie za długie, pomocne dyskusje i za zainteresowanie mnie tematem procesów redoks w tlenkach metali przejściowych. Jestem wdzięczny Dr. Benedyktowi Janemu za wtajemniczenie mnie w techniki mikroskopii elektronowej i pokazanie mi, jak można analizować dane algorytmami uczenia maszynowego. Chciałbym również podziękować Dr. Maciejowi Rogali, Dr. Christianowi Rodenbücherowi, Dr. Pawłowi Dąbczyńskiemu, Prof. Jakubowi Ryszowi i Prof. Krzysztofowi Szotowi za ich pomoc i współpracę podczas pisania mojej pierwszej publikacji. Za wykonanie pomiarów TEM jestem wdzięczny Dr. hab. Oleksandrowi Kryshatalowi. Za umożliwienie dokonania pomiarów właściwości fotokatalitycznych proszków TiO_2, chciałbym podziękować Marcie Macyk, Dr. Joannie Kuncewicz i Prof. Wojciechowi Macykowi.

Chciałbym podziękować także współpracownikom: Wojciechowi Bełzie, Dr. Konradowi Szajnie, Dr. Arkadiuszowi Janasowi, Marcie Macyk, Piotrowi Popkowi i Januszowi Ryrychowi za pomoc w pracy laboratoryjnej i za zapewnienie przyjemnych warunków pracy. Dziękuję również członkom Zakładu Fizyki Ciała Stałego, na czele z Prof. Rafałem Abdankiem-Kozubskim, za miłą i przyjazną atmosferę.

Dziękuję przyjaciołom z czasów studiów, Dariuszowi Augustowskiemu i Sebastianowi Zielińskiemu, za zachęcanie mnie, żebym podążał za swoimi pasjami bez względu na napotykane problemy.

Chciałbym podziękować Krystianowi Aparcie za cenne uwagi i komentarze, które polepszyły jakość tej pracy doktorskiej.

Jestem dozgonnie wdzięczny moim rodzicom, Urszuli i Waldemarowi, siostrze Paulinie i mojej ukochanej Amnie za ich ciągłe wsparcie i życzliwość. Bez Was nigdy bym nie skończył tej pracy.

Abstract

The climate crisis that we are facing has galvanized the scientific and engineering communities and has led to the rapid development of new, efficient, environmentally-friendly devices. One of the most promising classes of materials for such applications are transition metal oxides. This is due to the fact that by controlling the oxygen content in these crystals by means of reduction and oxidation, the material properties can be tuned in a wide range of values. Thus, the transition metal oxides, such as the model crystals, titanium dioxide (TiO_2) and strontium titanate ($SrTiO_3$), find use in so many different fields, from photocatalysis, to energy storage (solid oxide fuel cells), information technology (memristors) and even healthcare (antibacterial films).

This PhD thesis is an investigation into the effect of reduction and oxidation on the electronic properties of transition metal oxides. These processes were studied at nanoscale using a multitude of techniques to provide a thorough characterization of the changes that occur in the studied systems, i.e. TiO_2 and $SrTiO_3$. Moreover, the experiments were performed in both ultra high vacuum (UHV) conditions, as well as in oxygen, and even in atmospheric air, in order to comprehensively describe the changes in properties and to bring the results closer to applications. The goal of the dissertation was to study the evolution of the electronic properties, i.e. the work function and conductivity, due to redox processes, and to add to the general understanding of these processes.

The experiments revealed that the electronic properties may be tuned. In case of using reduction by means of annealing in UHV, ion sputtering, and repeated ion sputtering and annealing, and for oxidation by exposure to oxygen or air at room temperature, and annealing in oxygen. Using this range of methods, the conductivity of TiO_2 can be changed from semiconductive-like to metallic-like. Furthermore, the work function of the transition metal oxides can be tuned in a wide range, from 3.4 eV to 5.0 eV for TiO_2, and from 2.9 eV to 4.5 eV for $SrTiO_3$. This is associated with changes in surface and subsurface composition, crystallography, morphology and even with the growth of new oxide phases.

The key findings in the field of surface science were the description of the changes in electronic properties due to repeated sputtering and annealing, and the presence of oxygen getter substances. These results are important, because they touch upon the very basis of every experiment in the field, i.e. the preparation of crystals. This work can be used to foster greater reproducibility of experiments, as well to provide new means of designing experiments.

Another object of the study was the technologically interesting system of conductive nanowires on semiconductive $SrTiO_3$ substrate. It was shown that the nanostructures are composed of a TiO core covered with a layer of Ti_3O_5. The evolution of the system, starting from atomically flat strontium titanate, through nanowire-covered substrate to a crystal with a layer of porous titanium suboxides was described. The effect of annealing in oxygen on wire-covered surface was been investigated.

Streszczenie

Panujący kryzys klimatyczny pobudził środowisko naukowe do szybkiego opracowywania nowych, sprawnych oraz przyjaznych dla środowiska urządzeń. Jedną z najbardziej obiecujących klas materiałów w kontekście takich zastosowań są tlenki metali przejściowych. Jest tak dlatego, że wykorzystując procesy redukcji i utleniania można kontrolować zawartość tlenu w takich kryształach, a w konsekwencji ich właściwości fizyczne. W związku z tym tlenki metali przejściowych, takie jak modelowe kryształy, ditlenek tytanu (TiO_2) i tytanian strontu ($SrTiO_3$), znajdują zastosowanie w wielu dziedzinach, od fotokatalizy, przez technologie magazynowania energii (ogniwa paliwowe ze stałym tlenkiem) i informacji (memrystory), po nawet służbę zdrowia (warstwy antybakteryjne).

Przedmiotem tej pracy doktorskiej jest badanie wpływu redukcji i utleniania na właściwości elektronowe tlenków metali przejściowych. Procesy te badano w nanoskali wykorzystując szereg technik pozwalających na kompleksowy opis zmian zachodzących w badanych układach – TiO_2 i $SrTiO_3$. Co więcej, eksperymenty były przeprowadzane w ultra wysokiej próżni, tlenie, a nawet powietrzu, w celu wszechstronnego opisu zachodzących zmian i przybliżenia wyników do zastosowań. Celem tej pracy było zbadanie zmian elektronowych właściwości, pracy wyjścia i przewodnictwa, pod wpływem procesów redoks.

W pracy pokazano, że właściwości elektronowe można zmieniać, w przypadku redukcji poprzez wygrzewanie w próżni, bombardowanie jonowe, naprzemienne bombardowanie jonowe oraz wygrzewanie, a w przypadku utleniania poprzez ekspozycję na tlen lub powietrze w temperaturze pokojowej oraz wygrzewanie w tlenie. Wykorzystując ten wachlarz metod, przewodnictwo TiO_2 można zmienić z przewodnictwa półprzewodnikowego do metalicznego. Co więcej, pracę wyjścia tlenków metali przejściowych można dostosowywać w szerokim zakresie, od 3.4 eV do 5.0 eV w przypadku TiO_2 oraz od 2.9 eV do 4.5 eV w przypadku $SrTiO_3$. Wymienione zmiany są związane ze zmianą powierzchni i obszaru pod powierzchnią, krystalografii i morfologii, a nawet ze wzrostem nowych faz tlenkowych.

Głównymi osiągnięciami w zakresie fizyki powierzchni są opisy zmian właściwości elektronowych w wyniku naprzemiennego bombardowania i wygrzewania oraz wygrzewania w obecności, lub w braku substancji obniżających ciśnienie parcjalne tlenu. Te odkrycia są istotne, ponieważ dotyczą podstaw każdego eksperymentu z tej dziedziny, czyli przygotowania kryształów. Wyniki tej pracy mogą być wykorzystane w celu osiągnięcia większej powtarzalności eksperymentów oraz w projektowaniu nowych eksperymentów.

W pracy opisane są eksperymenty przeprowadzone na układzie składającym się z przewodzących nanodrutów na półprzewodnikowej powierzchni $SrTiO_3$. Wykazano, że badane nanostruktury składają się ze rdzenia TiO pokrytego powłoką Ti_3O_5. Została opisana ewolucja układu od atomowo płaskiego tytanianu strontu, poprzez pokrytego nanodrutami substratu $SrTiO_3$ aż do kryształu pokrytego porowatą warstwą podtlenków tytanu. Dodatkowo zbadano wpływ wygrzewania w tlenie.

Acronyms

AES Auger electron spectroscopy

AFM Atomic force microscopy

CC Cleaning cycle

CPD Contact potential difference

EBSD Electron backscattered diffraction

EDX Energy-dispersive X-ray spectroscopy

EELS Electron energy loss spectroscopy

ELOP Extremely low oxygen partial pressure

FFT Fast Fourier transform

HAADF STEM High-angle annular dark field imaging scanning transmission electron microscopy

HOPG Highly oriented pyrolytic graphite

KPFM Kelvin probe force microscopy

LC-AFM Local-conductivity atomic force microscopy

LEED Low-energy electron diffraction

ML Monolayer

RMS Root mean square

RT Room temperature

SEM Scanning electron microscopy

SIMS Secondary ion mass spectrometry

SPM Scanning probe microscopy

STM Scanning tunneling microscope

TEM Transmission electron microscope

UHV Ultra high vacuum

XPS X-ray photoelectron spectroscopy

Contents

Acknowledgements **i**

Podziękowania **ii**

Abstract **iii**

Streszczenie **iv**

Acronyms **v**

1 Introduction **1**

1.1 Thesis structure . . . 1
1.2 Motivations . . . 2
1.3 Transition metal oxides . . . 3
1.3.1 Titanium dioxide (TiO_2) . . . 3
1.3.2 Strontium titanate ($SrTiO_3$) . . . 4
1.3.3 Titanium suboxides (Ti_nO_{2n-1}) . . . 6
1.4 Defects in oxides . . . 7
1.4.1 0-dimensional . . . 7
1.4.2 1-dimensional . . . 7
1.4.3 2-dimensional . . . 9
1.4.4 3-dimensional . . . 9
1.5 Reduction of transition metal oxides . . . 10
1.5.1 Thermal reduction . . . 11
1.5.2 Extremely low oxygen partial pressure (ELOP) . . . 12
1.5.3 Sputtering . . . 12
1.5.4 Sputtering and annealing . . . 13
1.6 Oxidation of transition metal oxides . . . 14
1.7 Application of TiO_2 in photocatalysis . . . 15

2 Analytical methods **17**

2.1 Scanning probe microscopy (SPM) . . . 17
2.1.1 Scanning tunneling microscope (STM) . . . 17
2.1.2 Atomic force microscopy (AFM) . . . 19
2.2 Scanning electron microscopy (SEM) . . . 21
2.2.1 Energy-dispersive X-ray spectroscopy (EDX) . . . 23
2.2.2 Electron backscattered diffraction (EBSD) . . . 23
2.3 Low-energy electron diffraction (LEED) . . . 24
2.4 Auger electron spectroscopy (AES) . . . 26

2.5 X-ray photoelectron spectroscopy (XPS) . . . 27
2.6 Transmission electron microscope (TEM) . . . 28
2.7 Electron energy loss spectroscopy (EELS) . . . 29
2.8 Secondary ion mass spectrometry (SIMS) . . . 30

3 Experimental **33**
3.1 Methods of annealing the samples in ultra high vacuum (UHV) . . . 33
3.1.1 Electrical current through a sample . . . 33
3.1.2 Electron beam holder . . . 34
3.1.3 Quartz tube and Knudsen cell . . . 35
3.2 Methods of sample oxidation . . . 36
3.2.1 Oxidizing in UHV conditions . . . 37
3.2.2 Oxidizing by exposure to air . . . 37
3.2.3 Summary of the annealing methods . . . 37
3.3 Monocrystal preparation . . . 39
3.4 KPFM calibration procedure . . . 39

4 Goals of the thesis **41**

5 The effect of annealing on the electronic properties of TiO_2 **42**
5.1 Changes induced by annealing in UHV . . . 42
5.1.1 Experimental . . . 42
5.1.2 Changes in morphology and crystallography . . . 42
5.1.3 Changes in chemical composition . . . 45
5.1.4 Changes in electronic properties . . . 46
5.2 Oxidation of reduced TiO_2 at room temperature . . . 49
5.2.1 Experimental . . . 49
5.2.2 The effect of oxidation on electronic properties . . . 49

6 The effect of repeated sputtering and annealing on the electronic properties of TiO_2 **51**
6.1 Changes induced by sputtering . . . 51
6.1.1 Experimental . . . 51
6.1.2 Morphology of the sputtered crystal . . . 52
6.1.3 Chemical composition of the sputtered crystal . . . 53
6.1.4 Changes in electronic properties due to sputtering . . . 54
6.2 Changes induced by sputtering and annealing . . . 57
6.2.1 Experimental . . . 57
6.2.2 Changes to morphology . . . 58
6.2.3 Changes to stoichiometry . . . 58
6.2.4 Changes to electronic properties . . . 59
6.3 Changes induced by repeated sputtering and annealing . . . 60
6.3.1 Experimental . . . 60

6.3.2 Changes in morphology with the increase in the number of CCs 61
6.3.3 Changes in chemical composition with the increase in the number of CCs 63
6.3.4 Changes in electronic properties with the increase in the number of CCs 66
6.3.5 One large cycle or multiple small cycles: the effect on electronic properties 67
6.4 The effect of subsequent oxidation of a sample after 50 CCs 69

7 The effect of thermal annealing on $SrTiO_3$ crystals 71
7.1 Changes occurring on the surfaces of flat $SrTiO_3$ as a function of temperature with or without a getter 71
7.1.1 Experimental 71
7.1.2 Morphology and crystallography of the surfaces 72
7.1.3 Work function of the surfaces 74
7.2 Growth of nanowires on $SrTiO_3$ during annealing in UHV 75
7.2.1 Experimental 76
7.2.2 Crystallographic and chemical composition of the nanowires 76
7.2.3 The relationship between annealing temperature and morphology of nanowire-covered $SrTiO_3$ 79
7.2.4 Chemical composition of the suboxide layer grown on $SrTiO_3$ 80
7.3 Changes in electronic properties of the nanowire-covered $SrTiO_3$ surface after exposure to oxygen or air at RT 81
7.3.1 Experimental 81
7.3.2 The electronic properties of the nanowires on $SrTiO_3$ substrate 82
7.3.3 The effect of oxygen exposure at RT on the electronic properties of the nanowires on the $SrTiO_3$ substrate 83
7.3.4 The effect of air exposure at RT on the electronic properties of the nanowires on the $SrTiO_3$ substrate 85

8 Changes induced by annealing in oxygen on the nanowire-covered $SrTiO_3$ surface 87
8.1 Growth of structures on the nanowire-covered $SrTiO_3$ due to oxidation 87
8.1.1 Experimental 87
8.1.2 Changes in morphology 88
8.1.3 Changes in the structure and composition of the nanostructures 89
8.1.4 The electronic properties of the structures grown during oxidation . . . 94

9 Conclusions 98

Bibliography 102

Appendix: Academic achievements 122

Chapter 1

Introduction

1.1 Thesis structure

This dissertation is an investigation into the electronic properties of transition metal oxides at nanoscale and how they change as a result of reduction and oxidation. The research was performed on two systems, titanium dioxide (TiO_2) and strontium titanate ($SrTiO_3$). Each of the crystals was described in two chapters.

- Chapter 1 – **Introduction**
  This chapter contains a description of the investigation, the motivations, crystals which were studied and defects which occur in them, the processes of reduction and oxidation, as well as one of the applications (photocatalysis).
- Chapter 2 – **Analytical methods**
  The chapter outlines the techniques used to characterize the changes in the crystals.
- Chapter 3 – **Experimental**
  This part of the dissertation describes the annealing methods which were used in the experiments, as well as the preparation methods of the monocrystals, and the calibration procedure used with KPFM.
- Chapter 4 – **Goals of the thesis**
  In this chapter the research objectives of the dissertation are presented.
- Chapter 5 – **The effect of annealing on the electronic properties of TiO_2**
  This chapter contains the description of the effects of annealing on TiO_2 electronic properties as well as composition. The changes due to subsequent oxidation at room temperature on the properties are also presented.
- Chapter 6 - **The effect of repeated sputtering and annealing on the electronic properties of TiO_2**
  This chapter is dedicated to describing the changes in electronic properties of TiO_2 during reduction by sputtering, and by repeated sputtering and annealing. The effects of subsequent oxidation are also presented.
- Chapter 7 – **The effect of thermal annealing on $SrTiO_3$ crystals**
  The chapter is dedicated to describing the changes which occur at the surface of $SrTiO_3$ as a result of thermal annealing at the stage where reduction is the dominant process and at the stage where incongruent effusion and growth of nanostructures also occurs. The effect of partial oxygen pressure on electronic properties is studied. The growth and properties of nanostructures is also described. Moreover, in all cases, the investigation also includes the changes due to oxidation at RT.
- Chapter 8 - **The changes induced by annealing in oxygen on the nanowire-**

covered $SrTiO_3$ surface
The changes in morphology and properties of nanowire-covered strontium titanate due to annealing in oxygen are investigated. The evolution of the chemical composition as the result of this process is described.

- Chapter 9 - **Conclusions**
  This chapter contains the conclusions.
- Appendix - **Academic achievements**
  The publications and conferences at which the results were presented are listed here.

1.2 Motivations

The climate crisis that humanity is facing right now seems to be the challenge of our times, with potential far-reaching consequences for both the current and future generations. A united global response is needed to tackle this challenge. The required changes are extensive and will not only impact global industries, but also every household. New, more efficient, sustainable technologies and solutions are needed urgently, and this is where science comes to the rescue.

The rapid development of such new technologies relies on many different, promising classes of materials, one of which are transition metal oxides. These materials are the basis of, or a major component of photocatalysts (for hydrogen production from water splitting [1], [2], and the removal of pollutants from air [3], [4], [5], water [6] and soil [7], [8]), solar cells [9], [10], carbon-capture technologies [11], solid oxide fuel cells [12], supercapacitors [13], energy-efficient memristor storage and neuromorphic computing devices [14], [15]. They are also used in fields not directly related to climate change, such as to global health, owing to their antibacterial [16],[17] and antiviral [18] properties. Metal oxides are also a subject of basic research, as they exhibit properties such as superconductivity [19], the magnetocaloric effect [20], the piezoresistive effect [21] and thermoelectric properties [22].

The wide application and versatile characteristics of transition metal oxides result from the fact that their properties can be tuned or even changed completely by the control of the oxygen content in the crystal, i.e. by redox processes. Changes in the oxygen content of the crystal lead to changes in the valence state of the transition metal, which depending on the intensity of reduction and oxidation processes, might slightly change the electronic properties of the crystal or lead to its complete rearrangement, in the form of a phase transition (e.g. as Magnéli phase formation in TiO_2). These changes may occur in the total volume of the crystal or just in some parts of it. Even gradients of nonstoichiometry can be introduced by using the appropriate methods [23]. As a general rule, the redox processes are most effective on the surface and where the symmetry of the crystal is broken, i.e. on extended defects, and this is why the surface science perspective is crucial here. The knowledge obtained from basic research allows for the targeted design of applications, while accelerating the development of such applications over a trial-and-error approach. Results of basic research experiments in surface science have already shed light on the processes occurring on photocatalysists [24] and even oxide biomaterials for dentistry applications [25].

This dissertation presents the results of a series of experiments aimed at providing a better

understanding of the reduction and oxidation processes of two model transition metal oxides - titanium dioxide and strontium titanate. While the research was primarily aimed at studying the changes of electronic properties due to the redox processes, a parallel investigation of the changes in compositions and structure of the crystals and its surface was unavoidable.

1.3 Transition metal oxides

Transition metal oxides are a wide category of materials – and this is of no surprise, as oxygen is highly reactive and forms compounds with most elements, transition metals included. These diverse materials can be separated into groups by common denominators, such as the number of elements present in these crystals. The model binary oxide studied in this dissertation, composed of a transition metal and oxygen, is titanium dioxide in the form of rutile. Strontium titanate was selected as a model ternary oxide (composed of a transition metal, another element and oxygen). $SrTiO_3$ is also a model perovskite crystal.

1.3.1 Titanium dioxide (TiO_2)

Titanium dioxide is a ubiquitous compound whose annual production is estimated at 5 and 10 million tonnes [26]. It is mostly used as a pigment for paints, coatings, paper etc. [26], due to its exceptionally high refractive index (2.73 for rutile [27]). Nanoparticles of TiO_2 are used in other fields, such as catalysis and electroceramics, and even in sunscreens [26]. Moreover, the exceptional properties and its easy manipulation makes titanium dioxide an attractive compound for high-tech applications from photocatalysts [1] [5], self-cleaning paints [28], to memristors [14]. It is no wonder that this compound is so intensively studied, to the point that, only in the field of photocatalysis, the number of papers on TiO_2 is close to 14 thousand [29] (till 2020).

Titanium dioxide exists in at least 11 crystalline phases [26], however only two - rutile and anatase - are of significant interest for applications [30]. Rutile is the most thermodynamically stable phase of TiO_2 (as determined by lattice energy calculations [32]), which makes it attractive for research in the field of thermal reduction, as the other viable meta-stable phase - anatase - transforms into rutile at approximately 600 °C in vacuum conditions [33], which is even below the temperature of desorption of organic adsorbates from the crystal surface [34]. A rutile unit cell (Fig. 1.1a) is tetragonal with two atoms per unit cell and the lattice parameters a = 0.4594 nm and c = 0.2959 nm [35]. It has a band gap of approximately 3.1 eV [36], which means that the onset of absorption in a perfectly stoichiometric rutile is in the range of UV light, and the polished, stoichiometric crystal is transparent (Fig. 1.1b). The slight yellowish coloration seen in as-received rutile monocrystals is most likely due to the scattering of light on the unpolished side of the crystal, and not due to the absorption of light, as similar coloration is seen on $SrTiO_3$ one-side polished crystals (see Fig. 1.2), and in both cases, the coloration disappears when the crystals are polished on both sides. In the case of TiO_2, there is some absorption in the violet end of the visible spectrum [37], but it is not intense enough to change the color of polished crystals drastically.

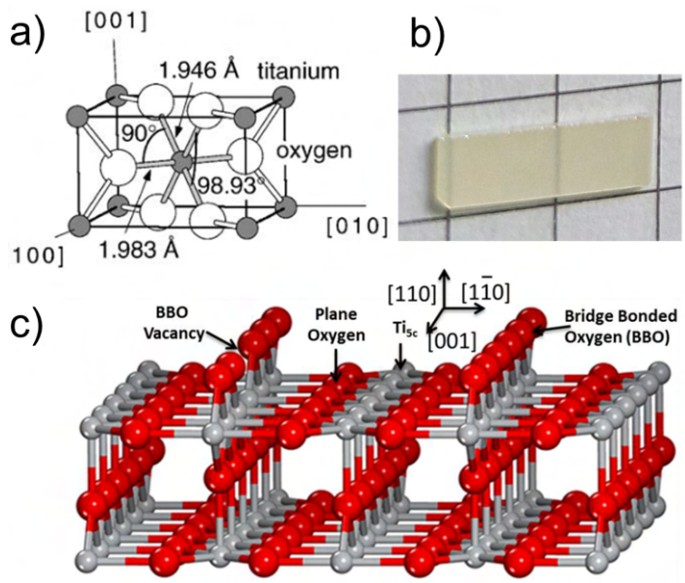

Figure 1.1: a) The tetragonal rutile unit cell [30], b) as-received rutile monocrystal, c) a stick and ball model of rutile (110) surface [31].

The rutile surface studied in this dissertation is its most stable phase [30] the (110). Its stability is due to the fact that the dipole moment perpendicular to the surface is zero, because of the symmetric stacking of differently charged planes [38]. The (110) surface, depicted in Fig. 1.1c), is composed of alternating rows of atoms in the direction [110]. Two types of titanium atom rows can be distinguished - sixfold and fivefold coordinated Ti atoms. The fivefold Ti atoms have one dangling bond perpendicular to the surface, while sixfold Ti atoms have chemical bonding, as in the bulk crystal. Two different types of oxygen atoms are present on the (110) surface - one is three-fold coordinated, as in the bulk crystal, while the other is twofold coordinated and forms sticking-out, bridging oxygen rows with one dangling bond. The unit cell associated with such surface reconstruction, i.e. (1x1), and the one which will be most often observed in this dissertation, has the lattice parameters equal to a = 0.649 nm and b = 0.296 nm [39]. Real-life monocrystals, due to the unavoidable small miscut angle, exhibit vicinal, or terraced, morphology. The terrace sizes depend on the method of preparation, but the terrace step height is due to the crystal morphology and is equal to 0.235 nm [39], which is approximately equal to half a unit cell.

1.3.2 Strontium titanate ($SrTiO_3$)

Strontium titanate first entered the application stage as a diamond substitute in 1951 [40], however its usage has shifted from jewelry applications to sophisticated technologies. This compound can be used as a highly stable electron transport layer in solar cells [41], as a model memristor [42], a high-energy storage device [43], a photocatalyst [44], or in RF circuits [45]. Moreover, $SrTiO_3$ is widely used as a growth substrate of thin films of perovskite materials, including materials exhibiting superconductivity [46], [47]. It is an extensively studied material considered a model perovskite crystal [48], [49], as well as a model ternary oxide [50]. Thousands

of publications have been devoted to its properties [51].

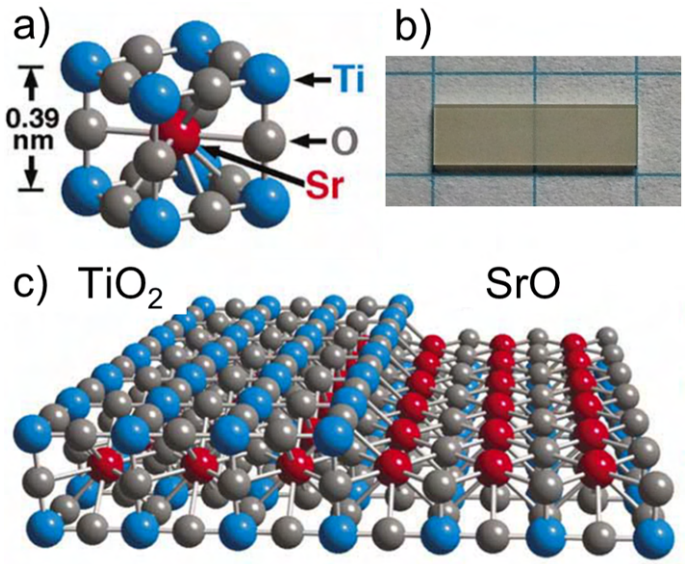

Figure 1.2: a) The unit cell of $SrTiO_3$ in its cubic phase [52], b) as-received $SrTiO_3$ monocrystal, c) its (100) surface with the two possible terminations of strontium titanate marked [53] .

Perovskite materials, a model compound of which is $SrTiO_3$, have a general formula ABO_3, where A is a group I or II element and B is a transition metal. These types of crystals are of enormous interest, as they exhibit properties typical of semiconductors, such as tunable band gaps or light absorption, but can also be tuned structurally, optically and electronically by replacing the A cation with small organic cations, which opens up a promising venue of investigation into organic-inorganic materials [54], [55].

The unit cell of cubic strontium titanate (Fig. 1.2a) has a length 0.3905 nm. It can be considered as a series of TiO_6 octahedrons placed in a strontium lattice. $SrTiO_3$ can also exist in a tetragonal structure, with phase transition occurring at 105 K [56], and orthorhombic below 65 K [57]. In its cubic form, it has a band gap of 3.1 eV [58]. Like TiO_2, it is transparent when polished on both sides, but in the case of one-side polished crystals it has a slight yellowish coloration (Fig. 1.2b) due to scattering of light.

The surface studied in this dissertation is the (100) surface (Fig. 1.2c). The $SrTiO_3$ crystal can be considered as repeating layers of TiO_2 and SrO when looked at <001> directions, both of these layers can form a thermodynamically stable termination of the (100) surface [53]. TiO_2 and SrO terminations, shown schematically in Fig. 1.2c, can coexist on the crystal surface [53]. Properties of these terminations differ, e.g. in work function [59], and some phenomena can only be observed on one of them, e.g. high-mobility electron gas on the $LaAlO_3/SrTiO_3$ interface is present only for the TiO_2 termination [60], and epitaxial growth depends on the termination and even the ratio of the termination area on the surface [61]. It is not surprising that there exist multiple methods of obtaining the TiO_2 [62], [63] or SrO terminations [64], [65].

1.3.3 Titanium suboxides (Ti_nO_{2n-1})

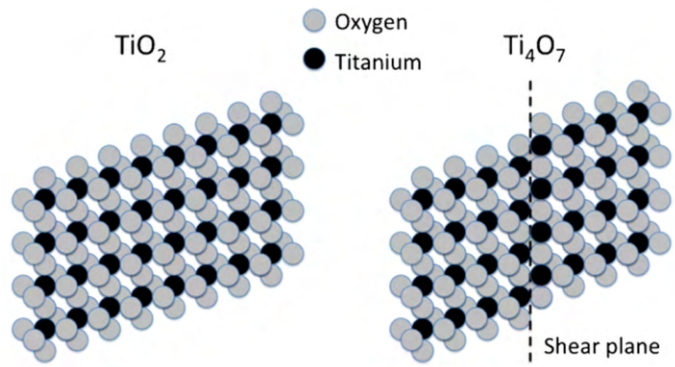

Figure 1.3: The formation of a Magnéli phase Ti_4O_7 by the creation of a shear plane [66].

Transition metal oxides are a fascinating topic for research and applications, because of their ease of modification - one can use redox reactions to change their chemical composition, structure, and therefore their physical and chemical properties. Using redox reactions makes it possible to produce a multitude of titanium suboxides, with a general chemical formula Ti_nO_{2n-1}, and their chemical formula and properties can be tuned to reach the desired results. These suboxides find applications in many fields, from metal-insulator-metal diodes [67] to coatings that increase tribological performance [68]. Titanium suboxides studies are tightly connected with research into TiO_2 and titanates, such as $SrTiO_3$, as redox reactions on these crystals unavoidably lead to the formation of these suboxides.

The easy change in the titanium oxides and titanates offers multitude of possible suboxides that can be formed during the reduction and oxidation of these crystals. The titanium suboxide chemical formula Ti_nO_{2n-1} their properties seamlessly change, for example electrical conductivity can change from semiconducting to metallic [69], and even to superconductive [19]. The evolution of crystallographic and electronic structures is governed by the value of n. The driving force of the changes in the electronic properties is the increasing number of reduced titanium ions Ti^{3+} and even Ti^{2+} in the crystal, which introduces states near the conduction band, which houses easily excitable electrons [30], [70]. The great number of possible suboxides can be seen on the phase diagram of titanium and oxygen [71] and since the upper value of n has been proposed to be 28 [72] or even 99 [73], the property tuning possibilities are significant. Magnéli phases, a subgroup of titanium suboxides of the n value $4 \leqslant n \leqslant 9$, have been studied widely. They are formed from rutile by means of crystalographic shearing, and in their structure every n-th layer of octahedra shares not the corner, but the whole face (which is depicted in Fig. 1.3).

Redox processes generally do not occur uniformly in the whole oxide crystal volume - they are most effective on the surface and near extended defects. This non uniformity of reduction and oxidation gives rise to some of the properties of transition metal oxides. In the cases of $SrTiO_3$ [42] and TiO_2 [74], resistive switching occurs on dislocations, due to the fact that the changes in stoichiometry, and therefore electric properties, occur readily on the defects, in

contrast to the bulk crystal. Furthermore, even pure annealing in vacuum leads to hierarchical changes in the crystal stoichiometry, with most reduced parts (and for heavy reduction phases) occurring at the surface, and increasingly less reduced parts further in to the bulk, where the composition is closest to stoichiometric crystal [74]. Accordingly, the changes in transition metal oxide crystals stoichiometry and structure presented in this dissertation will follow a gradient from the surface where the crystal will be reduced most, to the bulk which will be reduced least.

1.4 Defects in oxides

Crystals are highly ordered objects – enormous numbers of atoms of different elements follow the same pattern, and maintain the same distances between one another, which results in symmetrical macroscopic crystals displaying unusual shapes. Yet most research focuses more on imperfections or defects in the crystal, not their amazing ordered patterns. These imperfections might seem unwelcome for applications and research, but in reality, the defects are crucial for the development of technologies based on transition metal oxides. The ability to easily change the type and density of defects using redox processes is an advantage of transition metal oxides. This section will survey the typical defects, which can be characterized in many ways; the discussion below will define them by their dimensionality, or size.

1.4.1 0-dimensional

Crystal structure is composed of atoms in clearly defined points of the crystallographic lattice. The simplest defects are point defects, i.e. imperfections in this inner order. Such 0-dimensional defects can take many forms. They may constitute a missing atom in a node (i.e. a vacancy), or the presence of an additional atom between nodes (i.e. an interstitial atom or the Frenkel defect), or an atom of a different element, whose presence is not indicated in the general chemical formula (a dopant). Such defects are thermodynamically unavoidable, as they decrease the Gibbs free energy of the crystal. Additionally, their equilibrium concentration is a function of temperature and gas pressures. In general, point defects are responsible for conductivity, color and the diffusional properties of crystals [75]. In the case of transition metal oxides, the key point defects are oxygen vacancies and transition metal interstitials (see Section 1.5). Point defects in transition metal oxides can be considered to be non interacting and randomly distributed in the bulk crystal matrix only up to a point - for $TiO_{2\text{-}x}$ only up to $x = 1 \times 10^{-4}$ [76] and for $SrTiO_{3\text{-}x}$ $x = 1 \times 10^{-3}$ [77] - and then they interact with one another, forming extended defects. The ordering of oxygen vacancies leads to the formation of shear planes, which is considered the first step in the formation of Magnéli phases [78].

1.4.2 1-dimensional

Crystals also exhibit one-dimensional defects, with dislocations being the type most important in the context of oxide crystals. These line defects can be classified into edge and screw dislocations. Edge dislocations can be thought of as an additional half-plane inserted

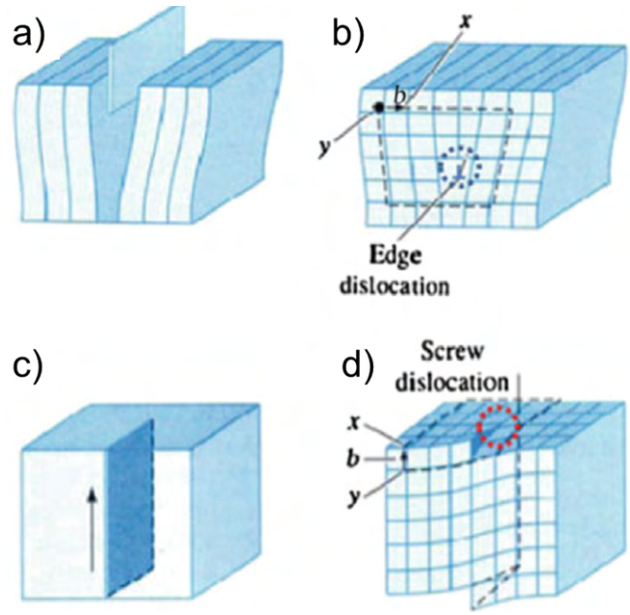

Figure 1.4: Schematic representation of the formation of a-b) edge and c-d) screw dislocations [26].

into the perfect crystal matrix (Fig. 1.4a-b). Screw dislocations, on the other hand, can be described as structures formed when one part of the crystal is sheared with respect to the other one (Fig. 1.4c-d). Such dislocations are described by the Burgers vector, which is a measure of the direction and magnitude of these line defects. These defects in TiO_2 and $SrTiO_3$ form bundles [79], [50], which exhibit a hierarchical structure, with the greatest concentration near the surface and the lowest concentration in the bulk. Dislocations are present in great quantities on TiO_2 and $SrTiO_3$ monocrystal surfaces with approximately $1 \times 10^7\,\mathrm{cm}^{-2}$ for Verneuil-grown crystals [80].

Dislocations are of extreme importance when considering phenomena like memristive switching [42], but they are also of consequence in the context of mechanical deformations. It is due to the movement of dislocations that some crystals break easily while others deform plastically. If the dislocations can move easily, strains do not accumulate and the crystal bends. However, if the dislocations tend to be pinned and to accumulate, the strains will shatter the crystal. The reason behind the problematic cracking in $SrTiO_3$ is the manner in which dislocations behave throughout annealing. Even though the melting temperature of $SrTiO_3$ is very high - 2080 °C, and even though it is considered to be a good material for high-temperature applications [51], the existence of the ductile-to-brittle-to-ductile transition [81] makes it difficult to work with monocrystals at high temperatures. Typically, brittle-to-ductile behavior is observed in ceramics, which are brittle in lower temperatures and ductile at higher temperatures. However, strontium titanate is different. $SrTiO_3$ is ductile at low temperatures, becomes brittle at approximately 1000 K, and subsequently becomes ductile again [57]. The origin of this unusual behavior is not due to any structural changes (as they occur at much lower temperatures), but due to the behavior of dislocations in the crystal [81]. At low temperatures dislocations move by gliding, i.e. the Burgers vector and the dislocation line lie on the same plane [82]. At high temperatures dislocations move by climb planes, i.e.

with the Burgers vector and the dislocation line not on the same plane. In between, there is a transition region, as the change between glide-associated and climb-associated configurations of dislocation has an energy barrier [82]. At these temperatures, the pinning of dislocation occurs, which slows down the movement of dislocations and causes the crystal to become brittle [82], as the dislocations continue to form at the same regions, while their low mobility causes them to concentrate in one location, which significantly increases the internal stress and causes the crystal to shatter at approximately 1050 K in the so-called brittle failure [57]. Hirel et al. (2016) proposed that extremely slow strain rates $SrTiO_3$ could avoid the brittle failure as the dislocations would only move by climb mechanism [82]. The atomistic reason is that strontium vacancies diffuse much slower than oxygen vacancies to dislocations, causing the dislocations to become electrically charged and pinned.

1.4.3 2-dimensional

Defects of higher dimensions can also be found in crystals. The most interesting two-dimensional defect for surface science is, of course, the surface itself. Ideal crystals are infinite, and surfaces are a clear break in this rule. This break in symmetry - loss of neighbors on one side – leads to such exceptional properties of crystal surfaces. The increases in energy of the system associated with the lower coordination number may lead to reconstruction of the surface, i.e. the atoms on the top layer may move into other, more energetically beneficial positions than the ones that they would have if they followed the immediate symmetry of the bulk. Another process that follows is relaxation, or the changing of inter planar distances in the last two layers from the surface. If the surface is defined as just the exterior layer of the material, then it is appropriate to designate this as a two-dimensional defect. if the definition of the defect takes into account the subsequent relaxed layers, then such a surface would constitute a three-dimensional defect.

An important two-dimensional defect in the study of reduction is a shear plane, also named the Wadsley defect [76]. These types of defects form when there is a sufficiently high concentration of oxygen vacancies, which organize themselves along crystallographic directions, and are then annihilated by shearing. Other typically encountered two-dimensional defects are grain boundaries, shear planes and stacking faults.

1.4.4 3-dimensional

Three-dimensional defects one may include new phases in the bulk crystal matrix and voids. New phases in transition metal oxides are common, especially when the crystals are heavily reduced. A gradual, hierarchical transition from stoichiometric crystal to a heavily reduced phase occurs, with many less-reduced phases occurring in between. Voids, as the name implies, are spaces inside of the crystal, where there is no crystallographic ordering, but rather gas or vacuum. Such voids are formed during the growth of crystals using the Verneuil method, and can even be observed by optical inspection [80]. Smaller voids, ranging from micrometers to nanometers, can still be present in crystals, as has been demonstrated for $SrTiO_3$ [83].

1.5 Reduction of transition metal oxides

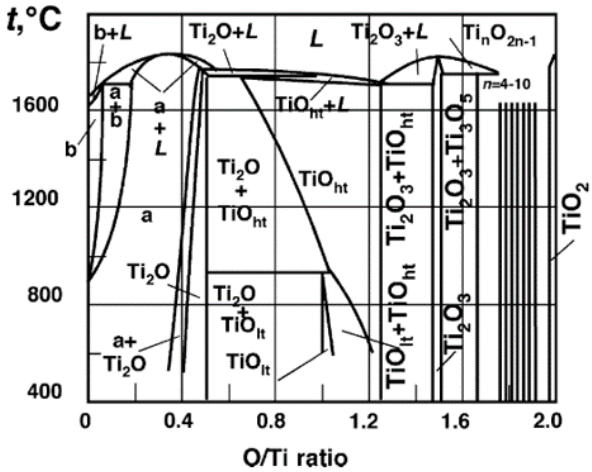

Figure 1.5: The phase diagram of a titanium-oxygen system, showing the multiple possible phases that can be produced and which remain thermodynamically stable [71].

Reduction is the loss of oxygen from a material and with this, one would think simple loss of a component, the transition metal oxide crystal changes dramatically. When an oxygen atom leaves the crystal lattice an oxygen vacancy is formed, and two electrons are left behind. These two electrons change the oxidation states of titanium ions in the crystal from the IV oxidation state to III or even II. Thus with the loss of a single oxygen atom, the crystal gains a positively charged oxygen vacancy, as well as two electrons near the conduction band gap. Using Kroeger-Vink notation, the change in the crystal lattice can be described as follows:

$$\mathrm{O_O} \longrightarrow \mathrm{V_O^{\bullet\bullet}} + 2\mathrm{e}' + \frac{1}{2}\mathrm{O_2}, \tag{1.1}$$

where V is a vacancy and e is an electron. In this notation, the charge relative to the lattice is written in superscript, and the position in the lattice is represented in subscript (if the atom is in the interstitial position, the letter i is used).

The oxygen vacancies formed during reduction exist independently and do not interact with one another in a small concentration window (for $TiO_{2\text{-x}}$ up to $x = 1 \times 10^{-4}$ [76] and for $SrTiO_{3\text{-x}}$ $x = 1 \times 10^{-3}$ [77]). If the reduction proceeds further, extended defects are formed. Initially oxygen vacancies organize each other into lines, or Magyari-Köpe defects [84]. At sufficiently high concentrations of oxygen vacancies, the vacancies organize along crystallographic directions, and are then annihilated by shearing, thus forming shearing planes (referred to as Wadsley defects) [76]. These shearing planes are at first distributed randomly in the crystal. However, with increasing reduction of the crystal, they group themselves into bands, creating structures of different crystallographic structure: at first, Magnéli phases [78], and subsequently other suboxides [80]. This evolution of defect chemistry has been described for TiO_2 [80], but the defects investigated, or their equivalents, also occur for other transition metal oxides, and parallels can be drawn for them. As demonstrated by the phase diagram of

titanium and oxygen (Fig. 1.5), such evolution can lead to the formation of a great range of different oxides, and controlling the thermodynamic parameters allows for an explorations of such phase diagrams and reaching the desired compound.

Crystals can be reduced using many means: by annealing in vacuum conditions [85], by sputtering [86], using direct current [23], electron irradiation [87] or chemical methods [88]. The investigation represented in this dissertation will employ reduction by thermal annealing, sputtering, and the combination of the two approaches.

1.5.1 Thermal reduction

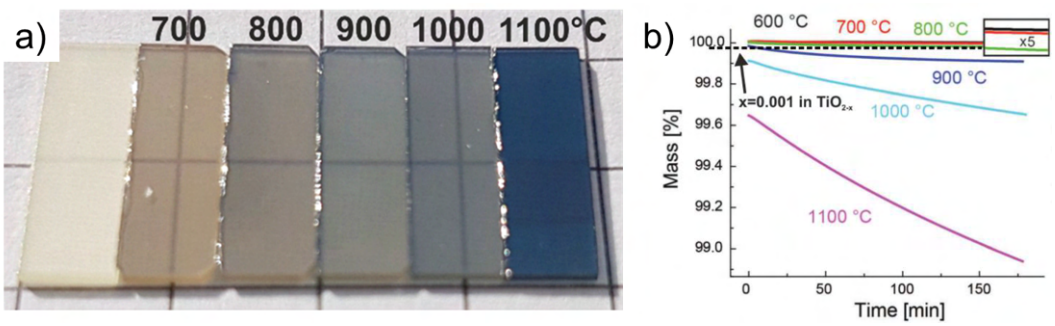

Figure 1.6: a) The colors of TiO_2 crystals annealed for an hour at different temperatures in UHV conditions; b) The mass change of TiO_2 crystals during such processes [89].

Thermal annealing in vacuum conditions is a time-tested method of reducing transition metal oxides. The increase in temperature, coupled with an oxygen-poor atmosphere, leads to oxygen loss in the crystal, which can be measured using simple mass spectrometer [89]. As temperature increases, more and more oxygen leaves the crystal, resulting in dramatic macroscopic changes as increasing number of transition metal ions change their oxidation states. In the case of TiO_2, coloring evolves from pure transparency, through shades of brown and blue to even black (see. Fig. 1.6a). This stoichiometry change is associated with an increase in conductivity of several orders of magnitude [90], [91] and even significant changes in the whole mass of the crystal [89], as depicted in Fig. 1.6b).

The following processes occur during thermal reduction: oxygen atoms leave the crystal, and the excess titanium atoms move into interstitial positions and diffuse into the bulk [91], which leads to the reduction of the crystal. The greatest reduction of the surface, however, occurs not at high temperatures during annealing, but during the cooling process [92]. This surprising process is caused by differences in the defect formation energy between the bulk at high temperatures and the bulk at low temperatures. At elevated temperatures, oxygen effuses from the crystal's surface, but oxygen also flows from the bulk to the surface, driven by the lower vacancy formation on the surface. But the energy of oxygen vacancy formation is a function of temperature [92], and during cooling, a diffusion of vacancies to the surface occurs, leading to changes from the ratio of vacancies on the surface to the ones in the bulk, equal to 1.2 at 1100 °C to 6.7 during cooling [92].

Even annealing at 800 °C can lead to significant changes in the crystal. This annealing

process in TiO_2 is associated with a mass loss of 0.05 % [89], which is in the regime of changes in stoichiometry which lead to the formation of Megnéli phases [74]. Furthermore, surface changes are also prevalent, with reduction leading to different reconstructions, with (1x3) attested in the research [93] (but not always easy to reproduce [94]), (1x2) and cross-linked (1x2) [91], [95]. Various temperatures associated with these reconstructions are fund in the literature, with temperatures of 827 °C [94], 878 °C [39], 927 °C [91], [96] for (1x2), and 1030 °C for (1x3) [94]. The cross-linked (1x2) reconstruction was observed at the same temperatures as (1x2), but with longer reduction times [91].

1.5.2 Extremely low oxygen partial pressure (ELOP)

The annealing of transition metal oxides in vacuum conditions leads to their reduction and to a decrease in the partial pressure of oxygen in the vicinity by means of getter material, such as silicon or titanium, accelerates such process. In case of ternary metal oxides, such as $SrTiO_3$, $BaTiO_3$, or $CaTiO_3$, other process occurs in addition to reduction. When the oxygen partial pressure reaches extremely low values, such crystals decompose by means of incongruent sublimation [97]. During incongruent sublimation, the components of the crystal sublime at significantly different rates, which leads to modifications of the crystal structure, with serious changes in stoichiometry and therefore formation of new phases.

In the case of strontium titanate this process has been observed and considered, but at extremely high temperatures, above 1300 °C [98]. However, if a substance which lowers the oxygen partial pressure is placed in the vicinity of the titanate, incongruent sublimation takes place even at the temperature of 1000 °C [97], [99]. The final effect is then a surface layer of reduced titanium suboxides on a bulk perovskite crystal, as the cation from the group 2 sublimates at a much higher rate than titanium. Depending on the conditions, such as temperature and the duration of annealing, the resulting surface may be porous and rough [97], or covered with highly crystalline nanostructures [99].

This effect can be used to obtain exotic, difficult-to-synthesize compounds in a crystalline form on a crystalline substrate in a bottom up process, as is the case for obtaining titanium monoxide nanowires on $SrTiO_3$ substrate [99]. Moreover, getter substances can be used to enhance reduction in binary compounds like TiO_2. In different experiments, the presence of a getter or the absence there of it may account for, for example, differences in temperatures for which the same reconstructions or values of electronic properties will be obtained in different publications. This is because, not only the temperature, but also the oxygen partial pressure affects the reduction of oxide crystals [100].

1.5.3 Sputtering

Sputtering of crystals using ion beams is a time-tested technique used in surface science laboratories in many different ways: as part of a cleaning procedure [101], as a means of creating nanostructures [102], or implanting dopants [103]. It is quite intrusive and changing, as it leads to scattering of components and roughening of the surface, and, in the case of oxides,

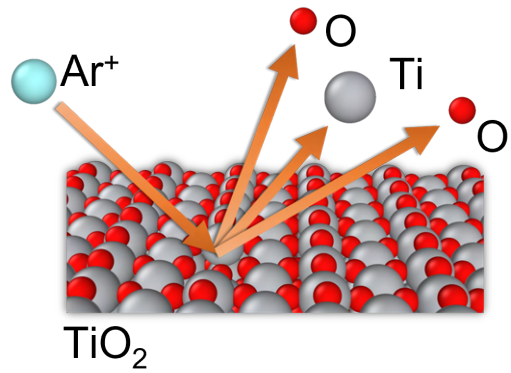

Figure 1.7: Schematic representation of preferential sputtering of oxygen on TiO_2.

it also reduces the crystals. In the case of TiO_2 it has been used to create a highly conductive sub-oxide layer on the surface of the crystal [104], or even to form a layer of TiO under its surface [105].

Irradiation with an energetic ion beam of a system composed of different elements may lead to changes in its composition due to preferential sputtering, i.e. one projectile from the ion beam has a higher probability of removing one of the components than the other. This ballistic process is observed experimentally in oxides [86] and in the case of TiO_2, the sputtering ratio is 1.3 [106], with more oxygen being sputtered per one ion than titanium atoms. This topic has been studied not only experimentally, but also using modeling, to find out the impact of parameters such as energy of the ions on the changes in the crystal [107]. Therefore, sputtering does not only change the morphology of the oxide sample, but it also reduces it, by introducing nonstoichiometry to the crystal's surface and subsurface.

1.5.4 Sputtering and annealing

Surface science requires a well-defined, clean surface as a good starting point for experiments. Experiments can only begin when such substrate is obtained. The method most commonly used for preparing such surfaces in the case of TiO_2 is repeated sputtering and annealing of crystals, or the so-called cleaning cycles. There are other methods which do not require sputtering, such as etching in HF acids and annealing in vacuum [108], however they are not as commonly used, as they require dangerous, corrosive chemicals and may introduce unwanted impurities to the crystal (such as fluorine). Cleaning cycles can be found in most experimental sections of publications concerning this area of research, but this does not mean that the procedure is the same in all laboratories. An analysis of related publications shows that the energies of ions differ (0.6 keV [91], 1 keV [109], [110], 2 keV [111], [112]), and that types of ions (Ar^+ [91], Ne^+ [113]) and the temperatures also vary (527 °C [114], [111], 727 °C [115], 1027 °C [91]). This method is so common place that some publications do not even specify the experimental details, such as the energy of ions [116], [117], [118]. The number of cycles used is not a typically specified parameter, as the procedure continues until a sharp LEED diffraction pattern is seen and/or no contaminations on the surface are found using X-ray photoelectron

spectroscopy (XPS) [119] or Auger spectroscopy (AES) [120].

Both of the components of the cleaning cycle, i.e. sputtering and annealing in UHV, are reducing in nature, as described in the sections above. The changes occurring during such preparation are not insignificant, as the whole crystal changes its color from transparency to a bluish hue [91]. Furthermore, the properties of the crystals change, e.g. the electrical conductivity is increased by orders of magnitude [90]. Even still, following multiple changes and cycles, the surface has the (1x1) reconstruction, and when investigated using XPS or AES, it is found to be stoichiometric. Throughout the preparation, oxygen is removed, and yet the resulting surface is essentially stoichiometric, while the crystal's properties and composition change. This discrepancy was the motivation for a series of experiments, whose results are described in Chapter 6.

1.6 Oxidation of transition metal oxides

Oxidation is the process of introducing oxygen back into the reduced crystal, and as such, it is the reverse process to reduction. The reversibility of the changes induced by reduction makes transition metal oxides even more tunable and attractive for applications. Oxidation is highly dependent on parameters such as the partial pressure of oxygen or, of course, temperature. The results of oxidation are as dramatic, as the crystal changes its color after high-temperature oxidation from black to white and e.g. its electrical conductivity decreases significantly [91].

Reduced crystals can be reoxidaized in UHV systems at elevated temperatures in the presence of gaseous oxygen. In such cases, the oxidation of the reduced TiO_2 occurs by the diffusion of Ti^{3+} from the bulk to the surface, where it reacts with atmospheric oxygen [91]. It has been proposed that the process of reoxidation likely begins at shear planes, which are the nucleation sites for oxidation [121]. The regrowth of the surface occurs with new layers of TiO_2 forming consecutively on the surface of the crystal, until stoichiometry is reached. This process is highly dependent on temperature, with significant rates of reoxidation observed experimentally at temperatures from 300 °C to 800 °C. Reoxidation also occurs at lower temperatures, but at much slower rates [91]. Annealing in oxygen rich conditions does oxidize the crystal further [122], but the process also brings changes in the surface [123], [124]. In such conditions, the reaction of interstitial titanium and gaseous oxygen leads to the formation of rosettes, strands and islands [123], [124]. These structures are respectively composed of incomplete TiO_2 layers, Ti_2O_3 and small (1x1) islands [124]. Furthermore, the process of oxidation at elevated temperatures is not limited to the surface as oxygen diffuses into the crystal's bulk in the form of oxygen interstitials at high temperatures and annihilates vacancies present below the surface [125].

Monocrystals can also be oxidized at much lower temperatures. In fact the healing of surface oxygen vacancies begins at the temperature of 120 K [126]. Oxidation is such conditions heals some surface oxygen vacancies, but even at room temperature, not all vacancies will be healed [92], [127]. Additionally, such oxidation does not affect the nonstoichiometry below the surface, as high temperatures are necessary for that to occur [125]. As a method of obtaining a TiO_2 surface which is close to stoichiometric plasma cleaning has been deemed the best

method [122], [128], as oxygen plasma is more oxidative than molecular oxygen. Moreover, this method does not require high temperatures, which prevents the segregation of impurities on the surface (as is e.g. the case with iron in anatase [129] or calcium in rutile [130]).

1.7 Application of TiO_2 in photocatalysis

Conversion of the freely available solar energy to energy that can be put into useful work is the aim of the study of photocatalysis. The seminal work by Fujishima and Honda [131] opened up the whole field to the area of transition metal oxides when it showed that rutile can be used in the production of hydrogen from water. From that point onward, multiple publications demonstrated that titanium dioxide is a promising photocatalytic material which can be not only be used to obtain hydrogen from water, but also to remove various pollutants from air [3], water [6] and soil [8]. It has even been used in artificial photosynthesis [132].

In order to obtain the best results for this compound, different phases [133], preparation methods [88], morphologies [134], compositions, doping [133] [135], have been investigated, spanning many years of research. Both of the most common phases of TiO_2, i.e. rutile and anatase, are used as photocatalysts, and each of them comes with its own set of advantages and disadvantages. As Ma et al. (2014) [134] wrote, rutile has better charge mobility, as it is more crystalline than anatase, however anatase has more active sites for photochemical reactions. Furthermore, anatase exhibits a higher surface area than rutile, and the charge separation is more efficient. On the other hand, rutile absorbs more light than anatase, due to its narrower bandgap. Due to these characteristics, both of the compounds are in common use, even concurrently, as it has been shown that using mixed-phase TiO_2 leads to the highest hydrogen production [136], [137]. The compounds can be further improved by various processes, such as narrowing the bandgap (e.g. in the famous black TiO_2 [138]) or introducing additional defects which improve photocatalytic efficiency [139], [140], [141]. Moreover, increasing the surface area to volume ratio, as is the case when using nanostructures, also boosts the efficiency of such crystals [142], [134].

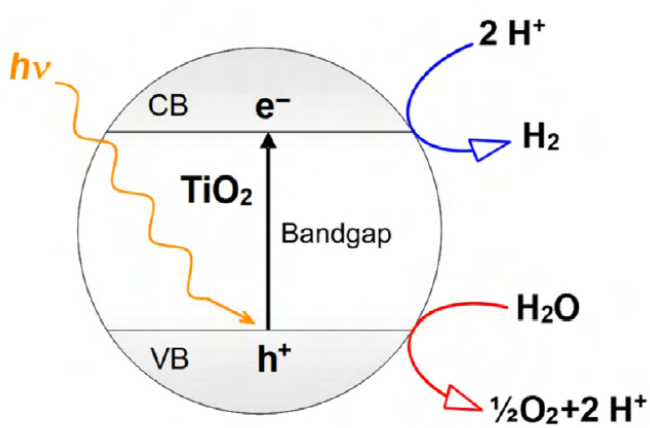

Figure 1.8: Schematic diagram showing photocatalytic water splitting in titanium dioxide [26].

Regardless of the type of preparation method or phase the basic mechanism responsible for photocatalysis in TiO_2 is the same and is schematically depicted in Fig. 1.8. Light of energy equal or higher than the band gap width is absorbed by the crystal which leads to the excitation of the electron into the conductive band and the formation of the hole in valence band:

$$\mathrm{TiO_2} + \mathrm{h}\nu \longrightarrow \mathrm{e}^-_{\mathrm{CB}} + \mathrm{h}^+_{\mathrm{VB}}. \tag{1.2}$$

These species may recombine or they may be used in chemical reactions such as the photocatalytic splitting of water. The following reactions take place on the surface of TiO_2, the formation of hydrogen ions from water:

$$\mathrm{H_2O} + 2\,\mathrm{h}^+_{\mathrm{VB}} \longrightarrow 0.5\,\mathrm{O_2} + 2\,\mathrm{H}^+, \tag{1.3}$$

and the synthesis of molecular hydrogen, which can be used as fuel:

$$2\,\mathrm{H}^+ + 2\,\mathrm{e}^-_{\mathrm{CB}} \longrightarrow \mathrm{H_2}. \tag{1.4}$$

Chapter 2

Analytical methods

The redox phenomena in transition metal oxides are complex processes which, as shown in Chapter 1, change the crystals drastically in their structure, as well as in their properties. A series of techniques was used in this dissertation in order to describe and understand the changes that occur during reduction and oxidation. Because the majority of the analytical methods implemented are well-known and commonly used, they will be overviewed briefly in this chapter.

2.1 Scanning probe microscopy (SPM)

Scanning probe microscopy is a versatile group of techniques which allow for measurements of surfaces in extremely high resolutions with often simultaneous measurements of their physical and chemical properties. Even though this group encompasses a multitude of specific modes and setups, the general principle behind all the techniques is the same, i.e. a sharp tip scans the surface at a very small distance, and the interactions between this probe and the sample are measured, to subsequently become and are the basis of the microscopy images. Thus all of such microscopes are composed of a sharp tip mounted on a scanner and an electronic system which controls the feedback loop and computer. Due to the high dependence of the signal on the tip-sample distance, as well as the fragility of the tips, such microscopes are placed in frequency-dampening systems.

All the SPM measurements presented in this dissertation were performed in UHV using the AFM/STM Omicron RT/UHV microscope. Chemically-etched tungsten tips were used for the STM measurements, while PPP-contPt cantilevers (Pt-Ir coated with eigenfrequency of 17 kHz) were used for LC-AFM and KPFM investigations. For KPFM measurements NC-AFM PT-Ir coated tips were also occasionally used.

2.1.1 Scanning tunneling microscope (STM)

The scanning tunneling microscope was the first SPM microscope, and its invention revolutionized surface science, as it was the first tool that allowed for relatively quick and easy investigations, both measurement and manipulation, at the atomic scale. The importance of this tool was recognized immediately, which is reflected in the fact that the inventors, Gerd Binnig and Heinrich Rohrer, received the Nobel Prize just four years after publishing their first STM images.

As the name implies, STM relies on the quantum tunneling effect in its operation [144], [145]. Quantum tunneling describes a classically impossible situation where an electron overcomes a potential barrier with energy lower than the barrier. This is due to the fact that electrons, just

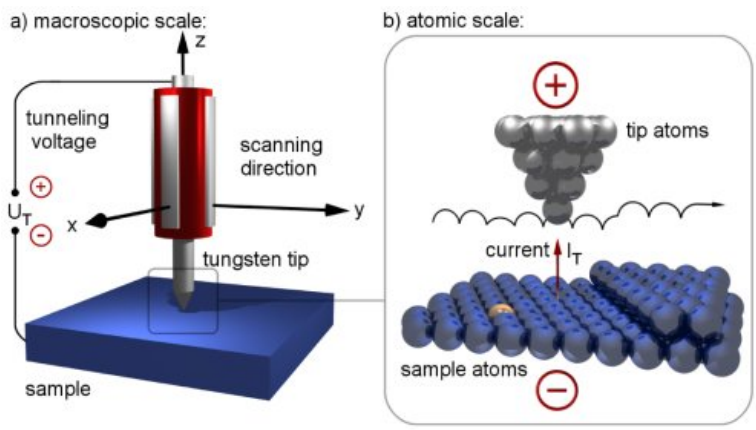

Figure 2.1: Schematic diagram of a STM, showing its working principle at both a) macro and b) atomic scales [143].

as all matter, can be described as both particles and waves, and therefore can display wave characteristics. The wave function, which describes the electron, decays exponentially when it encounters a potential barrier. However, at sufficiently low barrier widths and heights, it does not decay completely. Since the probability is proportional to the amplitude of the wave function squared, an electron might pass through such a barrier.

In the case of STM, electrons tunnel between, depending on the bias polarity, the metallic tip and the studied, conductive surface. In order to achieve this, the tip has to be brought close to the surface and voltage has to be applied to induce current flow (as depicted in Fig. 2.1a). As the tip is brought progressively closer to the surface, more and more tunneling current flows, which is depicted in the following equation:

$$I(d) = \frac{D(V)V}{d} \cdot \exp\left(-A\phi^{1/2}d\right), \tag{2.1}$$

where I is the tunneling current, d is the tip-surface distance, $D(V)$ is the density of the electron states, A is a constant, ϕ is the barrier height. As can be clearly seen, the current's dependence on distance is exponential, which allows for extremely high resolutions to be reached. The change in distance of 1 Å is followed by a change in the current by one order of magnitude, thus vertical resolutions of 0.1 Å can be obtained [146]. The high dependence on distance also means that most of the signal comes from the tunneling of the tip atom closest to the sample's surface. There is also some contribution to the total signal from the tunneling of tip atoms that are at a greater distance from the surface, which lowers the lateral resolution to values of approx. 1 Å.

Due to the fact that the tunneling current depends on both the distance and the density of electron states, the STM topography may be difficult to interpret. As depicted in Fig. 2.1b), the signal from a dopant atom might be reflected on the STM map as, for example, a vacancy, as its different density of states will lead to such change of current, which could have also indicated a sudden drop in height. Moreover, in oxide surfaces, such as TiO_2, distinguishing between which features are due to geometric and which due to electronic structures is especially difficult [147], which often means that a supporting technique has to be used to solve such

problems. Moreover, tip changes during scanning may also affect the image, and can even lead to the inversion of contrast [148], which further complicates the analysis.

The dependence of the current on the density of states can be used to the advantage of the researcher, as using STM one might perform a measurement of the local density of states as a function of energy. In order to perform this scanning tunneling spectroscopy, the tip must be set in place and the bias voltage has to be changed. The obtained $\mathrm{d}I/\mathrm{d}V$ vs V graphs must be compared with simulations to reach conclusions [149].

2.1.2 Atomic force microscopy (AFM)

Atomic force microscopy is a versatile SPM technique which, in contrast to STM, can be used on multiple types of samples and, depending on the mode used, it can measure various surface properties [150]. The differences between STM and AFM stem from the fact that AFM is based on forces which are universal and are always present when the tip approaches a sample. These forces cause the cantilever on which the tip is mounted to bend, and this deflection is measured using a laser beam and a photodiode detector, as it can be seen in Fig. 2.2a. Depending on the degree of tip-sample separation, two AFM modes, contact and non-contact, can be distinguished, and can be explained using the Lennard-Jones potential (Fig. 2.2b).

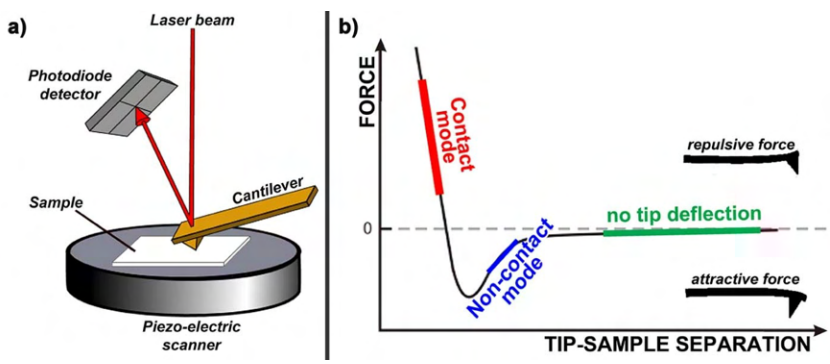

Figure 2.2: a) Schematic diagram showing the main components of a typical AFM microscope and b) the force-distance relationship based on the Lennard-Jones potential, with marked regions for the contact and non-contact modes [151].

In contact mode, the tip is close to the sample (on the order of a couple of angstroms) and forces arising from the Pauli and electrostatic repulsion act on it. The tips used in this mode have to be soft, in order to bend easily and avoid destroying or modifying the investigated surface. The contact mode might be executed in two regimes: the constant height or the constant force mode.

The non-contact mode is executed in the attractive region of the Lennard-Jones curve (Fig. 2.2). When the tip approaches the surface and reaches the distance of hundreds of angstroms, the Van der Waals force, which is attractive by nature, acts on the tip, bending it. In this mode of measurement, the forces are very small and they are detected by other means than by simple bending of the cantilever. The cantilever is induced to vibrate at its resonant frequency, while the forces arising from the tip-surface interactions shift this resonant frequency. Information

about the forces, and therefore the topography of the sample is hidden in the frequency shift signal.

One huge advantage of AFM is that changing the type of tip used or introducing a new element into the AFM system makes it possible to go beyond simple topography, and to measure surface properties at nano and even atomic scales. For example, magnetostatic interactions on the surface can be measured by changing the the default tip to a ferromagnetic probe [152]. Applying voltage to the piezoelectric sample and measuring the induced extension enables the investigation of the magnitude of the piezoelectric constant [153]. The two modes that are of special importance to this work are the ones which allow for the measurement of the contact potential difference and conductance, i.e. Kelvin probe force microscopy and local conductivity force microscopy, respectively.

Kelvin probe force microscopy (KPFM)

Kelvin probe force microscopy is a mode of non-contact AFM which allows for investigations into the work function at nano and atomic scales [154]. It is a technique introduced by Nonnenmacher, M, et al. (1991) [155] and it can be thought of as an extension of Lord Kelvin's seminal work on the contact potential difference of metals [156]. Lord Kelvin discovered that when plates of copper and zinc are in electrical contact, a potential is created between them. This potential of the capacitor depends on the materials that the conductors are made of. At its core, the potential due to the work function difference between them. In KPFM, instead of two metallic plates, a conductive AFM tip is used, while the sample functions as the equivalent of the other plate in Lord Kelvin's experiments. This allows for nanoscale measurements of the contact potential, and makes it possible to create maps of it [157]. The contact potential difference V_{CPD} in KPFM can be expressed as follows:

$$V_{CPD} = \frac{\phi_{sample}}{e} - \frac{\phi_{tip}}{e}, \tag{2.2}$$

where ϕ_{sample}, ϕ_{tip} are the work functions of the sample and the tip, while e is the elementary charge.

KPFM is an extension of the non-contact mode of the AFM microscope where AC voltage is applied during the measurement. The applied voltage V_{sample} has both AC and DC components, and it changes with time t at a frequency ω:

$$V_{sample} = V_{DC} + V_{AC} \sin(\omega t). \tag{2.3}$$

The electrostatic force F_{el} which acts between the tip and the sample can be expressed using the oscillating capacitor model:

$$F_{el} = \frac{1}{2}(V_{DC} + V_{AC} \sin(\omega t) - V_{CPD})^2 \frac{\partial C}{\partial z}, \tag{2.4}$$

where $\frac{\partial C}{\partial z}$ is the capacitance gradient. The electrostatic force can be separated into three components:

$$F_{DC} = -\frac{1}{2}\frac{\partial C}{\partial z}(V_{DC} - V_{CPD})^2, \tag{2.5}$$

$$F_\omega = -\frac{\partial C}{\partial z}(V_{DC} - V_{CPD})V_{AC}\sin(\omega t), \tag{2.6}$$

$$F_{2\omega} = \frac{1}{4}\frac{\partial C}{\partial z}V_{AC}^2(\cos(2\omega t) - 1). \tag{2.7}$$

The F_{DC} leads to a constant deflection of the tip, F_ω is used to determine the contact potential difference, the $F_{2\omega}$ can be used as the basis for capacitance microscopy [158], [159]. The measurement of CPD is done using a lock-in system, as the output of the lock-in amplifier is directly proportional to $V_{DC} - V_{CPD}$, as it can be seen in Equation 2.6. Thus, by sweeping the voltage in some range, the value of the V_{DC} for which the signal is zero, can be found, since it is equal to the CPD. A map of CPD can be obtained by performing this procedure at each point of the AFM map. If a surface with a well-known work function, such as a gold or HOPG surface, is measured by using the same tip, then the CPD maps can be calibrated to yield the work function values at each point.

An additional advantage of KPFM is that it can be used to measure the real height of structures on surfaces [160]. The forces acting on an AFM tip have three components: chemical, electrostatic and van der Waals. Chemical forces are only relevant below 5 Å [161], so they do not affect NC-AFM measurements. Van der Waals forces decay exponentially fast with distance, much faster than electrostatic forces. Thus, electrostatic forces affect the tip the most, and in the default NC-AFM mode, they are in no way compensated, so the measured force, which is the basis of the topographical maps, is skewed due to the work function differences between the tip and the surface. This affects the height and only when this electrostatic component is negated by the usage of KPFM can true topography be obtained [160].

Local-conductivity atomic force microscopy (LC-AFM)

Local conductivity AFM (also called conductive AFM) is a type of contact AFM that allows for the measurement of the local conductance of the surface. There are two differences between these types of measurements and the standard measurements, namely, the tip is conductive, and, during image acquisition, bias is applied and the galvanic current is measured. These simple modifications allow for remarkable results, at even atomic resolution conductance maps can obtained in this manner [162]. This is because, even though the tips have a radius of 20 nm, the contact area between the tip and the sample, which contributes to the measured current, is below 10 nm^2 [163]. Typically, the applied bias is close to 100 mV. However, I-V curve measurements can also be performed, where the tip stays in place, while the current response to voltage in some range is studied. Such investigations elucidate the characteristics of the surface, i.e. whether it behaves like a semiconductor or like a metal.

2.2 Scanning electron microscopy (SEM)

Scanning electron microscopy is a technique which can be used to image the surface of a material quickly and in high resolution. It is a versatile method that can provide information not only about the morphology of the sample, but also its composition. It can also be used in combination with other techniques, in order to provide data on the crystallographic ordering of

the surface at nanoscale and its composition. This makes it a powerful research tool in surface science and other areas of study [164], [165].

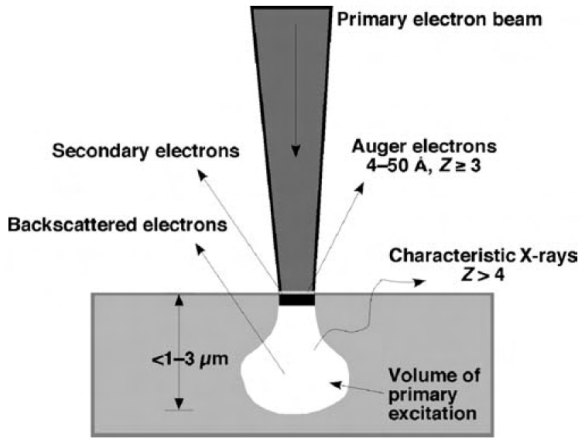

Figure 2.3: The schematic representation of the interaction of the electron beam with a sample, with the approximate volumes and depths from which different signals originate [166].

SEM microscopes are based on the interaction of a high-energy electron beam with the surface of a material. When such a beam impacts the sample, a series of processes may occur, each with its own characteristics, and each containing different information about the sample and originating from different depths of the sample, as can be seen in Fig. 2.3. In the setup used in this dissertation, the sample was imaged using the secondary electrons, backscattered electrons and X-ray fluorescence.

Secondary electrons (SE) are low-energy electrons (up to 50 eV) emitted from the depth of several nanometers [149]. The emission of SE is not strongly correlated with the atomic number of the element, but it displays high angular dependence, with more SE being emitted from edges than from flat areas. Thus, SE images show the topography of a sample at high resolution (of 5 nm to 20 nm [149]).

Backscattered electrons (BSE) are high-energy electrons from the source beam which are elastically scattered on the atoms of the sample. They are emitted from depths of 1 µm to 3 µm [166], and accordingly, generally, the BSE images have worse resolution than SE images. BSE carry additional information about the sample, which is absent from SE images, as BSE images display chemical contrast on the surface. This is due to the fact that the probability of backscattering is highly dependent on atomic number. BSE can be also used to determine the crystallographic composition of a surface and the structures that cover it, which is described in Section 2.2.2.

A SEM microscope is schematically shown in Fig. 2.4. The beam is formed in the main column of the SEM microscope using an electron source (in most cases, a field-emission gun). The emitted electrons are accelerated, and then the beam is formed using a series of lenses and apertures, eventually resulting in a beam cross-section of approximately 1 nm. The beam is then scanned over the surface of the sample and the desired signal is measured using one of the detectors. A Everhart-Thornley detector positioned at the side of the sample is used

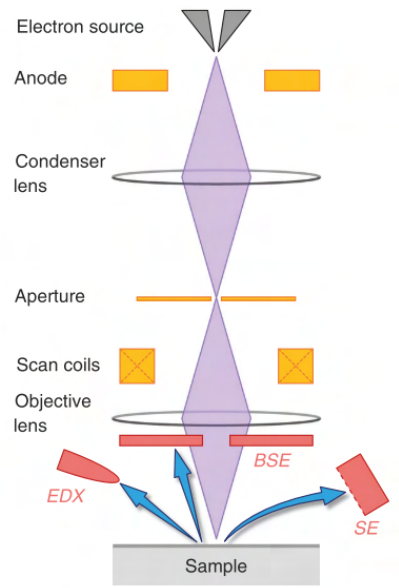

Figure 2.4: Components of the SEM microscope [167].

for secondary electrons. It is composed of a scintillator in a Faraday cage. A small positive voltage is applied and the SE are collected. In the case of BSE, the detector used is typically a semiconductor placed above the sample, around the final aperture of the beam column.

The Quanta 3D FEG microscope was used to perform the SEM measurements (SE/BSE images, EDX spectra, EBSD images) presented in this work.

2.2.1 Energy-dispersive X-ray spectroscopy (EDX)

In a SEM setup, the chemical elements in a sample can be identified using energy-dispersive X-ray spectroscopy (EDX). The interaction of the high-energy electron beam and the sample might lead to the excitation of atoms, and subsequent de-excitation in the form of X-ray fluorescence. The depth from which such X-rays are emitted is approximately 0.1 µm to 10 µm [149], which means that the information originates from a relatively great depth. The fact that the measurements are carried out using a scanning beam means that maps can be created. Their resolution will be lower than SE and even BSE images, due to the fact that the signal is collected from a greater depth.

EDX uses a silicon diode detector to measure the X-ray energy. The EDX chemical composition maps can be further analyzed using machine-learning algorithms, which allows for concealed patterns to emerge, as individual EDX spectra are assigned to structures present on the surface [168].

2.2.2 Electron backscattered diffraction (EBSD)

Electron backscattered diffraction is a technique which can be incorporated into a typical SEM setup in order to obtain information about the crystallographic composition of the subsurface, its domains and even nanostructures. It is a powerful technique that can be used to

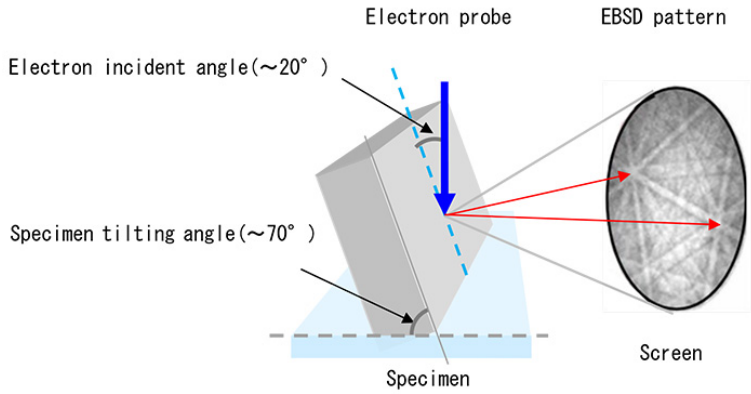

Figure 2.5: Schematic diagram showing the principle of operation of an EBSD apparatus [169].

study large areas, simultaneously showing orientation of many grains. Its resolution can reach even 10 nm [170], which makes it an indispensable method for characterization of nanostructures in an inexpensive and fast manner.

In order to perform EBSD measurement, a flat, crystalline sample must be rotated at an angle of 70° relative to the electron beam [171], as it is depicted in Fig. 2.5. Some of the electrons from the beam backscatter, as is the case in typical BSE measurements. These elastically scattered electrons interfere and, as it is described by Bragg's law, their interference pattern is determined by the crystal structure of the sample. In EBSD, the diffracting electrons form Kossel cones, which intersect with each other forming bright lines, i.e. Kikuchi lines, on the fluorescent screen. Each Kikuchi line corresponds to a specific plane in the crystal, and their analysis by fitting simulated patterns to the experimental pattern, allows for the determination of the phase of the sample.

2.3 Low-energy electron diffraction (LEED)

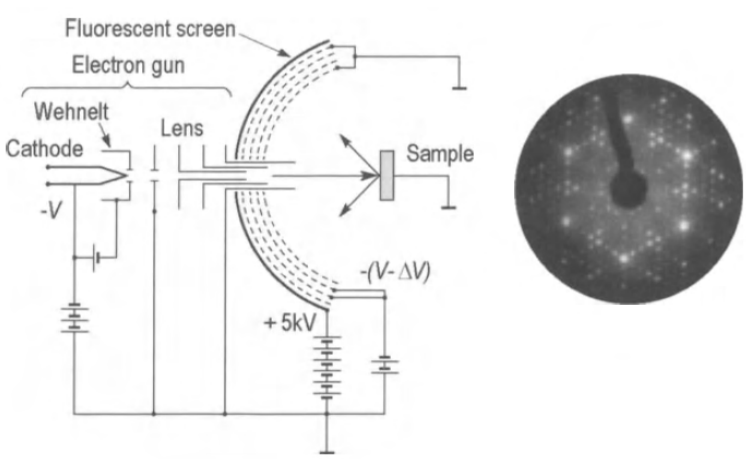

Figure 2.6: Schematic diagrams showing the LEED apparatus and the famous (7x7) reconstruction of the Si(111) surface [149].

Low-energy electron diffraction is a technique that can be used to study the arrangement of atoms on the surface of crystals. It is a diffraction-based method which relies on the fact that electrons, just like all matter, display wave like characteristics. Electrons used in this method are typically in the energy range from 30 eV to 200 eV, which corresponds to wavelengths of approximately 1 Å to 2 Å. Such waves are well suited to the study of crystallographic arrangement, as they are equivalent to distances between atoms, making diffraction effective. Furthermore, low-energy electrons have an extremely short mean free path of a few atomic layers [149], which means that the elastically scattered, diffracted electrons come from the surface only. The low mean free path is also the reason why LEED experiments must be performed in UHV conditions.

A typical LEED setup (Fig. 2.6) is composed of an electron gun, a series of grids and a fluorescent screen. Electrons are emitted from the electron gun by means of thermal emission and an electron beam is formed by a series of lenses. The set energy, and therefore the wavelength, is determined by the potential difference accelerating the electrons. The low-energy electrons interact with the grounded, conductive crystal. Some of them are scattered inelastically, some take part in the Auger process, and some are scattered elastically. The elastically scattered electrons interfere with each other and are the source of information about the crystal structure of the surface. They are separated from other electrons by the first set of grids to which opposing potential difference is applied, of a value slightly lower than the potential difference that accelerated electrons in the first place. The filtered electrons are then accelerated by the following grids and produce bright spots of the diffraction pattern on the fluorescent screen.

The observed diffraction image contains a lot of information. The type of information that is easiest to decipher and is typically used in investigations is to be found in the symmetry of the image and the distances between spots. The distances between spots are a function of interatomic distances on the surface, and the symmetry of the image reflects the way atoms are arranged on the surface in 2D cells. Furthermore, simply looking at the image provides qualitative information about the surface, as the brighter and more point-like the spots and the lower the background intensity the less defected the surface. Quantitative analysis of the image can also be performed, but with the rapid development of SPM techniques, it seems to have fallen out of favor. Just as in 3D crystallography, a model of the crystal can be proposed and fitted to the experimental data. In LEED, it is called I-V analysis, and the model data is fitted to the intensity vs primary electron energy curves measured for diffraction spots. Such analysis results in very accurate information about the distances between atoms. Another type of analysis is spot profile analysis (SPA), which yields information about the arrangement and the sizes of the terraces.

In this work a LEED/Auger instrument with a microchannel plate (OCI Vacuum Microengineering Inc.) was used.

2.4 Auger electron spectroscopy (AES)

The above-mentioned LEED experimental setup also allows the study of the chemical composition of the surface using Auger electron spectroscopy, which is a highly surface-sensitive analytical method.

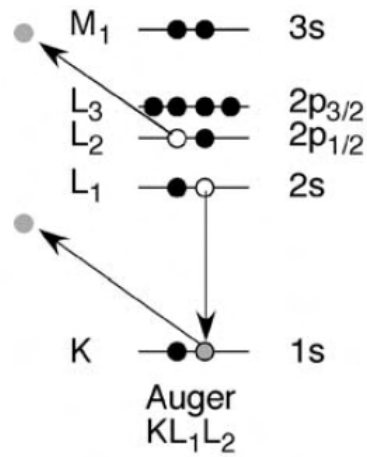

Figure 2.7: The Auger electron emission [166]. The energy of the Auger electron in this case is equal to: $E_{kin} = E_K - E_{L1} - E_{L2}$.

AES is based on the Auger effect which is schematically depicted in Fig. 2.7. When an inner shell electron is removed from the atom by interaction with a high energy electron or photon, an electron vacancy is formed and the atom is in an excited state. What follows is the transition of an electron from a higher energy state to the newly formed electron vacancy. The excess energy may be emitted by means of the ejection of the third electron, the Auger electron, which occupies an even higher energy state. Its kinetic energy E_{kin} is characteristic of the atom in which the transitions occur and can be described using the following equation:

$$E_{kin} = E_{core} - E_1 - E_2, \tag{2.8}$$

where E_{core}, E_1, E_2 are the energies of the states corresponding to, respectively, the core electron state, the first valence and the second valence shell. Since it is a three-electron process, the Auger effect cannot occur for hydrogen and helium. Furthermore, with increasing atomic numbers the probability of the Auger electron occurring decreases, while the probability of the competing relaxation process - characteristic X-ray emission, is increased. Accordingly, this analytical technique is not well-suited for heavy elements.

Experimentally, the same setup as described in the section above can be used to collect electron emission spectra. This is possible because when the LEED/AES setup is used, the the surface is also irradiated by low-energy electrons. Accordingly, Auger electrons are also emitted from the surface, and an electron emission spectrum can be acquired through the gradual shifting of voltage on the filtering grids.

2.5 X-ray photoelectron spectroscopy (XPS)

X-ray photoelectron spectroscopy (also known as ESCA, i.e. electron spectroscopy for chemical analysis) is a widely used analytical method which allows for both the qualitative and quantitative chemical composition determination of surfaces. Furthermore, its XPS spectra contain information not only about the elemental composition, but also about the chemical bonding, which makes it extremely useful for surface-science investigations.

XPS is based on the photoelectric effect, which describes what occurs when a high-energy photon interacts with a solid. If the photon's energy is higher than the binding energy of an electron in the atom it encounters, an emission of an electron from that atom may occur. The emitted atom has the kinetic energy $E_{kinetic}$, which is equal to the difference between the energy of the photon E_{photon}, the binding energy of the electron $E_{binding}$ and the work function of the surface ϕ (in XPS measurements, the work function is replaced by a constant experimental parameter of the system):

$$E_{kinetic} = E_{photon} - \phi - E_{binding}. \tag{2.9}$$

Rearranging the equation yields the formula for the binding energy of the electron in the atom:

$$E_{binding} = E_{photon} - (E_{kinetic} - \phi). \tag{2.10}$$

Since the energetic states of atoms have specific energies that depend on their atomic number, the obtained energies can be used to identify the components of the studied surface. Furthermore, the chemical surroundings affect the energies of the electron states, thus by measuring the shift in the energy (or the chemical shift) of the line as compared to a pure elemental sample, information about the chemical bonds can be obtained.

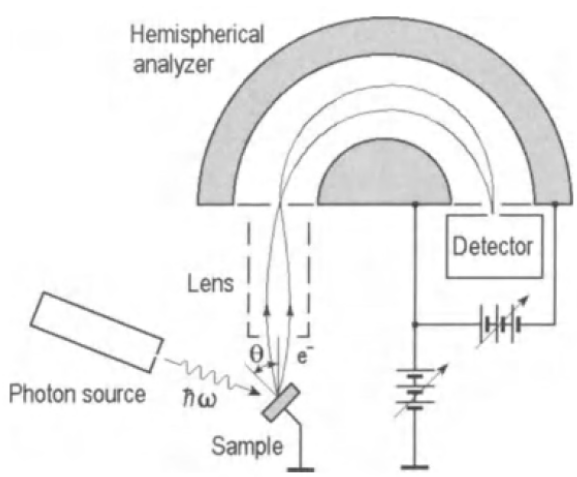

Figure 2.8: The schematics of a typical XPS system [149].

XPS systems are typically composed of a photon source, a hemispherical analyzer and a detector (see Fig. 2.8). Monochromatic light shines on the grounded sample, and photoelectrons

are emitted. The photoelectrons are focused in a beam which enters the hemispherical analyzer. Applying voltage to the hemispheres results in only electrons of a specific energy being able to pass through the analyzer and to reach the detector. Thus, by sweeping the voltage gradually, the whole range of energies of electrons can be measured. The electrons reach the detector, where their intensities are collected. In this way, XPS spectra can be acquired.

The XPS spectra presented in this thesis were collected using Phoibos 150 (SPECS) spectrometer with a 2D-CCD detector, equipped with the DAR 500 X-ray lamp with non-monochroamtic radiation (1253.64 eV Mg Kα).

2.6 Transmission electron microscope (TEM)

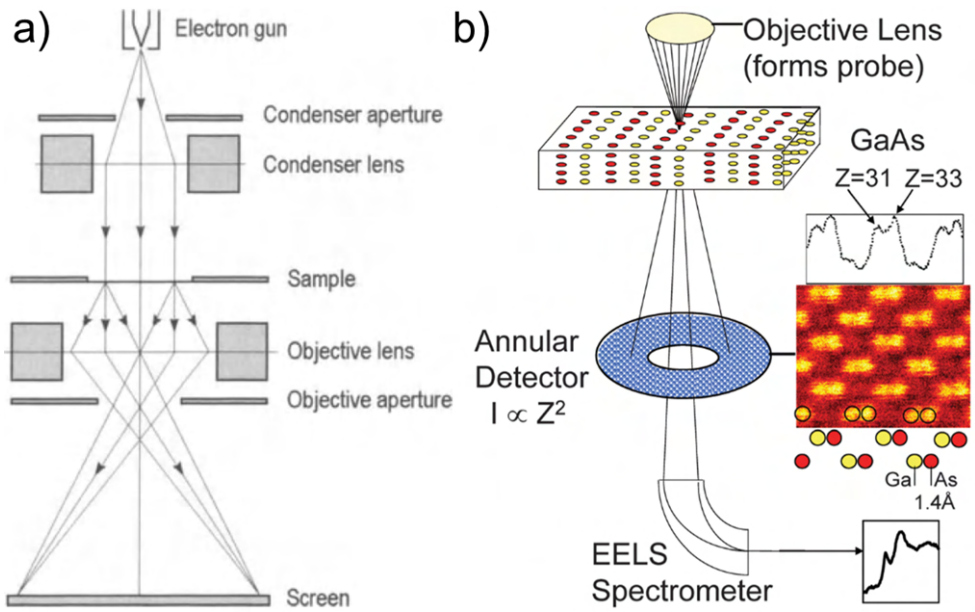

Figure 2.9: a) Schematic diagram showing the components of the TEM microscope (working in the bright field mode) [149] and b) a HAADF-STEM microscope with an EELS setup [172].

Traditional optical microscopes are limited due to the existence of the diffraction limit, which states that the resolution of a microscope is at most equal to approximately half of the wavelength of the wave used to image the sample due to diffraction. For visible light, this limit is in the hundreds of nanometers, and reducing the wavelength to X-rays brings its own set of challenges. There is a way to circumvent these problems, by using electrons instead of light. High-energy electrons have wavelengths of fractions of an angstrom, and their movement can be easily directed using electromagnetic fields. This was achieved in 1931 by Knoll and Ruska, with the TEM prototype in 1933 already providing better resolution than the traditional optical microscopes [173]. With time transmission electron microscopes developed in such a manner that nowadays they are routinely and widely used in many fields of science to study samples with atomic resolution.

The principle of operation of TEM microscopes (Fig. 2.9a) is analogous to the operation

of optical microscopes however light is replaced by electrons, and traditional optics give way to electromagnetic lenses. An electron beam of high energy is produced in the electron gun, is collimated using the condenser lens, and, finally, it reaches the sample. Samples used in TEM must be in the form of lamellae, i.e. thin slices whose thickness is in the range of 100 Å to 1000 Å [149] (depending on the composition and density of the crystal). This is because electrons interact heavily with matter, and, as the name suggests, TEM studies the transmitted electrons. Depending on the desired result, the remaining optical setup of the microscope differ. If real-space imaging is necessary (using the microscope's bright field mode), the aperture is placed in such a way as to let the direct beam pass (as shown in Fig. 2.9a). The resultant contrast on the detector derives from the change in beam intensity due to the scattering or absorption on atomic columns. Due to the high dependence of these phenomena on atomic numbers, bright-field images have a chemical contrast. If the aperture is placed off center, the diffracted electron beams are then the basis of image formation and the diffraction image due to Bragg scattering is observed.

In order to reach even better resolutions, another mode of TEM microscope may be used, i.e. high-angle annular dark field imaging scanning transmission electron microscopy (HAADF STEM), which reaches sub-angstrom resolutions [172]. This method differs from standard TEM in that the beam that interacts with the sample is focused and scanned over the sample, and the detection occurs on a circular detector placed beneath the sample (see. Fig 2.9b). HAADF-STEM images are easier to interpret, as the basis of contrast is almost solely the difference in atomic number [172]. The high-angle inelastic scattering, which is the basis of the observed images, can be modeled as simple Rutherford scattering, with the intensity of the signal proportional to the square of the atomic number. However, in reality, the coefficient is in the range of 1.6 to 1.7 [172]. A significant advantage of this type of TEM is that the beam is focused before the sample, so the signal comes from a small area. Other techniques, such as electron energy loss spectroscopy, can be used to study the sample locally instead of globally.

The TEM and EELS measurements were made on the FEI Titan3 G2 60-300 microscope.

2.7 Electron energy loss spectroscopy (EELS)

Electron energy loss spectroscopy (EELS) is a technique that allows for the identification of chemical components, their oxidation states, and processes that occur in them, such as plasmon excitations and interband transitions [174]. This is done by measuring the loss of energy of the electron beam after passing it through a thin sample. This technique can be coupled with HAADF-STEM (as depicted in Fig. 2.9b) to provide such data even at the atomic scale.

The operation of EELS is based on the fact that electrons encountering a material interact with it heavily, often inelastically. Such interactions heavily depend on the material at hand, with energy losses tied to the processes that occur in the material, which allows for its thorough analysis. This multitude of signals is both an advantage and a disadvantage of this method, as it provides an abundance of information about the sample, but it also makes the spectra difficult to interpret, and oftentimes requires simulations to be performed [174]. In order to

reduce the complexity of the spectra, the samples must be very thin, which ensures that there will no multiple interactions of one electron with the sample. Despite its complexity, this technique is extremely useful in the study of oxides, as it not only gives the information about the oxidation state of transition metal oxides, but, when used with HAADF STEM, also provides images with atomic resolution, making identification of oxide nanostructures possible [99].

2.8 Secondary ion mass spectrometry (SIMS)

The above mentioned analytical methods can be used to identify the composition of the surface of the crystal, but in some cases, the object of investigation is the distribution of atoms in the crystal, starting from the surface and ending in the bulk. Secondary ion mass spectrometry (SIMS) is the technique of choice in such applications.

A multitude of events takes place when a stream of high energy ions, in the range of tens of keV, impacts a surface. The energy and momentum carried by the ions are dissipated through collisions, emission of electrons or photons from the sample, vibration of the lattice, movement of the atoms in the sample or even their ejection. The process that is of interest for SIMS, as the name implies, is the emission of secondary ions. These are atoms of the sample which, due to the interaction with the impacting ions, become ionized and are ejected from the sample. Since these ejected atoms are the building blocks of the studied material, the analysis of the secondary ions allows for a thorough and extremely sensitive investigation into the composition of the material (for Time-of-Flight SIMS, the detection limits can reach $1 \times 10^{17}\,\mathrm{atoms\,cm^{-3}}$ [175]). This method uses ejected ions and not atoms, even though the probability of ion ejection is lower, because charged particles are much easier to work with. The fact that the studied object is charged also means that it will come from a smaller depth than if it were not [149].

SIMS can be used in two modes, static and dynamic. In static mode the ion beam scanned on the surface is of low fluence, so that each ion impacts a pristine part of the surface which has not interacted with any other ion. The fluence used in this mode depends on the sample measured, but typically $1 \times 10^{12}\,\mathrm{ions\,cm^{-2}}$ is used for organic, and $1 \times 10^{14}\,\mathrm{ions\,cm^{-2}}$ for inorganic surfaces [176]. In the dynamic mode the ion beam fluence is higher, therefore erosion of the material occurs during the measurement. This allows for the profiling of the composition of the studied sample. In both modes, if the ion beam is scanned on the surface, a 2D map of the composition can be created. Furthermore, in dynamic SIMS, such scanning allows for the acquisition of 3D maps representing the distribution of elements in the crystal.

SIMS is a great analytical method, but it comes with its own set of experimental and interpretational challenges. The first stages of SIMS measurements are difficult to interpret, because depending on the sample, it takes some time, for sputtering to reach equilibrium conditions [177], and since this stage of the measurement corresponds to the surface, this is quite a problem for surface science. Moreover, interaction with a high energy ion beam is by its nature a destructive process, and it causes the atoms in the sample to mix, which in turn leads to a decrease in resolution and the widening of sharp transitions [178] (cluster ions may be

used to significantly diminish this effect [179]). The existence of preferential ionization causes the ratios of ions to differ from the real ratio of elements in the sample [180]. Moreover, the probability of ionization also depends on the chemical surroundings of the atom [181], but this matrix effect can be lowered, e.g. by using cesium ions during sputtering [182]. SIMS experimental results are also affected by the surface morphology [176], as on a rough surface, such as one covered with nanostructures, secondary ions are emitted concurrently from the top of the structures and the crystal surface on which they were grown. Nonetheless, SIMS is a powerful analytical technique which yields information on the distribution of elements in the crystal, which, coupled with other complementary, more surface-sensitive techniques, provides the complete representation of a crystal's chemical composition.

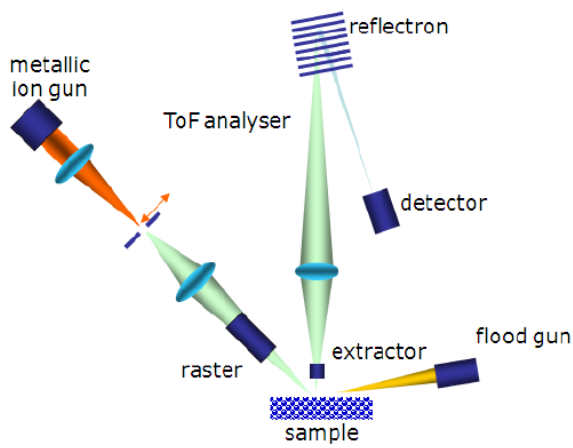

Figure 2.10: Schematic diagram showing the components of a ToF-SIMS apparatus [183].

The SIMS setup used in this work is a Time-of-Fight SIMS (ToF-SIMS), which is schematically depicted in Fig. 2.10. It is composed of an ion gun, an extractor, a time-of-flight analyzer and a detector. The ion gun produces impulses of ions of set energy which are then focused and scanned over the sample. The emitted secondary ions are then focused on the entrance of the analyzer using the extractor. Delayed extraction, i.e. applying a voltage to the sample just after the secondary ions are emitted, ensures that ions of the same mass but different initial kinetic energies reach the analyzer simultaneously. If the sample is nonconductive, an electron flood gun may be used to prevent charging. The time-of-flight measurement separates ions of different mass to the charge ratio m/q, by the simple principle that after the initial acceleration by the same voltage, ions of different masses will reach the detector at different time, which is expressed by the formula:

$$\frac{m}{q} = \frac{2t^2 E_k}{L^2}, \tag{2.11}$$

where t is the time of flight (or the time to reach the detector), E_k is the kinetic energy of the ions, and L is the distance traveled by the ions. In order to recalibrate the obtained SIMS spectra from relationship of signal to fluence, a profilometer may be used to measure the depth of the crater made during the measurement.

For the purposes of this work, SIMS profiling and imaging was performed using the TOF SIMS V (Munster, Germany) system.

Chapter 3

Experimental

This dissertation is concerned with the reduction and oxidation of transition metal oxide crystals. A wide array of preparation methods and experimental techniques was used to study these processes. Multiple annealing methods, varying in possible annealing temperatures and the quality and purity of vacuum or atmosphere, were used in order to prepare samples and then thoroughly characterize the changes occurring in them. This chapter contains a discussion of the different methods of annealing and the KPFM calibration.

3.1 Methods of annealing the samples in ultra high vacuum (UHV)

Thermal reduction of oxides in vacuum can be accomplished in many ways, each with its own advantages and disadvantages. Throughout this work, multiple methods were used to achieve different results.

3.1.1 Electrical current through a sample

The method that was used the most is annealing by electrical current flow through the sample. This is because this heating method can be used in the UHV system where the AFM/STM microscope is located, and therefore in situ measurements of morphology, crystallography and electronic properties can be made there. A typical holder is shown schematically in front and side view in Fig. 3.1a), c) respectively. As is the case in all materials that exhibit electrical resistance, the flow of current induces the dissipation of energy, and a subsequent increase in temperature. The temperature is monitored using a digital pyrometer. The value of emissivity used in the temperature measurements for TiO_2 was equal to 36 %, while for $SrTiO_3$, it was 70 %. Alternating current is used to ensure a more uniform temperature of the sample. Furthermore, heating using AC is also preferable because DC induces changes in chemical composition in transition metal oxides due to electroreduction (also known as electrodegradation) [185], [23]. Electroreduction is a process that occurs in oxides when, due to the electrical field, the ions of the crystal lattice migrate. Oxygen vacancies accumulate on one end of the crystal, which in effect leads to a gradient of reduction in the crystal.

The annealing by current flow through the sample is a great method for surface science experiments meant to be performed in situ, as this heating method incorporates a holder designed for use with the Omicron UHV microscope. Furthermore, the uniformity of the temperature when preparing samples is of high quality when the temperatures are below 1050 °C, as the temperature gradients on the exposed monocrystal surface are on the order of

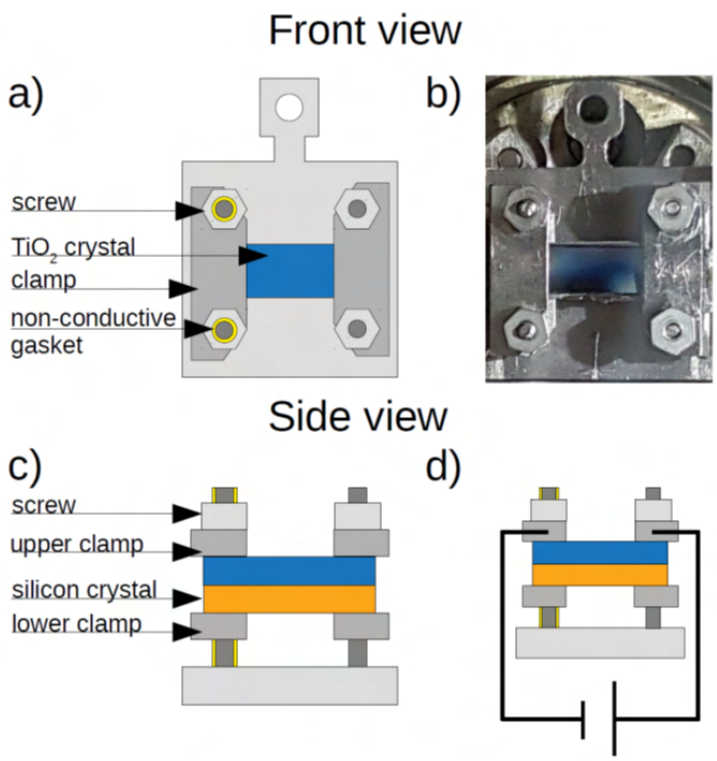

Figure 3.1: Front view of the current through a sample holder presented in a a) schematic form and b) in reality; c), d) side view schematic view of the holder [184].

approximately 30 °C. For higher temperatures, however, the gradients tend to be higher, and cracking of the crystals is common, as the tension due to the non uniformity of the holder's elements acts upon the crystal. An additional challenge in annealing at high temperatures originates from the fact that the crystals used as an aid in heating (the studied crystal is placed on top of silicon crystal) tend to have a higher temperature and may melt at random locations, leading to cracking or a pronounced non uniformity of temperature, which interferes with the planned experiments. The temperature of the supporting silicon crystal is unknown, which makes this annealing method not well-suited for the systematic investigation of the effect of getter temperature on the crystal properties.

Several methods of reducing temperature induced stresses in these types of holders were tried: clamps made from various materials (molybdenum, tantalum, titanium) and of different thicknesses, using different thicknesses of silicon crystals, placing a sapphire crystal between the silicon and the studied crystal and placing silicon monocrystal pieces between clamps and studied crystal. However, none of these methods showed any promise of mitigating the crystals' cracking at high temperatures.

3.1.2 Electron beam holder

Some crystals were annealed using electron beam holders, which is a method that allows for easy sample preparation for ex situ studies. When used with the electron beam holder, crystals are simply placed on the tantalum plate, with no additional clamps that might have

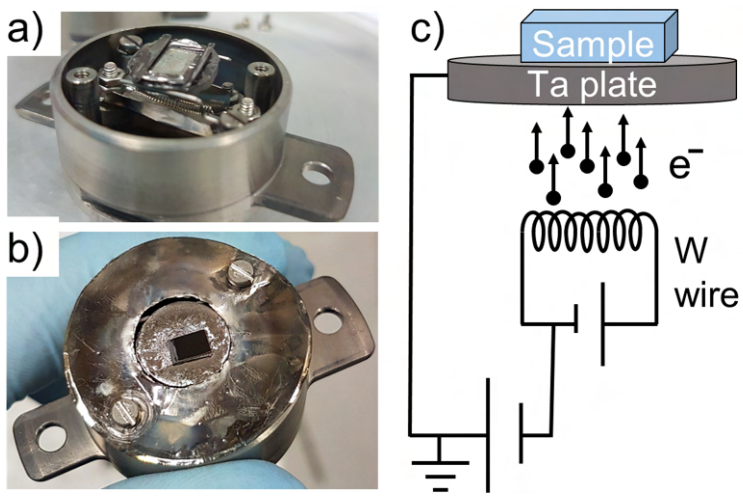

Figure 3.2: Electron beam holder as viewed a) without and b) with protective foil. In a) tungsten wire, which acts as a cathode is visible, while in b) a sample can be seen in the middle of the tantalum plate. c) Schematic diagram of the electron beam holder.

served as a source of both tension and thermal gradients (as when using clamps, the thermal contact in the vicinity of the clamps is much better than in other parts). The electron beam holder is depicted in Fig. 3.2a, b). As the schematic diagram in Fig. 3.2c) shows, the holder is composed of three parts: a tantalum plate on which the sample is placed, a tungsten cathode, and an electron accelerating circuit. When the device is in operation, electrons are emitted from the tungsten wire due to thermal emission, to then be accelerated by the applied voltage. The accelerated electrons hit the back of the tantalum plate, which increases its temperature, and therefore heats the crystal on top of the plate. The protective foil seen in Fig. 3.2b) is positioned there to prevent electrons from directly bombarding the crystal surface.

Annealing using electron beam holders is a great method for preparing monocrystals for ex situ experiments, as the crystals tend to crack less than when using direct current flow. This is due to the fact that the heating is based on the increase of temperature of the whole volume of the tantalum pallet, which offers a uniform heating platform, but the direct current flow method relies on the increase of the temperature of the silicon crystal, which tends to partially melt at high temperatures. Furthermore, this method provides information on the temperature of the getter material, as its surface is exposed and can be measured using a pyrometer. The possibility of using titanium foil as a getter in this method also makes it possible to investigate different getter materials and even different getter amounts. The obvious disadvantage is the fact that in the setup described, in situ studies of the electronic properties are not possible.

3.1.3 Quartz tube and Knudsen cell

The final methods of annealing used in this dissertation were annealing in a quartz tube (Fig. 3.3a) and a Knudsen cell (Fig. 3.3b). Both of these methods allow for great reproducibility, as they provide a uniform temperature to the whole volume. The quartz tube has been used in the investigation of the annealing of wire-covered $SrTiO_3$ in oxygen. Moreover, these annealing methods were tested and deemed unsuitable for the study of the effect of the oxygen getter

temperature on the growth of nanostructures on strontium titanate, as it was discovered that the getter must have much higher temperature than the investigated crystal, which cannot be achieved here.

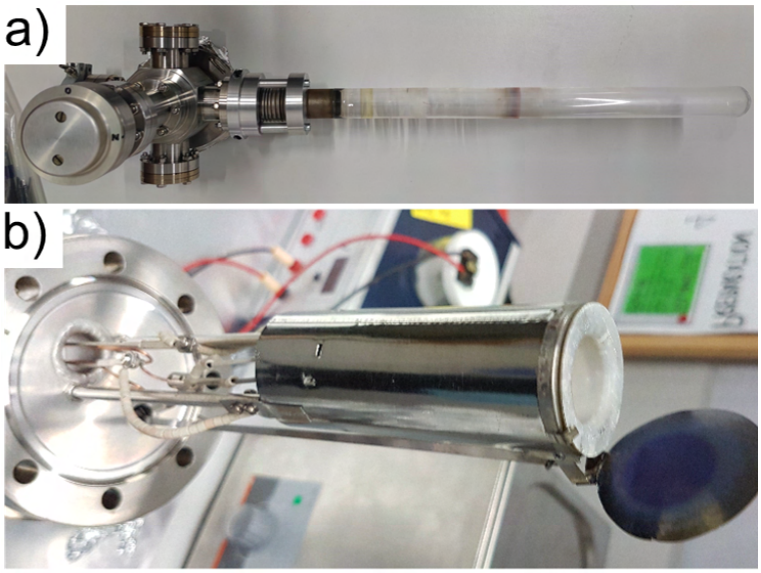

Figure 3.3: a) The quartz tube and b) the Knudsen cell used during annealing,

In quartz tube annealing, a sample is placed in the quartz tube, air is pumped out, and an oven is placed around the tube. In the oxidation experiments, before the annealing started, oxygen pressure was stabilized at the desired value.

When using the quartz tube, crystals were placed in an aluminium oxide Al_2O_3 crucible with a lid with a hole. The crucible was then placed in a small quartz tube, which was then deposited in the main quartz tube. This procedure was followed in order to ensure the maximal possible pureness of the experiments, as both the crucible and the small quartz tube were easy to clean using chemical methods or annealing. The quartz tube was heated by an oven, which was preheated to the set temperature and then placed on the tube.

The experiments in the Knudsen cell also used a crucible with a hole. The advantage of this setup is the possibility of increasing the temperature more than for the quartz tube (as silicon sublimation was observed for temperatures above 1000 °C). Furthermore, the higher mechanical stability allowed for experiments of higher complexity, such as annealing of monocrystals partially submerged in getter powder. The disadvantage of this method is a more limited temperature uniformity, as the heating element is only a thin wire, while a bulk oven is used for the quartz tube.

3.2 Methods of sample oxidation

For the purpose of this dissertation, the crystals were not only reduced, but also oxidized using several techniques: by exposing annealed crystals at room temperature to oxygen in UHV conditions, by annealing them in oxygen in UHV, or by exposing them to air at normal pressure.

3.2.1 Oxidizing in UHV conditions

The simplest and most often used method of oxidation was the exposure of reduced samples to oxygen in the UHV system. The chosen oxygen pressure for these experiments was 5×10^{-8} mbar, selected because it is relatively small pressure, which allowed for study of the kinetics of oxidation.

During such experiments the ion pumps and one of the hot-filament gauges were turned off, to slow down the adsorption of hydrocarbons on the investigated surface (one had to be left operating to monitor the oxygen pressure). After such experiments, the crystals were annealed in isotopic oxygen, at the same pressures, for one hour at 800 °C. The oxygen was introduced to the system in both cases using a precision gas valve.

To provide harsher oxidizing conditions, some of the samples were annealed in oxygen. The oxygen pressure was set at either 5×10^{-8} mbar or 2×10^{-2} mbar, depending on the desired level of oxidation. Isotopic oxygen ^{18}O was used to check the depth of changes introduced by repeated sputtering and annealing (see Chapter 6). The annealing time in all cases was one hour, and the temperature was 800 °C.

3.2.2 Oxidizing by exposure to air

To test how air affects the electronic properties, some of the crystals were exposed to atmospheric air, and the results of oxidation using just oxygen. The samples were reduced in UHV, studied, and then introduced to the load-lock chamber of the UHV system, where they were exposed to air. Subsequently, their properties were measured again. In order to determine the impact of easily desorbing adsorbates, such as nitrogen molecules and water, the following step was annealing at 230 °C for one hour and subsequent measurement.

3.2.3 Summary of the annealing methods

The main characteristics of the annealing methods tested during the investigation of redox processes are summarized in Table 3.1. Each of the annealing methods has its merits, not only from the experimental point of view (control of parameters, cleanliness, etc.), but also from a practical point of view, i.e. ease of sample preparation and reliability of annealing. All in all, there is no perfect method of thermal reduction, and a suitable method must be selected during the planning phase.

The high temperatures of annealing studied in this dissertation proved to have its own challenges. At extremely high temperatures, even clean materials can be a source of contamination. For example, a tungsten wire can cause heavy metal deposition on samples. Furthermore, contaminations present in as-received crystals segregate due to the increased temperature. Even such basic physical processes such as heat transfer can become a source of problems in UHV at high temperatures, as conventional heat conduction becomes less effective than radiation, and samples become significantly nonuniform in temperature.

Table 3.1: Summary of the used annealing methods describing their characteristics in the context of oxide reduction experiments.

Annealing method	Sample	Max temp. of sample	Temp. uniformity	Temp. of getter	Cleanliness	ELOP usefulness
Current through sample	Monocrystal	Depending on type of crystals and luck, for TiO_2 on Si >1350 °C, for $SrTiO_3$ on Si 1250 °C was achieved	Relatively uniform below 1050 °C (approx. 30 °C)	Unknown, but higher than the studied sample's*	Clean	Useful
Electron beam holder	Monocrystal	Temp. of sample above >1350 °C, temperatures of 1668 °C reached (melting temp of Ti), high temp can be reached without difficulty	Relatively uniform below 1050 °C (approx. 30 °C)	Known, in case of silicon. The same as sample, in case of Ti much higher	Clean	Very useful
Quartz tube	Monocrystal or powder	1150 °C can be reached, but above 1000 °C Si contamination	Uniform	Known, the same as sample	>1000 °C signs of Si	Limited usefulness**
Crucible	Monocrystal or powder	1450 °C was reached	Uniform	Known, the same as sample	Clean at least till 1450 °C***	Limited usefulness**

*The temperature measurement is performed using a pyrometer and the getter crystal is placed under the studied crystal, so its temperature cannot be measured. The getter's temperature is higher than the sample's temperature, as indicated by the color of glowing and the fact that it partially melts even when the temperature of the sample is lower than the getter's melting temperature.

**The experiments have shown that the getter should have much higher temperature than the perovskite crystal in the study of the growth of nanostructures. When the getter temperature is raised enough for the getter to be active, the temperature of the crystal is so high that the structures are badly defined and contaminated.

***The annealing in this method is due to radiation from tungsten wires. It must be noted that at high temperatures, tungsten wires begin to sublimate. Contamination with heavy metals was observed on the surface of monocrystals at high currents passing through wires in another heating system based on the same principle.

3.3 Monocrystal preparation

In order to remove all contaminations from the as-received crystal's surfaces and to ensure high quality of the vacuum, all monocrystals were first cleaned using the following procedure. First, the as-received crystals were cleaned using acetone, in order to remove all traces of glues or other organic substances, and then they were placed in isopropanol and rinsed for approximately 15 min in an ultrasound bath, to remove any foreign objects which could be present on the surface. Such pristine crystals were mounted on appropriate holders and placed in UHV systems. Then the crystals were degassed at temperatures of approximately 400 °C, which are below the temperatures associated with reduction, but are high enough remove inorganic adsorbates, such as water. Experiments were conducted once this procedure had been completed.

3.4 KPFM calibration procedure

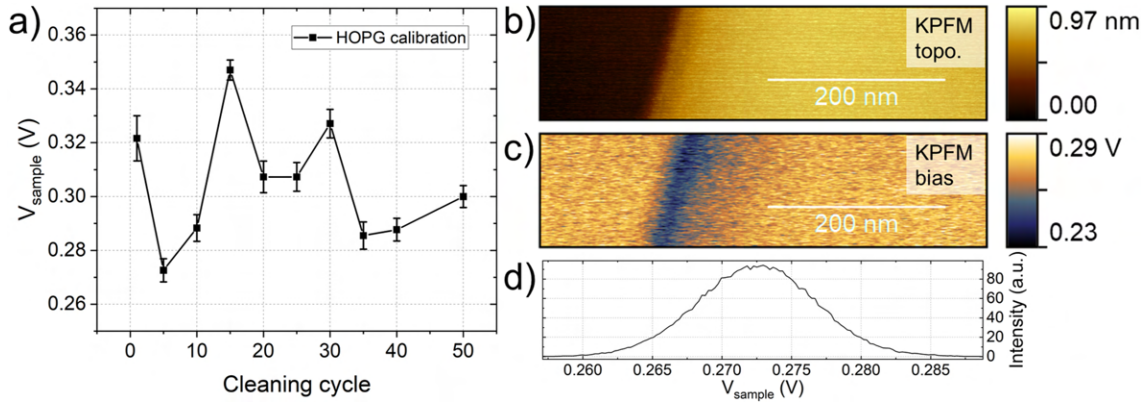

Figure 3.4: a) The sample bias measured on HOPG using the same tip which was used for calibration in the multiple-cycle experiments (Section 6.3), a fragment of a typical HOPG image showing b) the topography and c) the bias map with d) the histogram of the bias (the edge region was masked).

KPFM measurements providing the contact potential maps were performed simultaneously during the standard topography measurements, which was possible by using the additional third loop for bias compensation [186]. The contact PPP-contPt tips were used in most of the experiments, even though KPFM is a non-contact mode, because the tip was excited to higher harmonics (approximately 90 kHz). The amplitude of oscillation was approximately 10 nm. The bias loop operated with the modulation sample bias frequency of 100 Hz to 200 Hz and the amplitude was 500 mV.

In order to obtain absolute work function values, the tips were calibrated before and after measurements against the highly oriented pyrolytic graphite (HOPG) surface, which has a well-known work function of 4.5 eV [187] [188]. A fragment of a typical image of HOPG surface (showing a step-edge) can be seen in Fig. 3.4, with both topography and bias maps. The sample bias values measured on HOPG using the same tip throughout the series of experiments

typically did not change significantly, as can be seen on Fig. 3.4a), where, even after multiple measurements spanning months, the values differed only by 0.03 V.

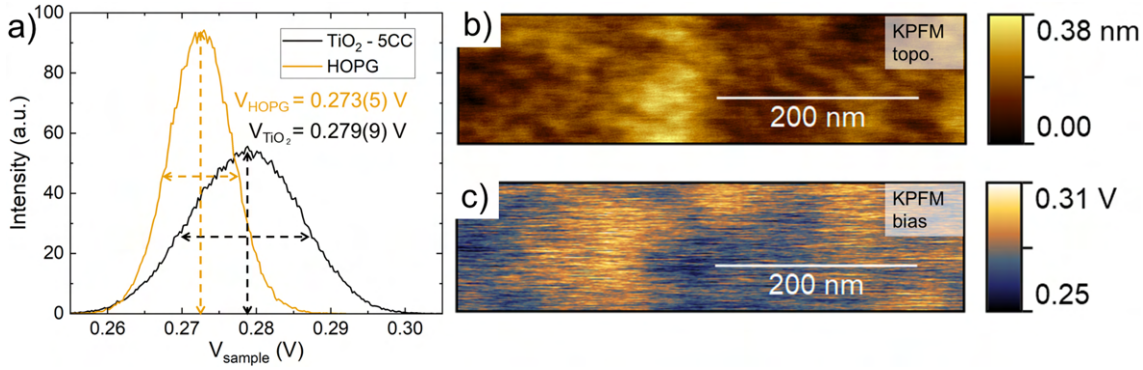

Figure 3.5: a) Sample bias histograms of a measurement performed on a TiO_2 surface and a following calibration measurement on HOPG. Fragments of raw data maps for TiO_2 of b) topography and c) bias are presented, while the maps for HOPG can be seen in Fig 3.4.

Chapter 4

Goals of the thesis

The goal of this dissertation is to investigate the effect of reduction and oxidation on the electronic properties, chemical composition and morphology of transition metal oxides, exemplified by model binary and ternary oxides, i.e. titanium dioxide TiO_2 and strontium titanate $SrTiO_3$. A broad range of methods of reduction and oxidation methods were studied. In case of reduction, these were annealing in UHV, ion sputtering, repeated ion sputtering and annealing, and in case of oxidation, the methods employer were exposure to oxygen at room temperature, exposure to air at atmospheric pressure and annealing in oxygen. These processes and their effects were studied using a multitude of techniques that provide insights into the morphology, chemical composition, crystallography and electronic properties of the crystals at hand, in order to provide the most thorough description of the observed changes.

The main research questions are:

1. To what extent can work function and conductance of TiO_2 and $SrTiO_3$ can be modified using reduction and oxidation? What are the changes in the chemical composition and morphology due to these processes?

2. Does the time-tested method of preparing the stoichiometric TiO_2 surface using repeated sputtering and annealing affect its electronic properties?

3. Does the presence of oxygen getter material during annealing affect the electronic properties and morphology of $SrTiO_3$?

4. How does the annealing in oxygen affect the morphology and electronic properties of the nanowire-covered $SrTiO_3$?

Chapter 5

The effect of annealing on the electronic properties of TiO_2

Oxide crystals can be studied in the context of redox processes using many methods, but one of the simplest approaches is annealing such crystals in oxygen-poor conditions or simply exposing a reduced crystal to oxygen. In this chapter, these methods are investigated using TiO_2 monocrystals. The discussion in this chapter reveals that even though annealing a crystal is a simple procedure, the changes which occur in annealed crystals are far from straightforward. The interplay between reduction and oxidation, as well as the movement of impurities in the titanium dioxide monocrystals and its effect on the chemical composition, morphology and electronic properties will be described below.

5.1 Changes induced by annealing in UHV

In the first stage of the investigation, the TiO_2 monocrystals were reduced in one of the simplest ways possible, i.e. by annealing them at low oxygen partial pressures, i.e. in UHV.

5.1.1 Experimental

In order to systematically study the changes induced by annealing, a set of experiments was performed following the same procedure. The samples were degassed at 600 °C, in order to remove adsorbates, and then they were annealed at the selected temperature for one hour. Annealing was performed at the following temperatures: 700 °C, 800 °C, 900 °C, 1000 °C, 1100 °C, 1220 °C, 1300 °C and 1350 °C. A new crystal was used at each temperature setting.

5.1.2 Changes in morphology and crystallography

The morphology of the TiO_2 surface changes with the increasing temperature of annealing, as can be seen in Fig. 5.1. With increasing annealing temperatures, the size of terraces increases, and their borders become more compact. The STM morphology shows a grainy structure on terraces (see Fig. 5.1a, b). These grains are most likely due to adatoms present on the terraces. The broadening and the differing size of grains is indicative of the size of the STM tip. Below 1100 °C, the surfaces are composed only of terraces, but at 1100 °C, some of the samples start to develop other characteristics. As shown in region A in Fig. 5.1 c), on borders of some terraces of the surface annealed at 1100 °C, domains of other reconstructions start to form. Moreover, at the same temperature, low structures (height approximately 1.8 Å) can be observed (region B in Fig. 5.1d), which can even span a couple of terraces, as depicted in

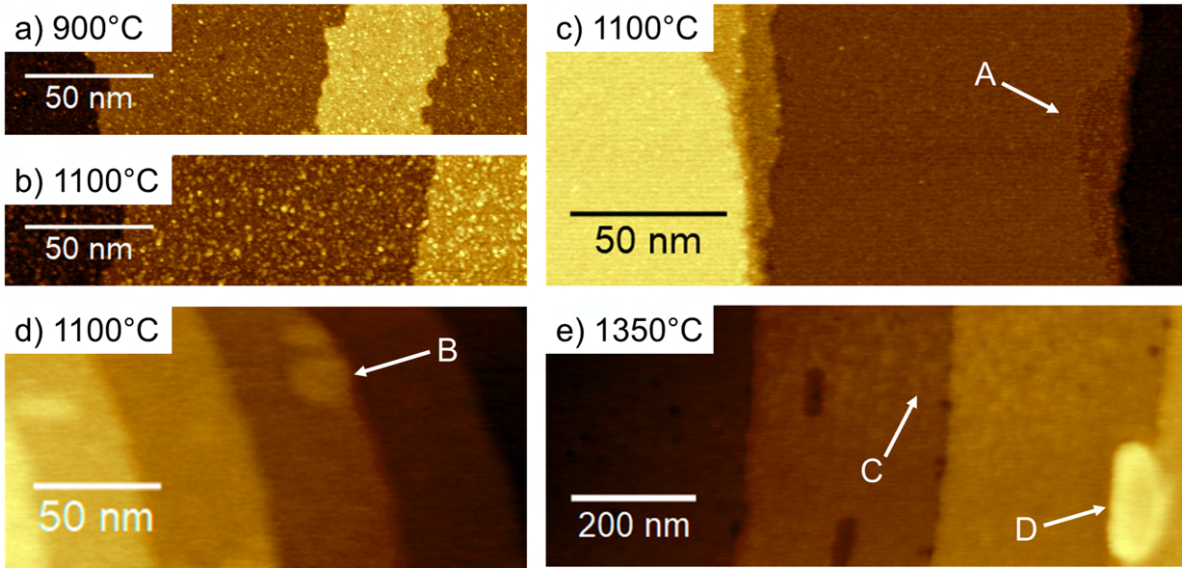

Figure 5.1: Morphology of the surfaces annealed at a) 900 °C, and b), c), d) 1100 °C, and e) 1350 °C. a), b) and c) show STM images obtained with the sample bias of 1.6 V and the set current of 16 pA, while the morphologies in d) and e) are derived from LC-AFM and KPFM images, respectively. The labeled structures refer to: A - region of different reconstruction, B - low island, C - region of high roughness, D - high island.

Fig. 5.7c). At the temperatures of 1220 °C, 1300 °C and 1350 °C, holes in terraces, such as the one in Fig. 5.1e), started to appear. Moreover, the small islands seen at 1100 °C were replaced with higher structures (height approximately 0.6 nm), such as the structure labelled D in Fig. 5.1e). The images for the temperature of 1350 °C also display another feature, i.e. regions of higher roughness on areas measuring hundreds of nanometers in length and width (labelled C in Fig. 5.1e).

Long-range ordering was investigated using LEED, which reveals that at any of the annealing temperatures used, the surfaces are crystalline, as they display diffraction spots (Fit. 5.2). The ordering of the surface changes with temperature, beginning with a (1x1) pattern at 700 °C. Subsequently, it goes through a c(2x2) reconstruction for temperatures in the range 800 °C to 1100 °C and then changes into c(6x2) for even higher temperatures. It should be noted that the c(6x2) reconstruction was also seen on a part of another crystal which was annealed at 1100 °C, which suggests that the transition temperature is in the vicinity of that temperature.

The nearness of the transition between the two reconstructions can be seen in the STM images for 1100 °C, e.g. Fig. 5.1c), where two domains can be seen coexisting on one terrace. The main domain was imaged at atomic resolution (Fig. 5.3a), and the fast Fourier transform (FFT) was performed. Comparing the FFT with the diffraction pattern (Fig. 5.3b) reveals that they are equivalent. The other domain present at this temperature is most likely c(2x2), since it can be seen in some LEED patterns for crystals prepared this way.

The cause of the changes described above can be part of one of the processes, either the reduction of the crystal or the segregation of impurities on its surface. Typically, TiO_2 crystals

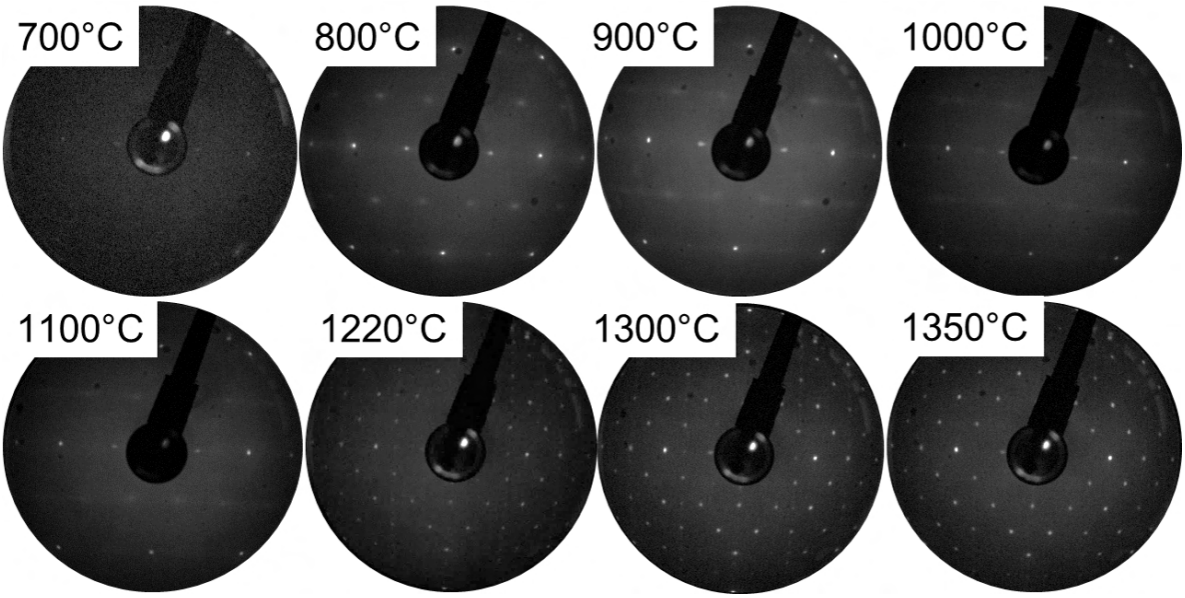

Figure 5.2: The diffraction patterns collected for surfaces annealed at different temperatures. The surface annealed at 700 °C has the reconstruction (1x1), which for temperatures in the ranges of 800 °C to 1100 °C changes into c(2x2), and above that temperature into c(6x2). The electron energy is 106 eV.

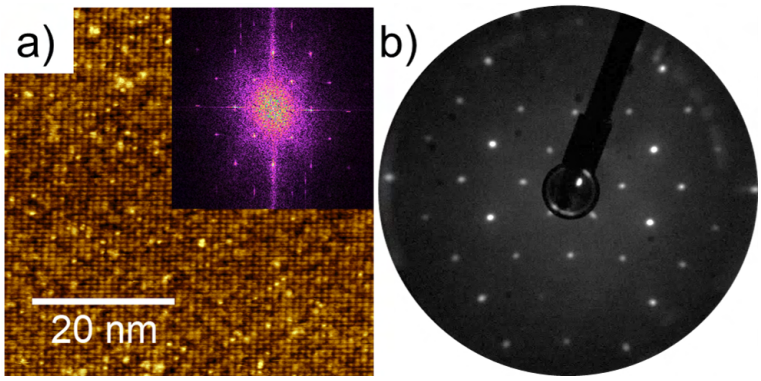

Figure 5.3: a) Atomically resolved STM topography of TiO_2 annealed at 1100 °C with an insert showing a FFT of the surface, which corresponds to the surface's LEED pattern. b) The STM image was measured with the bias of 1.5 V; current 10 pA; the LEED pattern was obtained for electrons with the energy of 56 eV.

are not only annealed, but sputtered and annealed, in order to remove possible impurities from the surface, e.g. several cycles are enough to remove calcium from the rutile's surface [130], [189]. By following this approach, any changes on the surface due to annealing are certain to arise from reduction, and not impurities. For surfaces prepared using such cleaning cycles, the reconstructions are different from the ones that can be seen in Fig. 5.2. At 800 °C and 900 °C, the reconstruction seen is (1x2), not c(2x2) [39], [94], [91], [96]. This implies that the changes are due to impurities and not pure reduction. Moreover, the c(2x2) reconstruction in rutile has only been seen when potassium was deposited on the crystal's surface [190], [191].

The effect of only annealing in UHV on the surface of rutile has been investigated by

other researchers, showing that such conditions lead to the segregation of calcium on the surface of TiO_2 [130], [192], [193], [194]. Zhang et al. (1998) [130] annealed TiO_2 for several hours at 723 °C, and observed rows of calcium atoms which segregated into a layer which they considered to be $CaTiO_3$. Noremberg et al. (1999) [192] annealed TiO_2 for 12 h at 840 °C and observed a c(6x2) reconstruction. Bikondoa et al. (2004) [193] investigated submonolayers of calcium at higher coverages, what they found out was that for submonolayer coverages, rows of calcium atoms can be seen on the surface, and a weak c(6x2) reconstruction is present. The proposed c(2x2) reconstruction may in fact be a developing, incomplete c(6x2) reconstruction. The discrepancy between what Bikondoa et al. (2004) [193] observed, i.e. the weak c(6x2) reconstruction and the c(2x2) reconstruction, could be due to the fact that their low coverage is obtained by molecular vapor deposition and not natural segregation, which may lead to a better-organized layer of $CaTiO_3$.

5.1.3 Changes in chemical composition

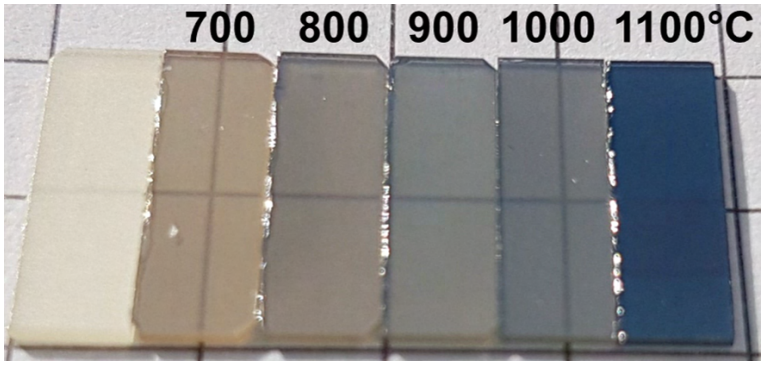

Figure 5.4: The change in color in TiO_2 monocrystals associated with annealing in UHV at different temperatures.

The monocrystals changed during annealing and the changes can be observed macroscopically. Fig. 5.4) shows that the color of TiO_2 changes as a function of annealing temperature, transitioning from brown, through shades of gray to deep blue. Such changes in color were observed many times, for example in [90], where they were tied to the bulk reduction level, with darker blue representing a higher reduction state of the monocrystal. The change in the bulk crystal composition is linked to phase transitions from the surface of the crystal to its bulk. Using XRD tomography, i.e. the gradual removal of the top layers of monocrystal and subsequent XRD investigation, it was demonstrated that annealing at 1200 °C leads to the formation of Magnéli phases [74], with the phases of highest reduction closest to the surface.

The changes on the immediate surface of the crystal were investigated in this dissertation using AES. The spectra obtained for different annealing temperatures show only carbon, titanium and oxygen (see Fig. 5.5a), with the signal for calcium missing (it should be visible at 291 eV [195]). The fact that it is not present, whereas for similar conditions calcium segregation has been observed, is indicative of the fact that the sensitivity of the setup used is too low to detect such a low concentration of calcium. This is especially apparent for the sample annealed

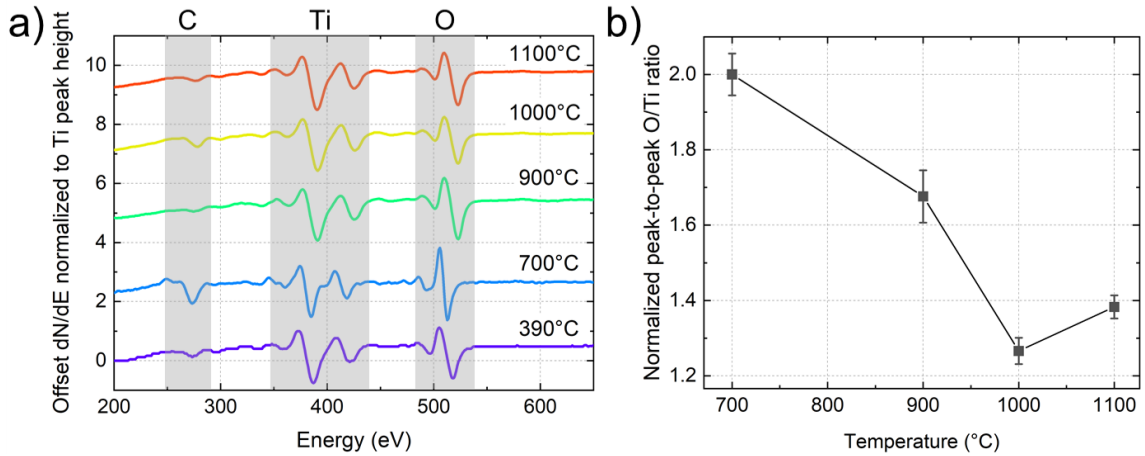

Figure 5.5: a) AES spectra obtained for different annealing temperatures showing the peaks for carbon, titanium, oxygen b) normalized oxygen to titanium peak-to-peak AES ratio as a function of annealing temperature. The marked regions for which peaks corresponding to the elements are present are based on [195].

at 1100 °C, where the $CaTiO_3$ overlayer was already present in part of the sample (as seen in LEED). Based on private communication with Maciej Rogala, it is known that a more sensitive technique (XPS), detects the presence of calcium at 8 % at the annealing temperatures of 1000 °C and a similar duration of annealing.

Using the AES spectra, the state of reduction on the surface was investigated, where the peak-to-peak heights of oxygen and titanium lines were measured and then divided. The resulting values, which were normalized to 2.0 and plotted (see. Fig. 5.5b). What follows it that, with increasing annealing temperature, the ratio decreases and then reaches approximately the same value above 1000 °C. The slight increase in the ratio for 1100 °C may mean that at that temperature, calcium segregation began to play a greater role and the overlayer formed in some parts of the crystal masked the signal from titanium. What makes this more probable is the fact that it has been proposed that the $CaTiO_3$ monolayer is formed when calcium atoms replace titanium atoms [192], which would lead to an increase in the measured ratio.

5.1.4 Changes in electronic properties

The changes in the conductivity of the crystals indicate two processes with opposing effects. The I-V curves depicted in Fig. 5.6a), demonstrate that the nature of the surface changes from very semiconductive to less semiconductive, as expected from the simple reduction of TiO_2. At 1000 °C, however, the surface becomes less conductive. This is demonstrated further in the values of conductance in Fig. 5.6b). This is likely due to the increasing influence of calcium contamination of the surface. The LC-AFM maps (Fig. 5.7) reveal that at these temperatures on the surface, islands of low conductivity appear, which can be related to calcium contamination. The results presented in Fig. 5.6) are calculated based on images, where such regions were masked, but these regions indicate that calcium on the surface of TiO_2 lowers the conductance, even when it is distributed evenly.

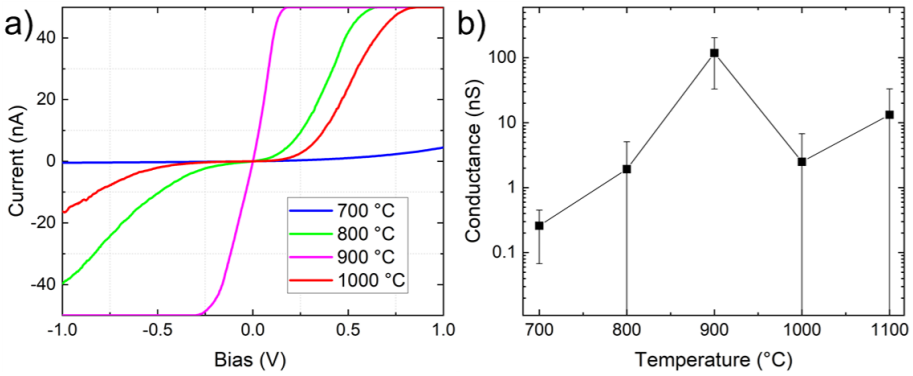

Figure 5.6: a) The average I-V curves and b) values of conductance for TiO_2 surfaces annealed at different temperatures. The source of the data are LC-AFM measurements performed in UHV.

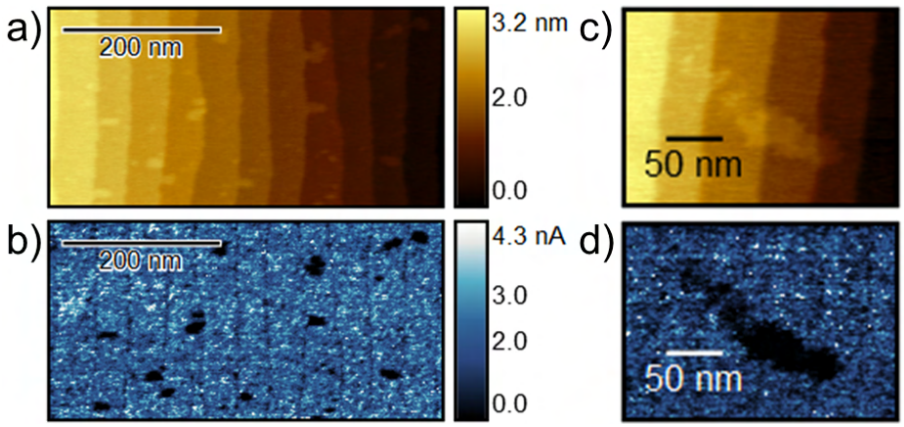

Figure 5.7: The LC-AFM morphology and current maps for a TiO_2 surface annealed at 1100 °C in a), b) on a large scale and c), d) on a small scale. The sample bias was equal to 0.07 eV.

The work function vs. temperature relationship (Fig. 5.8) exhibits the same characteristics as the conductance, with an initial monotonic change in the values and then a break at 1000 °C. The first stage in the range of 700 °C to 900 °C can be, once again, explained by the simple reduction, which increases the defect density of the surface of TiO_2, which, as it has been established [196], leads to a decrease in the work function. At 1000 °C, the change in properties is most likely due to the increasing role of the calcium impurities, with another breaking point at 1100 °C, which, as can be seen in the LEED inserts in Fig. 5.8), corresponds to the total change of reconstruction. The change of reconstruction of the surface naturally leads to another value of the work function, which is what was observed.

The impurity segregation process is far from simple, especially for extreme temperatures. In Fig. 5.9b), three regions of different work functions can be seen. The first is the most prevalent region, composed of atomically flat terraces, and was used for the calculation of the values of the work function of TiO_2 in Fig. 5.8). The second region (labelled A in Fig. 5.8) which only occurs in a small fraction of the images, is a region which spans many terraces and can be seen both in topography (as a rougher area) and on the work function map (as the area of lower work function). The third region (labelled B in Fig. 5.8) is the island which

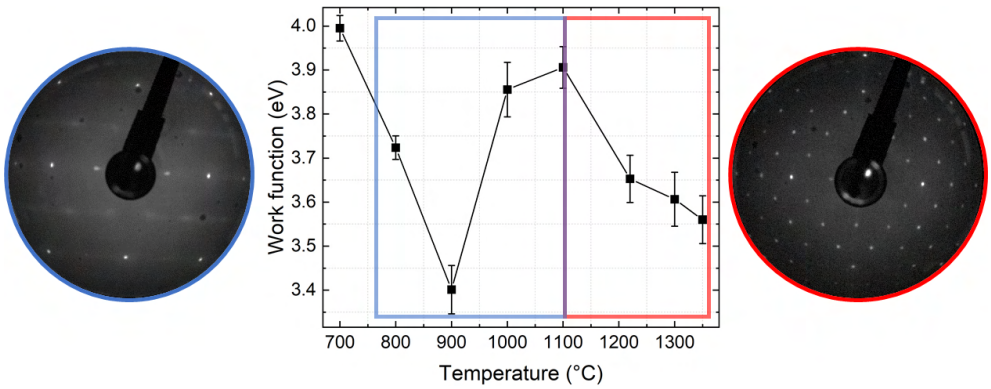

Figure 5.8: The changes in work function measured using KPFM as a function of temperature with marked regions in which the reconstructions shown in the inserts were found.

not only has significant height (of approximately 0.6 nm), but also much higher work function than both the rough region and TiO_2. These two regions are difficult to connect to specific impurities and crystal structures, as at such extreme temperatures, any of the contaminations naturally present in the monocrystals, such as Ca, K or Na (see SIMS profile in Fig. 6.14) could move to the surface and segregate. The disparity between the conductance and work function of such new structures clearly shows that they are of a different nature than the TiO_2 that they grow upon. These maps point to the fact that annealing at such high temperatures affects the crystal significantly, not only in its electronic properties, but also by changing the whole chemical composition of the surface. The fact that these changes are based on unwanted impurities makes such systems difficult to work with and likely difficult to replicate.

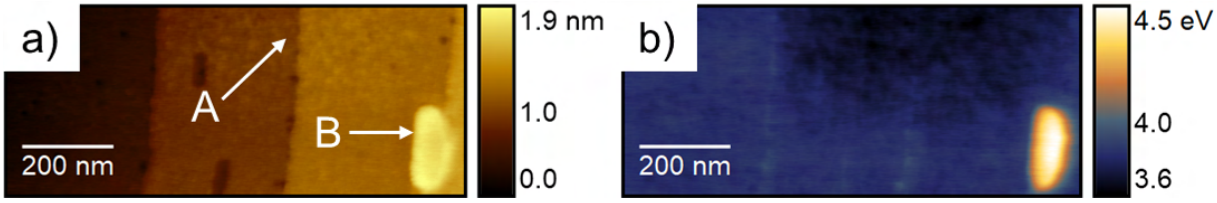

Figure 5.9: The KPFM a) topography and its corresponding b) work function map of a surface annealed at 1350 °C. Three regions of different work function can be seen in the work function map: terraces, the rough region spanning multiple terraces (labelled A) and the island (labelled B).

The results presented for the simple annealing of TiO_2 crystal show that the effects of annealing are not straight forward and that they encompass both the reduction and the segregation of all impurities present in the crystal. The fact that impurities, by definition, are something that is unwanted and not controlled, makes exact quantitative investigation into their nature difficult, however the results qualitatively show that above 800 °C one has to be wary if the observed changes are due to the changes in oxygen concentration or maybe the effect of impurities is mixed in. The batch used in this investigation may contain more contaminants than usual, as experiments using similar annealing temperatures, such as the research reported in [162] or [89], show the typical reconstructions for purely reduced TiO_2 with

no traces of calcium. This unpredictability regarding the impurities and density of defects is not unknown. It has been reported that titanium dioxide and strontium titanite monocrystals differ not only depending on the producer, but even the batch [80], [50]. These inconsistencies may be partially responsible for the great variation in the results in literature. For example, depending on the sample and preparation, the work function of anatase (001) may vary in the range of 3.61 eV to 6.76 eV [197]. Thankfully, there is a preparation method that solves the problem of impurities [130], [189] (see also Fig. 6.14), i.e. the cleaning cycles, which will be described in Chapter 6.

5.2 Oxidation of reduced TiO_2 at room temperature

Crystal oxidation at room temperature was also investigated, in order to shed some more light on the changes that occurred in the previous stages of experimentation.

5.2.1 Experimental

Based on the results from Section 5.1, the crystal which was annealed at 800 °C was selected for the oxidation experiments. Such temperature, as has been shown elsewhere [34], is high enough to remove organic adsorbates. Furthermore, annealing at such temperature should also significantly reduce the crystal in a in order to make changes that will occur during oxidation more noticeable (as crystals annealed at 750 °C are considered slightly reduced [34]).

Oxidation was performed by introducing oxygen gas at the pressure of 5×10^{-8} mbar into the UHV chamber. The dose was equal to 1260 L.

5.2.2 The effect of oxidation on electronic properties

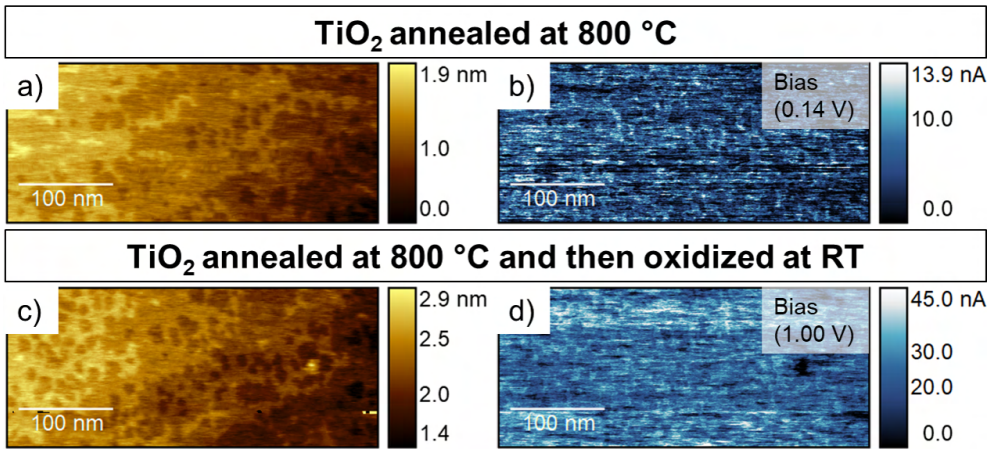

Figure 5.10: The LC-AFM topography and corresponding current maps for a TiO_2 surface which was a, b) annealed at 800 °C and c, d) subsequently oxidized at RT.

The surface morphology was not affected by exposure to oxygen, as can be seen on the topography images before (Fig. 5.10a) and after oxidation at RT (Fig. 5.10c). The electronic properties, however, did not remain unchanged.

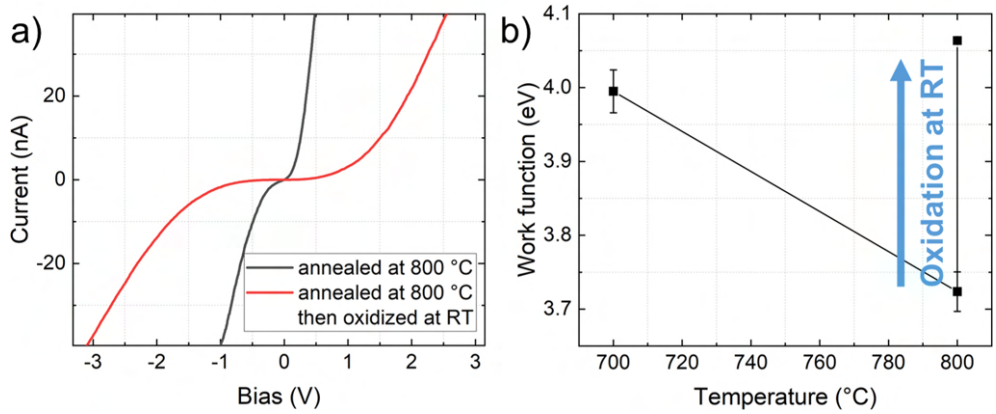

Figure 5.11: The changes in a) I-V curves and b) the work function after oxidation at RT.

There were no new features related to conductance on the current maps (see Fig. 5.10b and d), but the overall conductance of the surface changed drastically. The I-V curves, seen in Fig. 5.11a), show that simple exposure to oxygen at room temperature makes the surface less conductive, which has also been demonstrated elsewhere [34]. Rodenbücher et al. (2018) [34] noticed high-conductance features on the current maps, which they attributed to extended defects, which should remain conductive as they are more resistant to oxidation. Such features were not noticed on the map in Fig. 5.10d), which is most likely due to the fact that the maps are of worse resolution.

Similarly, the work function maps also did not display any features (maps not shown), but the overall value changed after oxygen exposure, which can be seen in Fig. 5.11b). The increase was by 0.34(4) eV, which is more than the increase observed by [34], i.e. 0.1 eV, however the sample used in that research was annealed at a temperature lower by 50 °C, and therefore, it was less reduced and consequently less impacted by oxidation. The value of the work function rises to a value higher than the work function for 700 °C, but it is still far from the value observed for stoichiometric rutile (110) surfaces, which ranges between 5.2 eV [198] and 5.8 eV [196].

The observed changes in electronic properties could be due to the oxidation of the reduced TiO_2 or to an oxidation reaction with impurities. The fact that the experiment was conducted at RT suggests that the changes are most likely due to the healing of oxygen vacancies, which occurs at temperatures above 120 K [126]. It seems unlikely that new oxide phases based on impurities would form at such low temperatures. The fact that the work function value did not reach the values measured for stoichiometric TiO_2 suggests that such oxidation is insufficient to restore stoichiometry of the surface.

Chapter 6

The effect of repeated sputtering and annealing on the electronic properties of TiO_2

Repeated sputtering and annealing is a commonplace, time-tested procedure used in most surface science laboratories in order to obtain a stoichiometric rutile TiO_2 (1x1) surface, which is the starting point of experiments. This surface, as will be shown in this chapter, may not be the same for different publications, which is due to the fact that both of the components of the cleaning cycle (CC) reduce the crystal and therefore change its properties. The manner in which sputtering itself and the subsequent annealing change the stoichiometry and the electronic properties of the surface is analyzed below. Since such preparation never stops at one CC, the effect of multiple CCs is also studied. To bring these results closer to the application side, as well as to better understand the changes at the surface, the crystals were also oxidized at RT and later annealed in oxygen and measured using SIMS.

6.1 Changes induced by sputtering

Sputtering by its nature is a very destructive process, with changes in morphology due to ballistically induced mixing, as well as changes in stoichiometry and electronic properties due to preferential sputtering for multicomponent samples. This process by itself can be used to modify properties of transition metal oxides and understanding its nature is a prerequisite to understanding the changes which occur during CCs in the crystal.

6.1.1 Experimental

To systematically study the changes brought by sputtering, two types of experiments were performed, experiments concerned with changing the fluence for a constant energy of ions, and experiments concerned with changing energy for a constant fluence.

In order to study the effect of fluence, the sample was masked completely, the ion gun was turned on with parameters previously optimized for 2 keV. Subsequently, the sample, and was gradually unmasked. In this manner, a gradient of fluence of Ar^+ was introduced to the sample's surface, which allowed for systematic study. The fluences studied were in the range of 5×10^{15} ions cm^{-2} to 1.2×10^{17} ions cm^{-2}. The sample was bombarded at an angle of 30° with respect to the surface.

The investigation of the influence of ion energy was performed in a different manner.

The ion gun's parameters were optimized for each energy, then a mask was introduced to the system, which contained several holes in various locations, which made it possible to move the mask to control which part of the crystal was covered and which was uncovered. This way, each part of the crystal was bombarded with ions of only one energy. The fluence was constant at 1×10^{17} ions cm^{-2}, while the energies studied varied between 0.6 keV, 1 keV and 2 keV. The sample was bombarded at an angle of 30° with respect to the surface.

Each series of LC-AFM experiments was conducted using one tip in order to make the relative conductance changes in a series easy to compare. The experiments into the fluences and into the energies were, however, done on different occasions, and the same tip could not be used, as it had been destroyed in an unrelated experiment. Consequently, the exact quantitative comparison of conductance may be skewed, as, by definition, conductance is a tip-dependent value. Nonetheless, all of the tips used were of the same type (platinum-iridium coated PPP-contPT tips) and originated from the same batch, which suggests that the tips did not exhibit significant discrepancies. By their nature, KPFM measurements require calibration, so the values obtained are easier to compare, even when the tips differ.

6.1.2 Morphology of the sputtered crystal

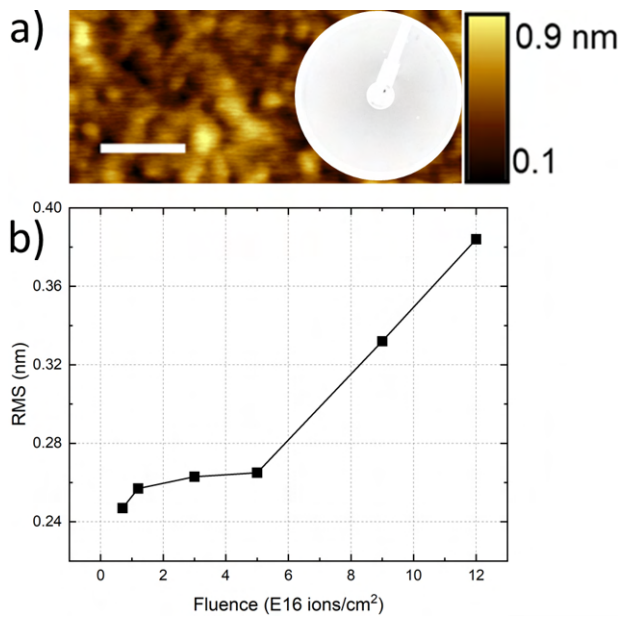

Figure 6.1: a) The morphology of the sputtered TiO_2 surface as shown on an AFM image (scale bar: 100 nm, fluence 1×10^{17} ions cm^{-2}) with an insert showing the lack of a diffraction pattern (electron energy 106 eV); b) RMS changes as a function of the ion beam fluence.

The morphology of the sputtered TiO_2 surface, depicted in Fig. 6.1a), is not composed of terraces, but of grains. The ion beam and the ballistic processes associated with the ion beam irradiation cause the surface to become rough, with the RMS increasing with fluence from 0.24 nm for the fluence of 7×10^{15} ions cm^{-2} and 0.36 nm for the fluence of 1.2×10^{17} ions cm^{-2}. The relationship between fluence and RMS (Fig. 6.1) did not display any sign of flattening out,

but as it has been shown elsewhere [104], at some point increasing fluence does not change the morphology of the surface. This is due to the fact that equilibrium is reached at some point of sputtering and when the fluence is increased further the crystal is only thinned and the surface remains unchanged. Due to this process, the grain sizes reach the end value of approximately 50 nm [104]. In case of the fluences used in this investigation, the grain sizes were of approximately 20(5) nm (as based on an autocorrelation analysis of the conductance structures - see Fig. 6.4), thus the levelling off regime has not yet been reached.

It is a well-known fact that sputtering may induce the formation of crystalline structures on a surface [199]. Furthermore, TiO and titanium suboxides have been observed on electron-bombarded rutile [200]. Following these examples, and the fact that oxygen is preferentially sputtered, it has been postulated that sputtering with Ar^+ leads to the formation of grains of suboxides [104]. The LEED diffraction experiments done on the sputtered surfaces (exemplified by the insert in Fig. 6.1a) did not reveal any diffraction spots, which indicates that there is no long-range ordering on the sputtered surfaces.

6.1.3 Chemical composition of the sputtered crystal

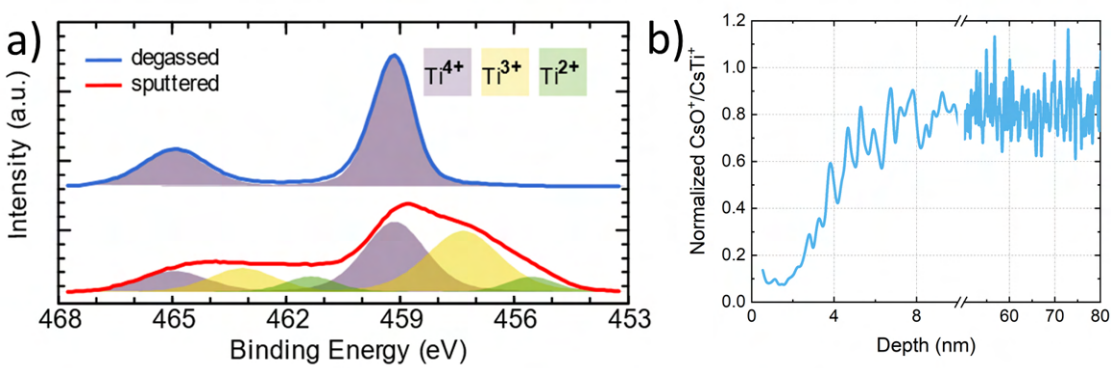

Figure 6.2: a) XPS spectra of a TiO_2 surface which was just degassed and one which was sputtered (fluence 8×10^{15} ions cm^{-2}); b) The CsO^+ to $CsTi^+$ SIMS profile of a sputtered surface (fluence 1.7×10^{17} ions cm^{-2}) normalized to a profile measured for an as-received sample. CsO^+ and $CsTi^+$ ions were used instead of O^+, Ti^+ ions, as in this manner, matrix effect is minimized [182].

Oxygen is preferentially sputtered from TiO_2 which can be clearly seen in the XPS spectra in Fig. 6.2a). The degassed surface contains only Ti^{4+} ions while after sputtering the spectrum becomes more complex, as the signals corresponding to Ti^{3+} and Ti^{2+} are also present. Their proportion is not insignificant, with XPS peak fitting showing that 35 % of titanium atoms on the surface are in the third oxidation state and even 5 % are in the second. This clearly demonstrates that the sputtered surface is nonstoichiometric, and such levels of nonstoichiometry cannot be explained by random, non-interacting oxygen vacancies in a TiO_2 matrix, which implies that the surface should be composed of a suboxide layer. Furthermore, these changes are not only present on the surface, but also in the subsurface layer, as the SIMS profile for the sputtered sample (Fig. 6.2b) shows that the changes in chemical composition reach up to approximately 8 nm in depth. Based on the investigation of Rogala et al. (2013)

[104], it was assumed that the grains were composed of highly defective, suboxide phases of the general formula Ti_nO_{2n-1}.

6.1.4 Changes in electronic properties due to sputtering

The changes in chemical composition and morphology induced by the ion beam dramatically affect the electronic properties of the surface. The sample annealed at 700 °C for 1 h (which was describes in Chapter 5) can be used as the reference point in analysing the changes in conductance. The sample is slightly reduced and free of organic adsorbates, moreover, it is conductive, which is the requirement for LC-AFM. The TiO_2 crystal is relatively poorly conductive, with a conductance of 0.2(3) nS, and its I-V curves show semiconductive behavior. As a reference point for the work function, the UPS-measured work function of 5.3 eV [201] of a pristine stoichiometric crystal was used. The value was assumed to be similar to the starting point of the sputtering experiments. The ion-beam modified surfaces, regardless of the fluence or ion energy, differ drastically in several properties, from the almost-stoichiometric crystal.

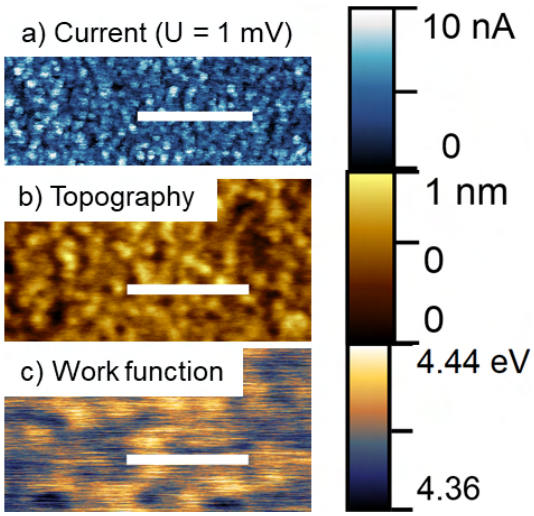

Figure 6.3: a) The LC-AFM map (bias 1 mV), b) AFM topography and c) work function for the sputtered TiO_2 surface. All surfaces were sputtered with a fluence of approximately 1×10^{17} ions cm^{-2}. The scale bar represents 200 nm.

The conductivity of sputtered samples is orders of magnitude higher than for the annealed sample, regardless of the fluence or energy of ions used, as one can see in the Fig. 6.6a), c). Moreover, the character of the I-V curves differs, as they are metallic-like (Fig. 6.5) and not semiconductive-like. The current maps (such as the map in Fig. 6.3a) demonstrate that the sputtered surface is certainly not uniform, but is composed of conductive structures. The high conductance of these surfaces is due to the high percentage of Ti^{3+} and Ti^{2+} ions, which in titanium suboxides are responsible for high conductivity. Furthermore, the sputtered surface is highly defective, e.g. it contains many grain boundaries, and extended defects in transition metal oxides tend to have low resistivity and thus act as highways for the current flow [42], [202].

The electronic properties of the bombarded surface are dependent on the fluence. With

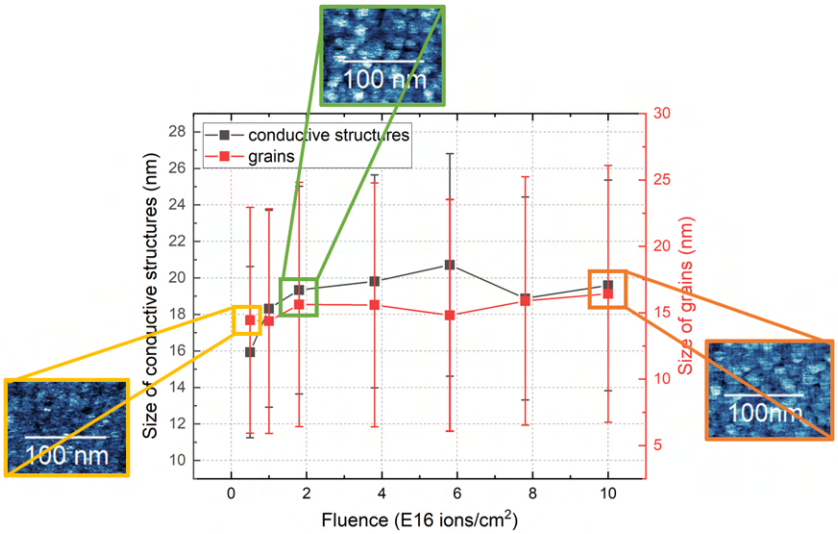

Figure 6.4: The conductive structure size and the grain size as a function of fluence (energy 2 keV). The sizes were calculated based on the autocorrelation maps, where the structure size was assumed to be equal to two standard deviations of the fitted Gaussian function and the uncertainty was 50 % of the FWHM. The inserts depict fragments of LC-AFM current maps.

increasing fluence the surface becomes increasingly more conductive, as depicted by the I-V curves, which become more metallic-like (Fig. 6.5a). As follows, with increasing fluence, the values of conductance increase with an almost exponential growth of the conductance with increasing fluence (Fig. 6.6a). The current maps also evolve, as with increasing fluence, the conductive structure sizes increase and then level out, as can be seen in Fig. 6.4. Furthermore, the conductive grain sizes are equivalent to the sizes of morphological grains (Fig. 6.4).

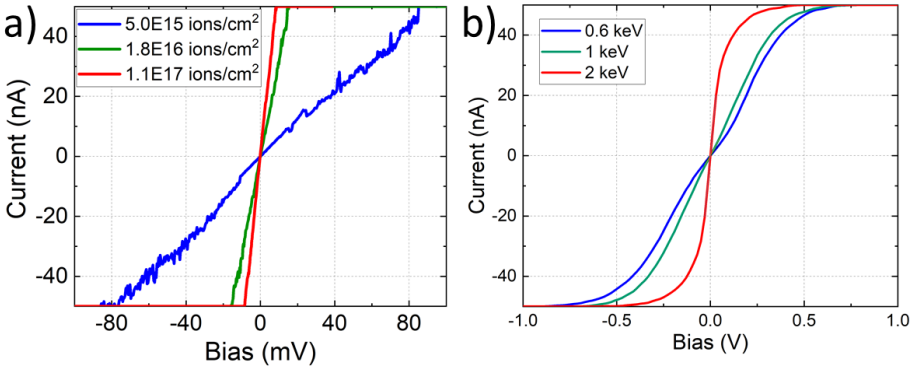

Figure 6.5: The average I-V curves for surfaces which were bombarded a) by different fluences (Ar^+ energy 2 keV) and b) by Ar^+ of different energy (fluence 1×10^{17} ions cm^{-2}).

These changes in the conductance are due to the fact that increasing fluence leads to greater reduction of the surface and therefore a greater number of Ti^{3+} and Ti^{2+} ions, which are responsible for conductivity in TiO_2. The process will cease when the changes in conductance level out for some fluence, which had been shown elsewhere [104]. For fluence values that are high enough, the sputtering of oxygen and titanium reach an equilibrium and no more Ti^{3+}

and Ti^{2+} ions are introduced, even with longer sputtering times. The sample is simply slowly thinned layer by layer.

The work function, which was calculated based on KPFM maps (see Fig. 6.3c), is lower than the work function for the stoichiometric crystal, regardless of the fluence or energy (Fig. 6.6b, d). This is to be expected as, in general, the work function decreases with decreasing order on the surface. Furthermore, the work function decreases when the defect density on the surface increases [196], and a sputtered surface is, without a doubt, defect-ridden. In contrast to the conductance, the work function is not highly dependent on fluence, as can be seen in Fig. 6.6b), because it remains on a similar level, of approximately 4.20(5) eV. This is most likely due to the fact that the work function is strictly a surface quantity, while conductance reaches a greater volume of the sample. The changes in chemical composition are up to the depth of 8 nm, which can be seen in the SIMS profile Fig. 6.2b). Assuming that with increasing fluence more changes are introduced in the subsurface layer, then, naturally, conductance would change drastically, while the work function, which probes the immediate surface, would not be significantly affected.

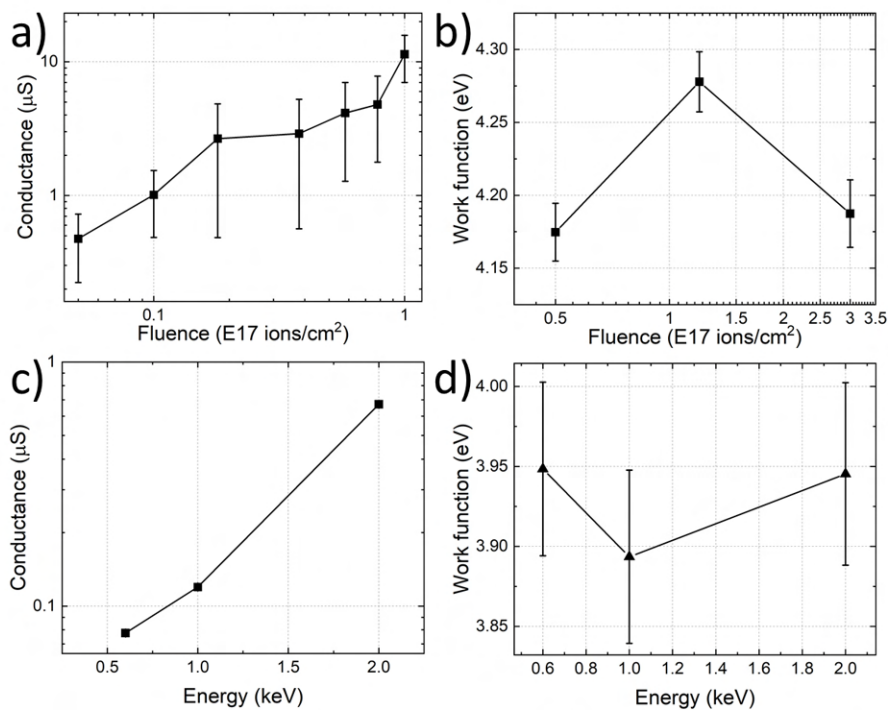

Figure 6.6: The relationship between fluence used during sputtering and the a) conductance and b) work function of TiO_2 surface, while maintaining the same ion energy of 2 keV. The change in c) conductance and d) work function when the sample was sputtered by ions of different energy, but the same fluence (1×10^{17} ions cm^{-2}).

The dependence of conductance on the energy of the sputtering ions (for constant fluence) was also studied. As can be seen on the I-V curves (Fig. 6.5b), greater energies of ions lead to more metallic-like behavior, as depicted on the curves. This is reflected by the values of conductance, which increase with increasing energy of ions (Fig. 6.6c). The differences seen

between the I-V curves for samples bombarded with ions of the same energy (2 keV) from the two experimental series are indicative of the differences between the tips. The averaged curves differ in character. The ones in Fig. 6.5a) reflect higher conductance compared to Fig. 6.5b). This difference most likely stems from the presence of adsorbates on the tip, which would lower the conductance of that series of measurements.

The work function (Fig. 6.6d), once again, is approximately the same (3.95(5) eV) regardless of the parameters of sputtering, and is explained by the same principle as the results for different fluences. The small differences in values between these two sets of data for sputtered samples are most likely due to the fact that the first sputtering of the crystal is most sensitive to the starting conditions. Thus, if the as-received crystals differ in some way in the level of impurities, a proper preparation method (such as the cleaning cycles described below) mitigates the problem as they would be removed from the surface. In the case of the first sputtering, however, the differences is still noticeable, especially when using such a surface sensitive method as KPFM.

The observations described above can be explained based on experiments and simulations done by Hashimoto et al. [203]. They showed that with increasing Ar^+ ion energies, the reduction of the surface, as depicted by the number of Ti^{3+} and Ti^{2+} ions, increases, with first sign on Ti^{2+} at and above 0.1 keV. For higher energies, the number of these ions increased quickly and began to level out at approximately 1 keV. Moreover, the depth and volume of changes induced by the ion beam, as calculated using Monte Carlo methods, was higher at higher energies of ions. These two facts explain why the conductance increased with the increase of ion energy, as more ions were reduced and at a greater volume than for lower energies.

6.2 Changes induced by sputtering and annealing

It can be clearly seen that sputtering introduces a lot of changes to the surface, both in the way of chemical composition as well as morphology. Annealing in vacuum in itself is also a reducing process. However, during annealing a lot of energy is introduced to the system, which allows atoms to diffuse on the surface and from the surface to the bulk and vice versa. The next step of the investigation into the nature of reduction, and the first step in analyzing the changes induced by repeated sputtering and annealing, was to find out how annealing affects a highly reduced and rough surface.

6.2.1 Experimental

The 2 keV sputtered surfaces were annealed at 800 °C for 1 h, and the obtained surfaces were systematically studied. The energy of 2 keV, as well as the relatively high temperature of 800 °C, have been chosen to introduce high reduction to the crystals, in order to measure as great changes as possible, while making sure that the parameters are within the frames of the parameters typically used in other surface science experiments (see Section 1.5.4).

6.2.2 Changes to morphology

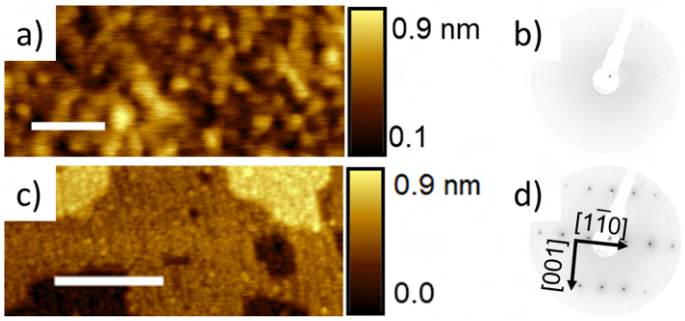

Figure 6.7: a) The morphology of the sputtered TiO_2 surface as shown on an AFM image (scale bar: 100 nm, fluence 1×10^{17} ions cm^{-2}) with b) the corresponding LEED diffraction pattern (energy 106 eV); c) the sputtered and annealed surface as seen on the STM image (scale bar: 30 nm, sample bias 1.5 V, fluence 1.2×10^{17} ions cm^{-2}) with d) the LEED pattern (energy 106 eV).

Annealing the sputtered surface changes the morphology drastically. The sputtered surface was rough and lacked long-range ordering (Fig. 6.7a,b), while the sputtered and then annealed surface was terraced, atomically flat and displayed long-range order (Fig. 6.7c,d). These changes are indicative of great movement of atoms in the crystal. The movement of either titanium or oxygen atoms is required for both the restoration of the crystallographic order of the surface and the restoration of stoichiometry of the surface, which, as it will be shown, follows such changes. This seems to be the case for TiO_2 it is both the movement of interstitial Ti^{3+} and the movement of oxygen atoms which take place when a sputtered sample is annealed [204]. Tracer SIMS experiments had shown that oxygen atoms diffuse at the temperatures of 277 °C to 427 °C, but at higher temperatures the movement of titanium is the kinetically dominant process [204]. On the other hand, the XPS results presented by Rogala et al. (2019) [92] indicate that the reoxidation of the sputtered surface is due to the movement of oxygen and not titanium, because the energy of oxygen vacancy formation on the surface and in the bulk drive the movement of this component. As a further supporting argument to the case of oxygen movement, one may use the ease of movement of oxygen vacancies at room temperature even when the oxygen partial pressure is relatively low [92], while the movement of titanium interstitials at room temperature is energetically highly unlikely [205]. Regardless of the mechanism of point defect movement, as is seen in Fig. 6.7 and in Fig. 6.8, the sputtered surface after annealing is once again stoichiometric and ordered.

6.2.3 Changes to stoichiometry

Annealing is followed by changes in the chemical composition. The surface composition reverts to the composition it exhibited before sputtering, with only Ti^{4+} ions present on the surface, as shown by the XPS spectra Fig 6.8a). Furthermore, the subsurface region also does not remain unchanged. This can be seen in the SIMS profiles, which show that simple annealing of the surfaces leads to the diffusion of ions, which restore the surface stoichiometry,

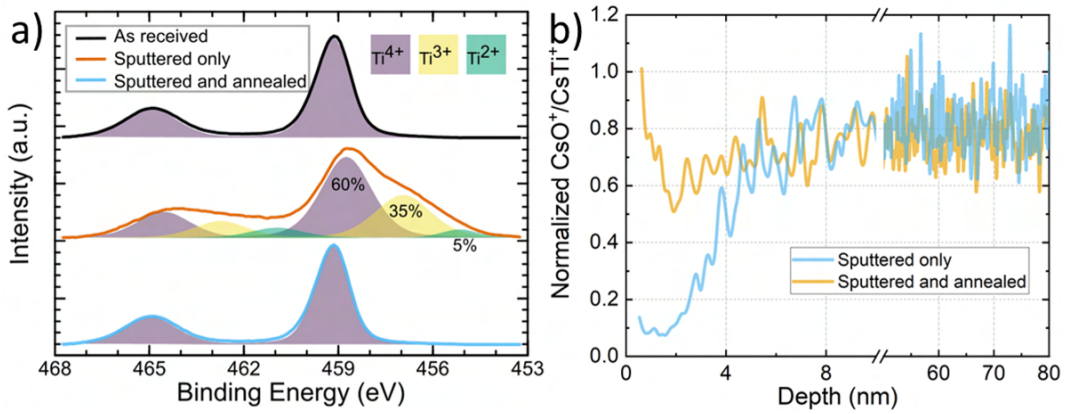

Figure 6.8: a) The XPS spectra for the as-received and sputtered only and a surface that was sputtered and subsequently annealed. b) The comparison of the SIMS oxygen to titanium profiles for the sputtered sample and the sample that was sputtered and then annealed. The profiles were normalized to the as-received sample.

and the non-stoichiometries are redistributed in the bulk, as the profiles reach the same values for approximately 5 nm. The ions which restore the stoichiometry must come from the bulk, because the sample is in a vacuum and undergoes reduction, so there is no other source of oxygen. The small dip in the oxygen-to-titanium signal in the subsurface region, as compared to the as-received sample, demonstrated, that one cycle of sputtering-annealing affects the subsurface layer. The difference in the dip value between sputtered and sputtered and annealed profiles coupled with the equal depth at which the profiles reach stoichiometric values suggests that the non-stoichiometry is redistributed in a great volume.

6.2.4 Changes to electronic properties

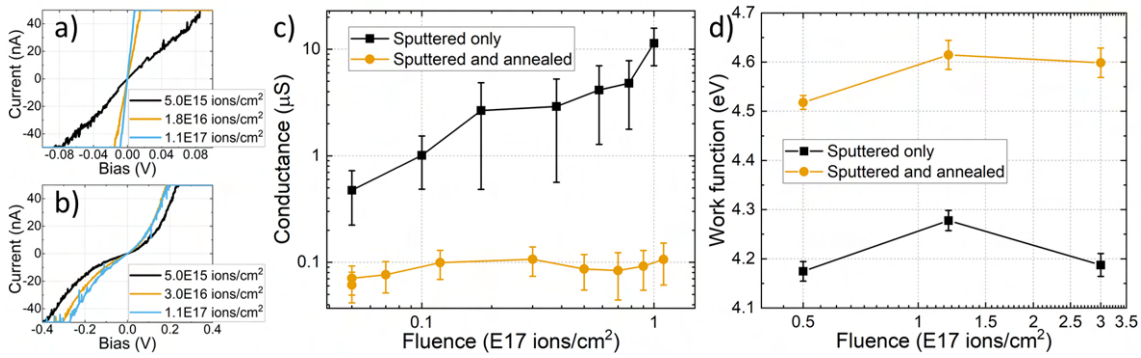

Figure 6.9: The average I-V curves collected for a) sputtered and b) sputtered and annealed surfaces for different fluences; the effect of received fluence on c) conductance and d) work function.

These major changes in stoichiometry of the surface induce changes in its conductance. With the annealing, the change from metallic-like I-V curves (Fig. 6.9a) to semiconductive-like curves (Fig. 6.9b) follows. Accordingly, the values of conductance drop by one or even two orders of magnitude (Fig. 6.9c), and reach approximately the same value, independently of the

ion beam fluence. No matter the initial fluence, the final conductance reaches approximately the same value. The I-V curves (Fig. 6.9b) support this interpretation. The current maps (not shown) show surface uniform in properties, with no grains of high conductance. The maps of the work function are also uniform, and the value of the work function increases dramatically after annealing from 4.25(5) eV to 4.55(5) eV (Fig. 6.9d). Based on the work function values, no clear correlation can be drawn on the work function-initial fluence dependence.

The changes in electric properties can be explained based on the evolution of chemical composition seen in the XPS and SIMS measurements. Since the reduced titanium ions are the main components of the electrical conductivity in titanium dioxide, the restoration of stoichiometry of the surface, seen in the Fig. 6.8a), explains why the conductance suddenly drops. The SIMS spectrum in Fig. 6.8b) indicates that there is a region below the surface which is not stoichiometric. It is most likely slightly different for different initial fluences, which would explain the differences between the I-V curves. Comparing the value of conductance for the sputtered-annealed surfaces with the conductance value of the surface which was just annealed at 800 °C (Fig. 5.6c), it can be seen that the additional reducing component in the form of sputtering does play a role in determining the final properties of the surface, as the surface after one cycle has the conductance of approximately 100 nS, compared to 1 nS for a surface just after annealing.

The increase in the work function due to annealing is also tightly connected to the changes on the surface, and with the restoration of stoichiometry and order the work function naturally increases. Nonetheless, the work function after one cycle is equal to 4.55(5) eV, which is below the value reported for stoichiometric rutile (110) surface, i.e. 5.3 eV [201]. This indicates that the changes under the immediate surface coupled with point defects on it, lower the value significantly compared to the one observed for stoichiometric surfaces. Comparing this value with the one obtained for just annealed crystal 3.72(3) eV (Fig. 5.8) one can see that using one cycle as compared to just annealing gives a more stoichiometric surface.

6.3 Changes induced by repeated sputtering and annealing

Sputtering and annealing by themselves reduce the TiO_2 crystal, yet after one such cleaning cycle, the surface is stoichiometric. The work function of the surface returns to values close to values of the stoichiometric surface, yet the conductivity increases by two orders of magnitude, as compared to the slightly reduced crystal. This shows that changes in the crystal's subsurface composition do, in fact, occur as a result of these processes. Since, typically, multiple cycles of sputtering and annealing are performed, the effect of the many cleaning cycles had to be investigated to find out if the changes are cumulative and if they drastically change the surface of TiO_2.

6.3.1 Experimental

As it was described in Section 1.5.4, various different experimental parameters are used when performing cleaning cycles, and, just as in the case for one cleaning cycle, the temperature

of 800 °C and Ar^+ energy of 2 keV were chosen to introduce changes as extensive as possible while still working under parameters that are used in typical surface science laboratories. The ion fluence introduced during one sputtering was approximately 8.6×10^{15} ions cm^{-2}.

The morphology, crystallography and electronic properties were measured systematically after 1, 5, 10, 15, 20, 25, 30, 35, 40 and 50 cleaning cycles. The changes in chemical composition were measured using XPS and SIMS. For XPS measurements the changes were observed in situ for three CCs, while SIMS profiles were obtained ex situ for a sample which underwent 11 CCs (here, the fluence was 2×10^{16} ions cm^{-2}).

To find out the effect of oxidation on the 50 CCs reduced sample, the sample was first oxidized at RT and studied and then annealed in oxygen at 800 °C and once again measured. In both cases the isotopic oxygen ^{18}O was used (pressure 5×10^{-8} mbar). The sample was then taken out of the UHV system and measured using SIMS. As a reference, an as-received TiO_2 monocrystal was also annealed at 800 °C in the isotopic oxygen and measured using SIMS.

6.3.2 Changes in morphology with the increase in the number of CCs

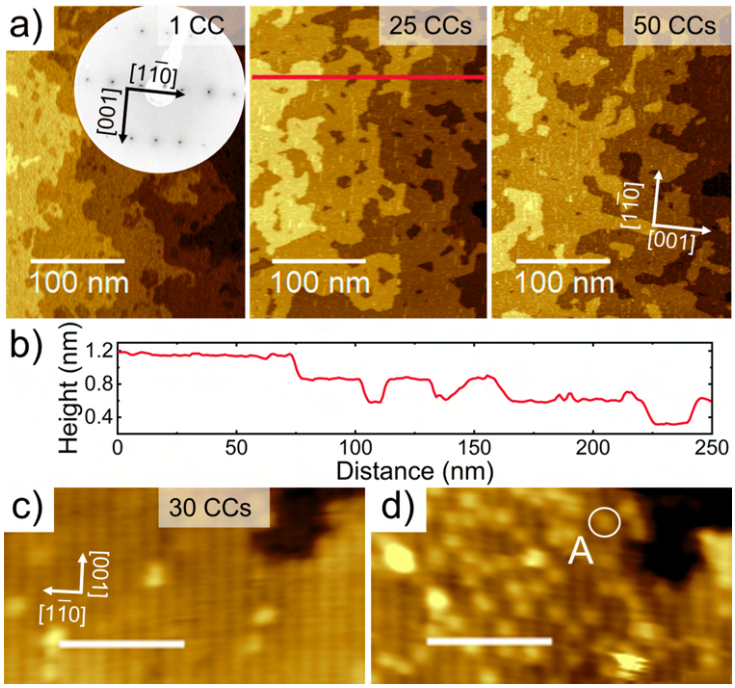

Figure 6.10: a) The STM morphology of the TiO_2 surface after 1 CC, 25 CCs and 50 CCs, with an insert showing the LEED pattern the 1 CC sample (electron energy 106 eV); b) the line profile through the terraces for the 25 CC sample, marked as the red line in a); STM images c), d) (scale bar 5 nm) showing the same area of the 30 CCs surface imaged using the same tip, but during scanning it changed its orientation, composition, structure or apex. The region marked with the circle and labeled A is an OH^- group. All STM images were collected for the sample bias 1.75 V and the current of approximately 20 pA.

As can be seen in the Fig. 6.10a), successive CCs affect the morphology of the surface. The increase in the number of cycles is correlated with the terraces' increase in size, and their

borders become more compact. The line profile through the 25 CCs surface 6.10b shows that the terraces are tens of nanometers in length and that the pits present on individual terraces have depths of one step edge. In all cases, the LEED patterns show a diffraction pattern characteristic of (1x1) stoichiometric reconstruction (exemplified by the insert in Fig. 6.10a). Since the heavily reduced rutile (110) surface takes the form of (1x2) reconstruction [206], [207], this shows that, with LEED sensitivity, the surface can be considered stoichiometric. Atomic-resolution STM images were also collected (see Fig. 6.10c, d), and they show that the surface is composed of atomic rows following the [001] direction. Both of the STM images were collected using the same tip, with the same positive bias, and measured the same place, yet they depict the surface differently. This is because during scanning, the tip was modified, and its orientation, composition, structure or apex changed, which led to different orbitals being used for imaging. Similar observations were made elsewhere, also revealing that such modification of the tip may even bring about the inversion of the contrast of the image [148]. The empty states of the TiO_2 (110) surface can be seen on the STM image for 30 CCs (Fig. 6.10c), where bright rows are associated with Ti^{4+} ions nested between oxygen rows [30].

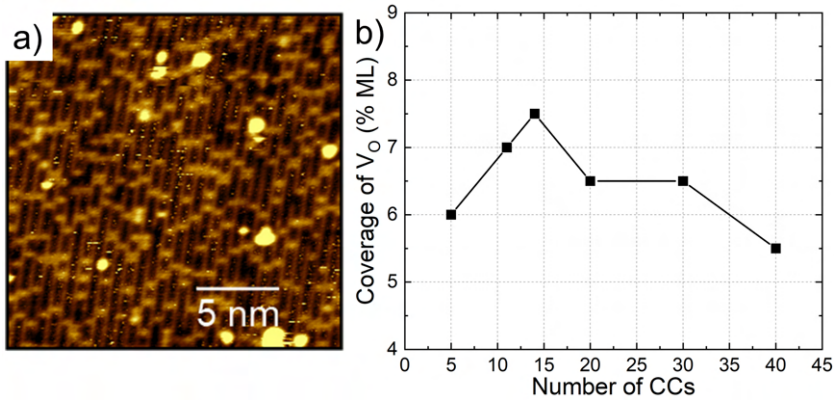

Figure 6.11: a) A typical STM image on which the coverage calculations were based. This image shows the topography of an 11 CCs sample (sample bias 1.7 V and current 11 pA). b) The relationship between the coverage of oxygen vacancies and the number of cleaning cycles performed on the surface.

Based on the atomically resolved STM images, an investigation into the dependence of the coverage of point defects on the number of cleaning cycles was performed. Typically, such investigations are conducted at low temperatures, where imaging at such resolutions is easier, as oscillations due to the temperature of both the tip and the sample are much lower. Furthermore, low temperatures hinder the movement of atoms and significantly lower reaction rates. Additionally, at low temperatures, the pressure in the UHV systems is lower than at RT, as the atoms and molecules tend to remain on the cold chamber surfaces (as is the principle of the cryogenic pump). In low-temperature investigations, oxygen vacancies on the surface can easily be distinguished from hydroxyl groups [208]. It has been reported that surface oxygen vacancies react quickly with residual water, even in UHV systems [208]. Moreover, oxygen vacancies are the site of water dissociation, with each oxygen vacancy catalyzing the formation of two hydroxyl groups [209], [208]. Due to lower resolutions and a higher base pressure, an assumption was made that all of the bright point defects that were seen were hydroxyl groups,

and that their number is tightly correlated with oxygen vacancies on the surface. Such OH^- group can be seen in Fig. 6.10d) . The obtained relationship between the coverage of oxygen vacancies and the number of performed CCs is represented in Fig. 6.11b). The coverage of such defects was studied based on 20 nm per 20 nm images, such as the one in Fig. 6.11a). The typical coverage of oxygen surface vacancies observed in the literature varies from 2.5 % ML for 9 CCs [208], through 6.1 % ML for 32 CCs, and 8 % ML [210] or 15 % ML for multiple cycles [211]. Accordingly, this means that the values obtained in this investigation were in agreement with the typical concentration observed in other publications. Wendt et al. (2005) [208] noted that the most common value was in fact approximately 5 % ML, which is close to the average of 6.5 % ML obtained here.

6.3.3 Changes in chemical composition with the increase in the number of CCs

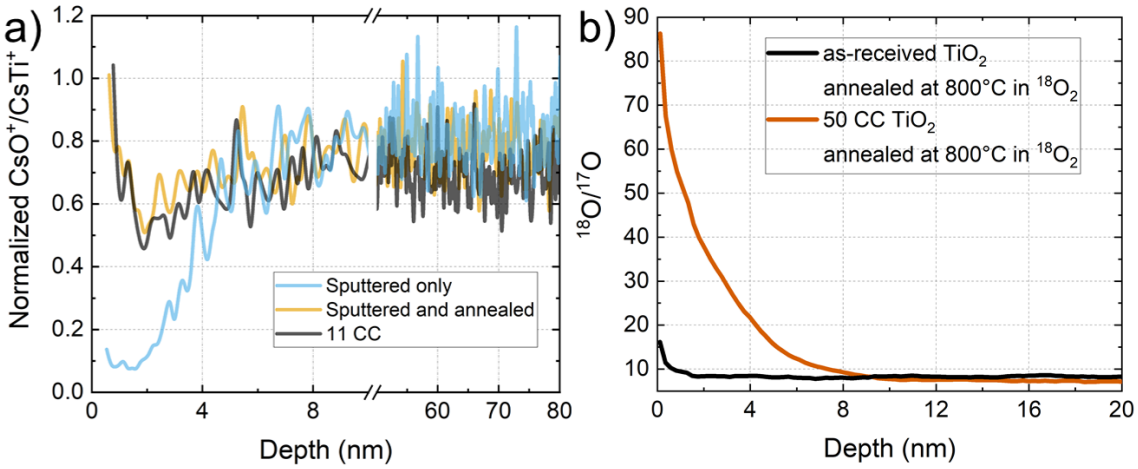

Figure 6.12: a) The CsO^+ to $CsTi^+$ raw SIMS profiles for the sputtered, sputtered and annealed (i.e. after 1 CC), and the 11 CCs surface. The profiles are normalized to the as-received sample. b) The SIMS profiles of two samples annealed in isotopic oxygen at 800 °C, one of which underwent 50 CCs, while the other was not subjected to any cycles. The ^{17}O isotope was the reference, because the signal for ^{16}O saturates the detector. Oxygen isotope profiles were 10-pt averaged to aid interpretation.

The STM images and LEED patterns show that the surface is stoichiometric, with a small percentage of oxygen vacancies. Furthermore, the XPS spectrum after three CCs demonstrates that all the titanium ions were in the fourth oxidation state. Due to the reductive nature of the processes involved in CCs, changes in compositions are to be expected in the bulk of the crystal. SIMS profiles were measured to find out their nature. As can be seen in Fig. 6.12a), the profiles for both one and eleven cycles show non stoichiometry for depths up to 4 nm. These two profiles do not show significant differences in the subsurface layer composition, which suggests that the non-stoichiometry is redistributed gradually throughout the crystal. All the profiles, even for 80 nm, do not reach the stoichiometric value of the oxygen-to-titanium ratio, but such an effect has already been observed for TiO_2 [180]. In this work, it was assumed that the ratio of approximately 0.8 corresponds to the stoichiometric ratio.

To find out the extent of the changes in the composition of the crystal, the 50 CCs crystal was annealed in isotopic oxygen and its profile was compared to the profile obtained for an as-received crystal prepared in the same manner. The profiles, which can be seen in Fig. 6.12b), show that the depth of penetration for the 50 CCs sample was much higher than for the reference sample, with the ratio reaching a constant value at approximately 10 nm, compared to 1 nm. Since the range of argon ions of 2 keV in TiO_2 is equal to 2.6 nm [203], the SIMS profiles show that the changes associated with multiple cycles reach greater depths. Furthermore, the values of the isotopic ratio are larger by an order of magnitude at the 50 CCs surface. Assuming that the signal from isotopic oxygen corresponds to defect states introduced by the preparation method, it can be seen that not only do the defects reach a greater depth than for the as-received sample, but also the density of defects is much higher.

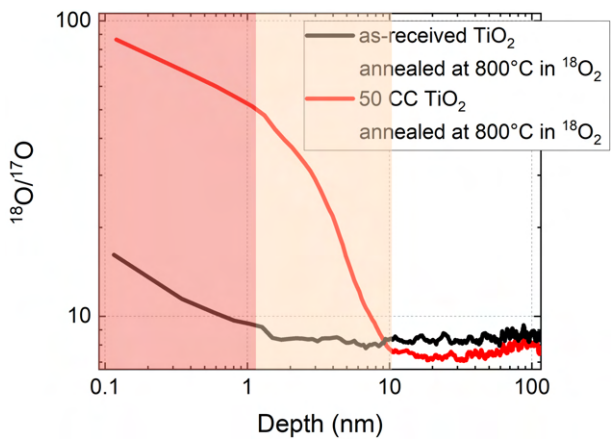

Figure 6.13: The same SIMS profile as in Fig. 6.12b), but in log-log scale, with three regions marked, one presumed to be associated with reaching equilibrium conditions, and one associated with the incorporation of oxygen into the nonstoichiometric subsurface layer, and the last one which is the bulk region.

Three regions of interest can be discovered by analyzing the same graph for isotopic oxygen ratios, but on the log-log scale. The first region is the same for both samples, and it ends at about one nanometer. The same slope and associated depth suggest that this is due to the initial equilibrium setting. In the case of the 50 CCs sample, it can be noticed that the slope changes first from 1 nm to 2 nm, and then from 2 nm to 10 nm. These depths may correspond to the immediate surface and the subsurface, respectively. Afterwards, the ratio levels out to the bulk value. For the as-received TiO_2 sample annealed in oxygen, the region with a different slope is very narrow, i.e. approximately 1 nm, and then the bulk ratio is reached. This difference in the penetration and the presence of an additional region of high slope in the case of 50 CCs sample indicates that this sample had been modified by the cycles, not only on the surface, but also at the subsurface region. The presence of the region of high slope might mean that another diffusion mechanism is present in this sample, e.g. a fast diffusion path, due to the high density of extended defects.

In the study of oxide crystals one must be also wary of impurities. In general, rutile crystals are very pure, which can be seen in Fig. 6.14, as the intensities of the SIMS signal

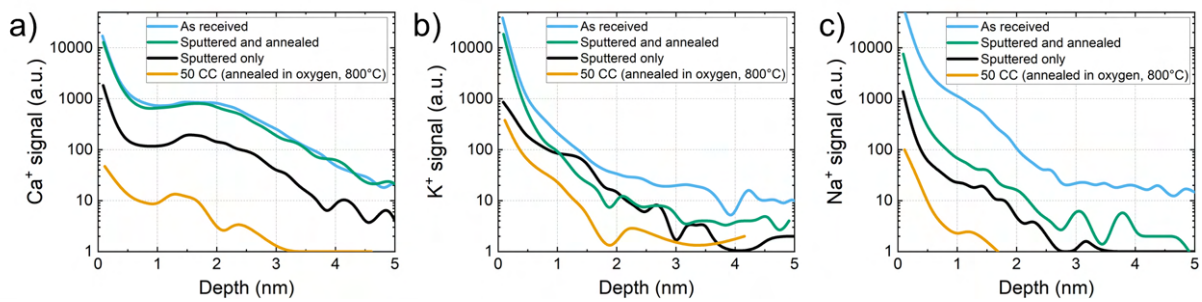

Figure 6.14: SIMS profiles showing the levels of typical impurities (Ca^+, K^+, Na^+) on TiO_2, one of an as-received surface, and one which underwent sputtering or cleaning cycles.

of the typical impurities are on a very low level. They are present in all of the crystals that are presented in the profiles and follow the same general trend, wherein their concentration is highest near the surface and then drops very quickly with depth. The signal values at the immediate beginning of the spectra should be interpreted with caution, as at the start of the measurement, the steady state sputtering conditions are not yet reached [177]. Segregation of impurities is a well-known process, which occurs due to the differences in the surface tensions of impurities and the base crystal, which atomically corresponds to different strengths of interactions between the component atoms.

The analysis of the profiles reveals that the level of impurities varies between samples. For example, the profile for the sputtered-only crystal shows lower concentrations of impurities than both the as-received and 1 CC samples. This diversity is to be expected, as different batches of monocrystals may differ in purity, but what is more interesting is the way the three profiles of the impurities look like compared to the 50 CCs sample. Its profile shows signals that are orders of magnitude lower than the signals for all impurities. This is due to the fact that with each instance of annealing, the impurities diffuse to the surface, and then during sputtering, they are removed ballistically. With each cycle, the general level of impurities is lowered, but of course the bulk provides a steady source of these impurities, so even after 50 CCs, some Ca^+, K^+, Na^+, etc. can be found on the surface. This property of the cleaning cycles has been used successfully to clean monocrystals, and for TiO_2, it has been reported that several cycles are enough to purify the crystal surface of the most common impurity, i.e. calcium [130], [189]. It must be noted that the level of impurities measured using SIMS as compared to signals measured for titanium and oxygen, is extremely low, even in the case of as-received crystals. The technological processes over the years have been perfected over the years and the quality of monocrystals is high, which has a been also reported in research by Wrana et al. (2017) [89], where it was shown that the levels of impurities are at or below ppm levels .

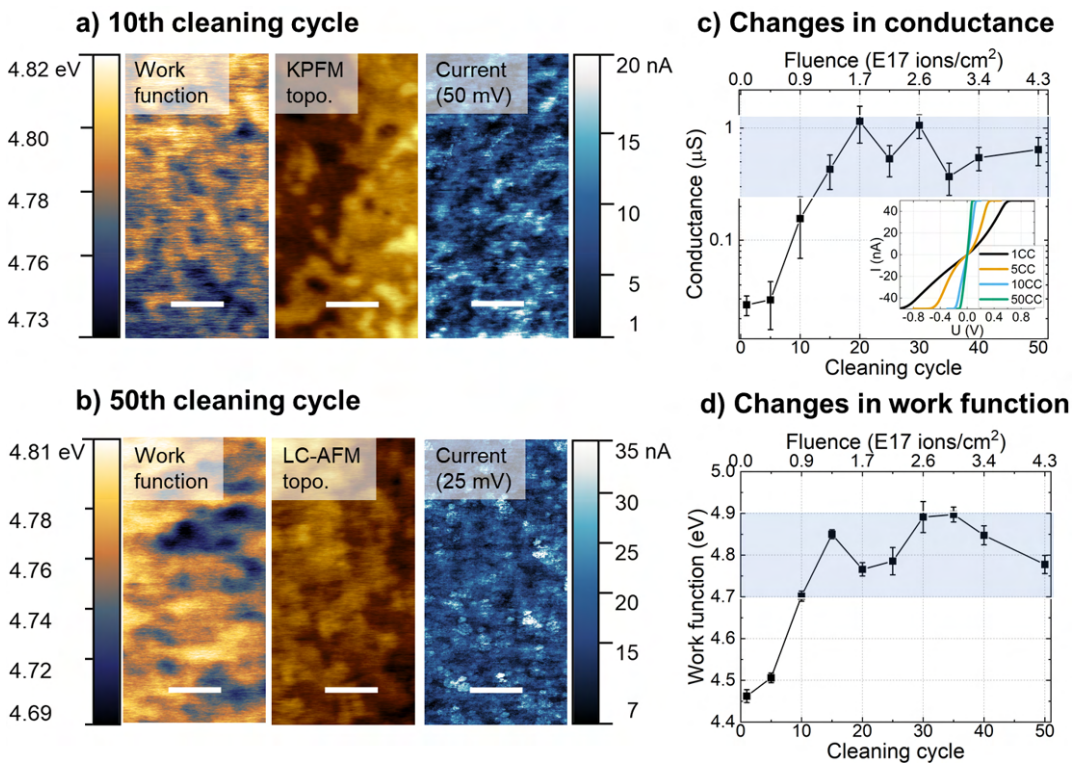

Figure 6.15: Typical maps of work function, current and morphology for the sample after a) 10 CCs and b) 50 CCs. The scale bar represents 100 nm. The relationship between c) the conductance and d) the work function as a function of the number of cleaning cycles that the sample underwent. The insert in c) shows the changes in average I-V curves with the increase in the number of CCs.

6.3.4 Changes in electronic properties with the increase in the number of CCs

The steady reduction introduced by the cleaning cycles affects the surface conductance. As can be seen in Fig. 6.15c), the conductance of the surface increases rapidly with approximately the first ten cycles and then it reaches the levelling out level. The value of conductance increases more than 20 times from 27(6) nS for 1 CC to 640(190) nS for 50 CCs. The insert in Fig 6.15c) with I-V curves clearly displays the nature of the surface changes. At first, the surface is semiconductive-like, and then it becomes increasingly more conductive. For 50 CCs, it shows an ohmic-like behavior, which is on the level of the sputtered-only surface. The current maps, seen in Fig 6.15a) and b), do not reveal any identifiable features, which suggests that the overall level of conductivity of the subsurface layer changes with the increase in the number of CCs.

The changes in conductance can be explained in the same manner as for the changes at 1 CC, i.e. the changes in composition of the subsurface due to the overall reduction of the crystal are what is inducing the change in the conductivity of the crystal. Each following CC further reduces the crystal, induces changes, and possibly phase transformations. However, at a certain point the surface-sensitive technique, LC-AFM, is not sensitive enough to detect such phase changes, hence the levelling-off region. As demonstrated in the previous section,

SIMS measurements indicate that these reduction-associated defects are redistributed in the bulk quite uniformly, which makes LC-AFM unable to measure them.

In relationship between the work function and CCs is very similar, with changes being most prominent for the first 10 cycles, after which the plateau region is reached. The work function maps, e.g. Fig. 6.15a), follow the morphology of the surface, with some contrast changes on the terrace borders.

The changes in the work function may be due to the effect of reduction or due to the effect of the gradual removal of impurities from the surface. The effect of oxygen vacancy coverage on the work function was explained by Onda et al. (2004) [196] as the change in surface potential caused by reduction. Oxygen is an element characterized by strong electron affinity, which causes the oxide surface to become negatively charged. The reduction process removes oxygen, which reduces the negative charge, which in turn allows electrons to leave the crystal more easily, i.e. it lowers the work function. However, the oxygen vacancy coverages that were measured in this work showed that they were approximately constant (Fig. 6.11b), and accordingly, the leveling off in the work function seen in Fig. 6.15d) cannot be due to reduction. Thus, the changes must be due to the decreasing concentration of impurities on the surface, which is seen in SIMS profiles in Fig. 6.14.

The work function plateau which is reached with increasing number of CCs has the value of 4.8(1) eV, which is relatively close to the lower bounds of the range of values reported for stoichiometric TiO_2 (110) surfaces, i.e.: 5.2 eV [198], 5.3 eV [93], 5.35 eV [212], 5.5 eV [213] and 5.5 eV to 5.8 eV [196]. The wide distribution of values has, in fact, been explained by the differences in the defect densities on the surfaces, with the work function decreasing with increasing defect coverages [196]. What is telling is the fact that Onda et al. (2004) [196] reported that in their own experiments, following the same preparation method, they saw a variability in the work function, in the range of 5.5 eV to 5.8 eV, so there must be some variability in the monocrystals themselves. The fact that the leveling-off value of the work function is so close to the stoichiometric values shows that sample preparation using many cleaning cycles allows, in case of work function, to obtain a surface which is very close to the stoichiometric one.

6.3.5 One large cycle or multiple small cycles: the effect on electronic properties

Comparing the results for one single CC and multiple CCs provides the answer to another question. Does one cycle affect the electronic properties of the crystal in the same manner as multiple cycles of the equivalent fluence?

As can be seen in Fig. 6.16a), for low fluences, the values of conductance are approximately the same, as the sample is semiconductive in nature. With an increasing number of cycles, the situation changes. Above 10 CCs, the conductance rapidly increases and then reaches the plateau of relatively high conductance. The divergence between these two sets of data can be demonstrated and its explanation lies in the way that sputtering works. Continuously increasing the fluence does not contentiously increase the level of reduction of the surface.

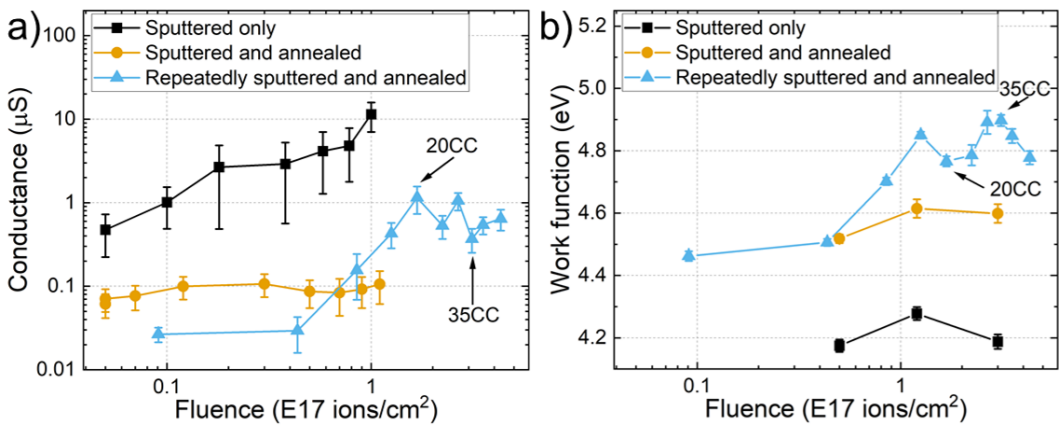

Figure 6.16: The values of a) conductance and b) work function as a function of fluence received depending on the preparation method, i.e. just sputtering, sputtering and annealing, or multiple cycles of equivalent cumulative fluence.

Instead, an equilibrium is reached, and the sample is at some point simply thinned [104]. On the other hand, when the fluence is introduced in a multi-step manner, i.e. each time the crystal is reduced during sputtering, then the surface is reoxidaised during annealing. Then, it is once again sputtered, so the equilibrium in this case is not reached during the sputtering. Thus, the conductance for multiple CCs increases, while for one CC of equivalent fluence, the value stays constant.

For the work function (see Fig. 6.16b), the equilibrium of sputtering seems to also have been reached, and the values for one CC reach the same value, which is lower than the one for multiple CCs. As it has been described in Section 6.3.4, one CC is typically associated with highly defective surfaces. Multiple cycles of equivalent fluence differ in such a manner that even though they reduce the crystal further due to the additional annealing time, they also provide more time at high temperatures for the reoxidation and recrystallization of the surface. Thus, the end result is more stoichiometric and its work function is higher.

The reason why cycles are performed many times is that the surface becomes more stoichiometric, as the number of the cycles is increased, whereas for a single cycle, even with increasing fluence, it never becomes more stoichiometric. Furthermore, performing multiple cycles leads to more reproducible surfaces and therefore more reproducible results, as both the conductance and the work function reach a plateau value after approximately 10 CCs. It is possible to obtain the same surface properties after annealing for sufficiently high fluences, i.e. in the equilibrium regime, but the surface would be of an inferior stoichiometry, and it would not be suitable for application in atomically resolved studies. This, coupled with the higher purity of multiple-cycle surfaces (see. Section 6.3.3), makes multiple cycles a far better manner of preparing a TiO_2 surface.

6.4 The effect of subsequent oxidation of a sample after 50 CCs

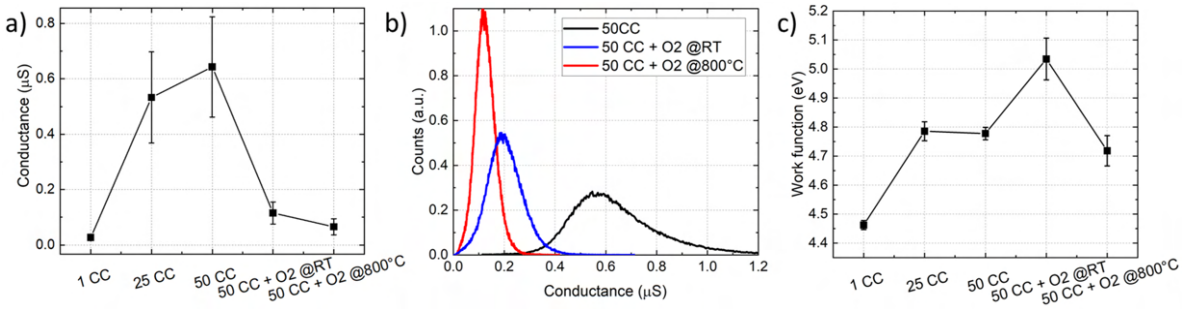

Figure 6.17: The effect of the RT oxidation and oxidation at 800 °C of the 50 CCs sample on the electronic properties. The changes in a) conductance values, b) shape and position of the conductance histograms and c) the value of the work function. The oxygen exposures for the measurements of the work function were 310 L, and for the conductance 1900 L for RT. The sample was then annealed in oxygen at 800 °C for one hour.

To find out if the changes induced by sputtering and annealing are reversible, the crystal was oxidized at room temperature. As can be seen in Fig. 6.17a), the conductance of the surface drops significantly after the exposure to oxygen. Furthermore, the conductance histograms narrow after exposure, which suggests that the surface becomes more homogeneous. These two facts indicate that oxidation takes place, with less conductive defects being present after the oxidation at RT. The values of conductance, however, do not reach the level which was observed after one cleaning cycles (27(6) nS for 1 CC as compared to 120(42) nS). This shows that not all of the defects introduced during the preparation are healed during the RT oxidation. The exposure to oxygen at temperatures higher than 120 K leads to surface oxygen vacancy healing [126], but this process, even at RT, does not heal all of the oxygen vacancies on the surface [92], [127]. Furthermore, oxidation at RT does not heal subsurface oxygen defects present on vacuum-annealed surfaces [196]. Accordingly, simple exposure to oxygen at RT does not heal the surface and subsurface completely, and therefore the conductance remains relatively high.

The work function of the RT-oxygen-exposed sample increases from 4.8(1) eV to 5.0(3) eV (see. Fig. 6.17c), which brings it even closer to the values observed for stoichiometric TiO_2, i.e. from 5.2 eV [198] to 5.8 eV [196]. This indicates that the surface became more stoichiometric, and fewer oxygen vacancies are present as compared to the 50 CCs surface.

As a further step in the investigation, this RT-oxidized surface was annealed at 800 °C at the oxygen pressure of 5×10^{-8} mbar. The results are quite surprising, as the work function decreased compared to the surface oxidized at room temperature (Fig. 6.17c). Furthermore, the conductance did not change significantly (Fig. 6.17a and b). Typically, oxidation leads to an increase in the work function and a decrease in conductance.

The fact that the work function decreases suggests that either another oxide phase has

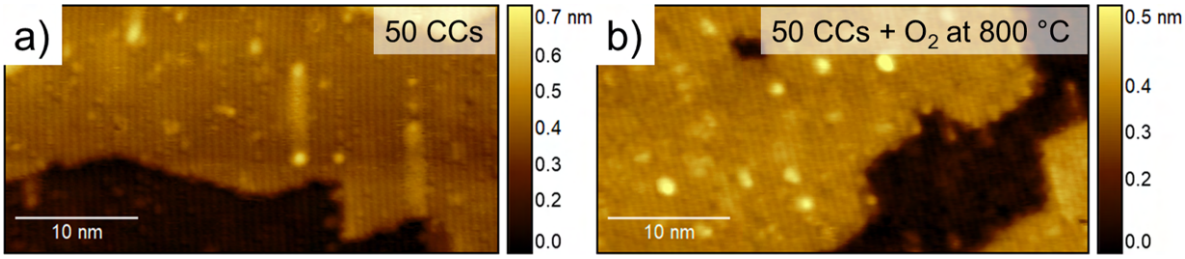

Figure 6.18: The STM morphology of the TiO_2 surface which a) underwent 50 CCs and b) underwent 50 CCs and then was annealed at 800 °C in oxygen (5×10^{-8} mbar) for one hour. The images were collected using the sample bias 1.7 V and the current of 10 pA.

grown on the surface, or the sample has been contaminated, or it has not been oxidized, but reduced.

As it has been described in the introduction (Section 1.6), annealing in vacuum in the presence of oxygen may lead to the formation of incomplete layers of TiO_2 or even strands of Ti_2O_3. Such processes lead to the formation of structures on the surface and, as can be seen in the STM images in Fig. 6.18, no such phases can be detected on this sample. The images before and after annealing in oxygen (Fig. 6.18a and b, respectively), show almost identical morphology.

It has been reported for anatase that annealing in oxygen may lead to the formation of iron oxides on the surface of the sample. The SIMS profiles did not show any presence of iron, and, in fact, the surface was very clean, with concentrations of typical contaminations far below the amounts that can be observed on the as-received crystals (Fig. 6.14).

Therefore, the remaining possibility is that the surface was not oxidized during the annealing, but, due to low oxygen pressure, it became slightly reduced. This would explain why the work function decreased, since the surface is the location where the reduction occurs at the fastest rate, so accordingly, even a slight reduction of the crystal would introduce oxygen vacancies. Such a change would lead to the decrease of the work function from the value for the RT-oxidized surface to the value of the 50 CCs surface (which can be seen in Fig. 6.17c). Furthermore, a slight reduction would not significantly impact the conductivity of the RT-oxidized crystal. The pressure used is indeed lower than the pressures usually used in this kind of investigations, for example: 7×10^{-5} mbar to 7×10^{-6} mbar [214], 3×10^{-7} mbar [196], 3×10^{-7} mbar [123], which may explain why the crystal remained black and the surface did not oxidize. Nonetheless, the presence of isotopic oxygen during annealing was beneficial, because some mass exchange did occur, as demonstrated in the SIMS profiles (Fig. 6.12b), which allowed for the investigation into the depth of changes induced by the cleaning cycles.

Chapter 7

The effect of thermal annealing on $SrTiO_3$ crystals

Strontium titanate is a more complex oxide crystal than titanium dioxide, both in its composition and in its crystallographic structure. In this chapter, it will be shown that the reaction to simple annealing in UHV, in the case of $SrTiO_3$, is also more complex, with changes not only in the electronic properties of the surface, but also in its morphology. First, the surface was studied at relatively low temperatures, i.e. in a regime where reduction of $SrTiO_3$ was the main process. Subsequently, the crystal was investigated at temperatures which lead not only to reduction, but also to the decomposition of the crystal by incongruent effusion. Furthermore, the effect of the oxygen partial pressure on these processes was investigated by using oxygen getter substances. As the last step, the studied surfaces were exposed to oxygen and air at room temperature and the changes in electronic properties were measured.

7.1 Changes occurring on the surfaces of flat $SrTiO_3$ as a function of temperature with or without a getter

In the first stage, the $SrTiO_3$ crystals were annealed in UHV at increasing temperatures. The effect of the oxygen partial pressure in the vicinity of the crystal was controlled by annealing the monocrystal on either silicone (oxygen getter) or titanium dioxide (non-getter substance).

7.1.1 Experimental

The reduction of $SrTiO_3$ was systematically studied by annealing the crystal at the temperatures of 800 °C, 900 °C, 1000 °C and 1100 °C for one hour. Then the crystals were oxidized at room temperature by exposing them to approximately 150 L of oxygen. Two sets of experiments were conducted at the same temperatures, but with one key difference. In one set of experiments, the $SrTiO_3$ crystals were annealed on silicon, and in the other on TiO_2 (using the current-through-sample method described in Subsection 3.1.1). This way, the oxygen partial pressure was lower in one set of experiments than in the other. In the case of annealing without a getter, TiO_2 was chosen instead of $SrTiO_3$, because TiO_2 monocrystals do not break easily during annealing, in contrast to $SrTiO_3$ (due to its ductile-to-brittle-to-ductile transition described in Subsection 1.4.2). In my experience, for experiments with strontium titanate at temperatures above 1125 °C more than 75 % of monocrystals break during annealing or cooling, which makes this crystal difficult to work with.

7.1.2 Morphology and crystallography of the surfaces

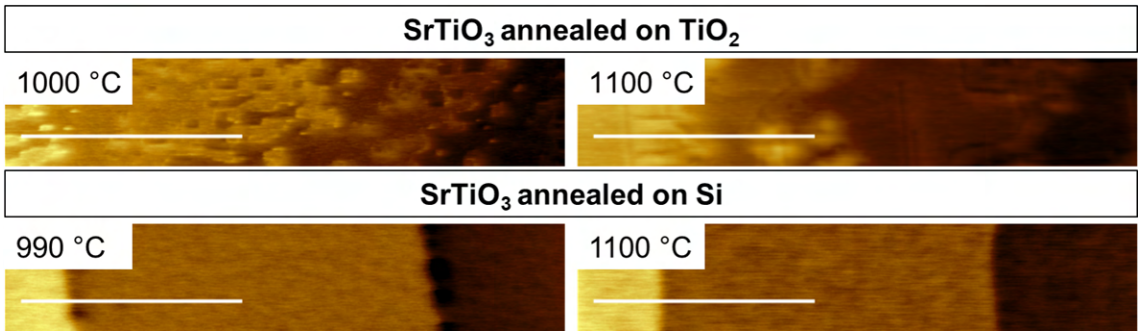

Figure 7.1: The KPFM morphology of $SrTiO_3$ surfaces annealed at 1000 °C and 1100 °C for crystals annealed in presence of a non-getter (TiO_2) and an oxygen getter material (Si). Scale bar represents 400 nm.

The investigation into the morphology of the $SrTiO_3$ surface annealed at temperatures up to 1100 °C showed that the surface remains flat regardless if the annealing is done in the presence of a getter material or not (see Fig. 7.1). The oxygen partial pressure, which is influenced by the getter, does, however, affect the character of the surface obtained. As can be seen in Fig. 7.1, annealing strontium titanate in the presence of silicon leads to large terraces of straight borders, while annealing it in the presence of titanium dioxide leads to smaller terraces of less compact edges. The experiments also show that the surface morphology does not significantly change with increasing temperatures.

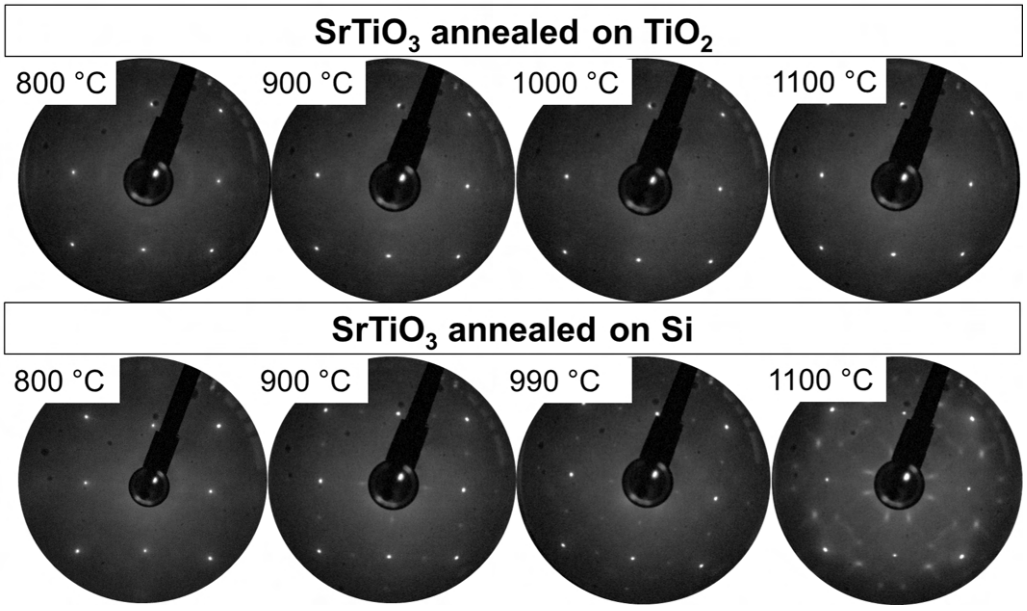

Figure 7.2: The changes in surface crystallography depending on the annealing temperature for $SrTiO_3$ annealed in the presence of a non-getter (TiO_2) and an oxygen getter material (Si). LEED patterns were made for 106 eV. The surfaces annealed on TiO_2 show a (1x1) reconstruction at all studied temperatures, while the reconstruction of the surface annealed on Si evolves from (1x1) through (2x2) and c(2x2) to ($\sqrt{13}$x$\sqrt{13}$ R33.7°).

The LEED investigations show that even though the morphology of the surfaces does not change drastically depending on the presence of getter material, the arrangement of the atoms of the surface does. During annealing on TiO_2, the surface reconstruction stays unchanged regardless of the temperature, remaining at (1x1). During the annealing on Si, the surface reconstruction evolves from (1x1) at 800 °C through (2x2) at 900 °C, c(2x2) at 990 °C to ($\sqrt{13}$x$\sqrt{13}$ R33.7°) at 1100 °C. The (2x2) reconstruction has been observed elsewhere at similar temperatures, i.e. 950 °C [215] and 1000 °C [216]. The c(2x2) reconstruction has only been observed once and at lower temperatures (800 °C) for thin films of $SrTiO_3$ [64]. The ($\sqrt{13}$x$\sqrt{13}$ R33.7°) has been seen at approximately the same temperatures, i.e. 1000 °C [85] and 1050 °C [217].

Unraveling the changes on the surface of $SrTiO_3$ and establishing a clear evolution of the reconstructions due to reduction is not an easy task, as more than 11 reconstructions of strontium titanate have been observed for various conditions [217]. Furthermore, there is no clear agreement on the phase diagram for these reconstructions [218]. It is, however, accepted that most of these reconstructions are due to a double layer of TiO_2 on the surface of $SrTiO_3$, with different concentrations of oxygen vacancies [217]. As proof, the reduction in UHV has been shown to increase the concentration of titanium on a $SrTiO_3$ surface [85]. It has also been demonstrated that, for $SrTiO_3$, at temperatures above 830 °C, impurities tend to disappear from the surface [219], so the changes observed cannot be due to impurities being incorporated into the surface, as it has been postulated [220]. All in all, it can be seen that a higher level of reduction of the surface leads to more and more complicated surface reconstructions, with even more complex reconstructions to follow, such as ($\sqrt{5}$x$\sqrt{5}$ R26.6°) [85].

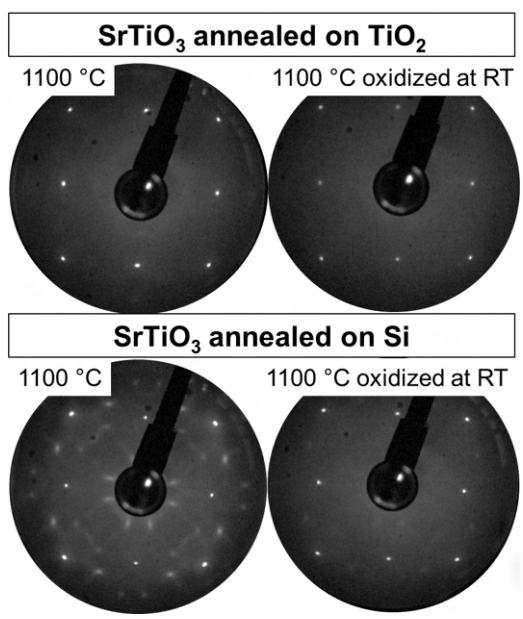

Figure 7.3: The LEED pattern change after exposure to oxygen in UHV at RT for a $SrTiO_3$ surface previously annealed on TiO_2, and a surface annealed on Si. The electron energy is equal to 106 eV.

In order to demonstrate that the changes in the surface reconstructions were due to

reduction, the crystals were exposed to oxygen, and the LEED measurements were performed again. The results can be seen in Fig. 7.3. For the $SrTiO_3$ sample annealed on TiO_2, the reconstruction remains as it was, i.e. (1x1). For the $SrTiO_3$ sample annealed on Si, there was a significant change in the diffraction pattern, i.e. the spots of the ($\sqrt{13}$x$\sqrt{13}$ R33.7°) almost completely disappear. This implies that the oxygen-deficient TiO_2 termination, which is most likely the cause of the observed reconstructions, is healed, which almost restores the stoichiometric reconstruction of (1x1).

7.1.3 Work function of the surfaces

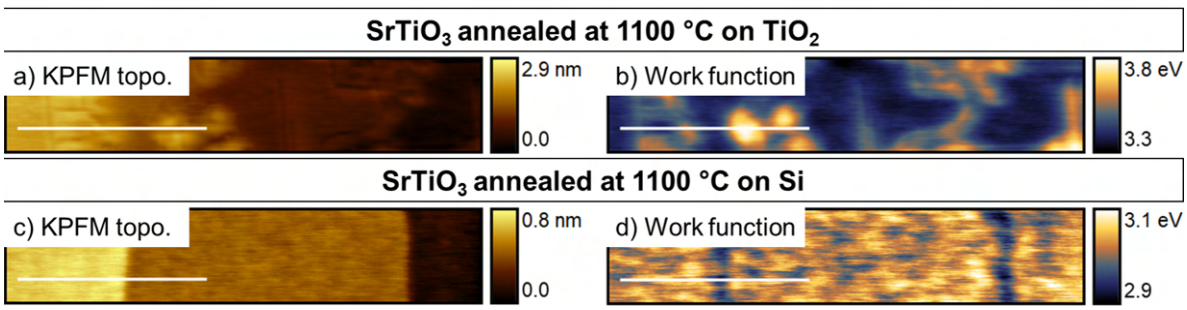

Figure 7.4: The KPFM morphology and work function maps for surfaces annealed at 1100 °C in the presence of a non-getter material and a getter material. Scale bar: 400 nm.

The work function has been systematically studied as a function of the annealing temperature for both crystals annealed in the presence of oxygen getter and in its absence. The values were derived from maps such as the maps presented in Fig. 7.4, where the terrace edges were masked, as their work function values differed due to the formation of dipoles. The work function is different on the step edges. Furthermore, it behaves differently for the sample annealed on TiO_2 and Si. In case of the sample annealed on non-getter material, the terrace edges show higher work function values than terraces, while for the sample annealed on a getter material, the opposite can be observed. Such inversion can be explained by assuming that for the less-reduced sample ($SrTiO_3$ on TiO_2), the step edges are composed of oxygen, while for the more-reduced sample ($SrTiO_3$ on Si), the step edges are made up of titanium, as such inversion in contrast for these cases has been calculated using DFT [221].

The changes in the values of the work function for all the cases investigated in this section can be seen in Fig. 7.5. The work function of the sample annealed on titanium dioxide remains the same, regardless of the temperature, and then slightly increases after exposure to oxygen at RT (from 3.76(3) eV to 3.91(3) eV). The sample annealed on a getter material started out at approximately the same value of the work function, but then the increasing temperature led to the drop in work function from 3.58(3) eV to approximately 3.1(1) eV for all other annealing temperatures. The following oxidation led to a dramatic increase in the work function from 3.30(2) eV to 3.91(3) eV.

The starting value of the work function for 800 °C is approximately the same as the

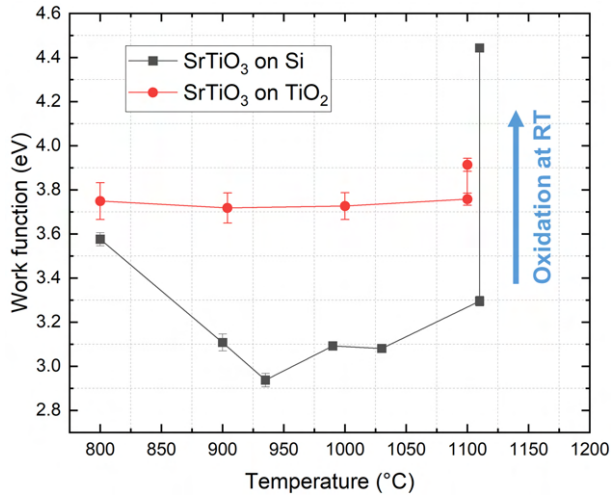

Figure 7.5: The relationship between the work function and the temperature for $SrTiO_3$ which was annealed on an oxygen-getter material Si and a non-getter material TiO_2, and subsequently oxidized at room temperature in situ.

value obtained by Wrana et al. (2019) [85] for the same temperature, i.e. 3.75 eV, and can be considered as the slightly reduced (1x1) TiO_2 terminated $SrTiO_3$ surface. The value for the stoichiometric TiO_2 terminated $SrTiO_3$ surface is much higher, at 4.2 eV [222] or 4.3 eV [223], but this is to be expected, since oxygen vacancies on this type of termination, which are present on the slightly reduced surface, lead to the lowering of the value of the work function [221]. The subsequent drop in the work function values for the sample annealed in more reducing conditions could be explained by the increase in oxygen vacancies, as DFT calculations show that introducing 25 % of oxygen vacancies leads to a drop of 1.5 eV [221]. Furthermore, highly reduced $SrTiO_3$ (annealed in the presence of a getter at 1150 °C) exhibits the work function of 3.12(18) eV [224], which is equal to the values obtained in the present experiments. The experimental data appears to be in agreement that oxygen-deficient reconstructions lower the work function value, however, DFT calculations demonstrate that such reconstructions should increase the work function by 1 eV to 2 eV [221], which was not observed in this series of experiments.

7.2 Growth of nanowires on $SrTiO_3$ during annealing in UHV

In this section, an additional process is introduced into the investigation, i.e. incongruent sublimation at extremely low oxygen partial pressures, which was described in Section 1.5.2. At these high temperatures, the samples are not only reduced, but are also decomposing, which leads to the formation of suboxide structures, such as the formation of titanium monoxide nanowires on the surface of strontium titanate.

7.2.1 Experimental

Two different ways of annealing were used in order to study the incongruent decomposition of strontium titanate. For in-situ KPFM/LEED investigations, the $SrTiO_3$ crystals were annealed on silicon wafers using the current-through-sample method of heating. For investigations into the effect of getter material, i.e. titanium and silicon, the electron beam method was used, because it was the only method which allowed for the usage of titanium foil as a getter. Other methods, such as annealing in a crucible, would not allow for sufficiently high temperatures of the getter as compared to the studied crystal.

In case of the investigation of the growth of structures in the presence of silicon one crystal was annealed for one hour. Different parts of the crystal had different temperatures ranging from 1100 °C to 1190 °C, which allowed for the systematic study of the growth mechanism while maintaining the same experimental conditions. The temperature of the getter was close to melting as parts of the silicon crystal melted. The sample was later investigated using SIMS to establish how the chemical compositions differed between various parts of the sample.

During the investigation into the growth of structures in the presence of a titanium getter, a strontium titanate crystal was annealed in the presence of titanium foil for one hour. The crystal had three areas of different temperature: 1050 °C, 1100 °C and 1150 °C. The temperature of the getter was above 1350 °C, which is the maximum temperature that can be measured using the pyrometer.

7.2.2 Crystallographic and chemical composition of the nanowires

The chemical and crystallographic composition of the nanowires was determined using a combination of techniques, i.e. EDX, EBSD, TEM and EELS. This wide range of methods enabled a thorough analysis of the nanowires.

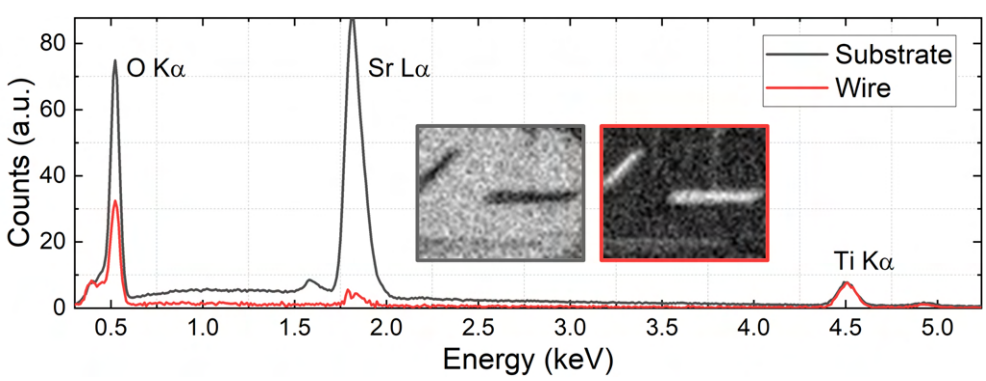

Figure 7.6: The EDX spectra of the substrate and nanowire (separated using machine-learning algorithms [168]) demonstrating that the structures in the insert were composed of titanium and oxygen, while the substrate also contains strontium. Electron energy of 7.5 keV was used, as it was the lowest energy that still allowed for a quantitative analysis of the spectra, while maintaining a relatively low penetration depth.

Incongruent sublimation of $SrTiO_3$ annealed at 1150 °C, leads to a sample covered with

nanowires that follow the crystallographic directions of the $SrTiO_3$ substrate (see. Fig. 7.7c). Performing an EDX analysis assisted by machine-learning techniques (as described in [168]), made it possible to assign the X-ray fluorescence spectra to the substrate and the nanostructures (see. Fig. 7.6). It can be clearly seen that the substrate is composed of strontium, titanium and oxygen, as it is the $SrTiO_3$ monocrystal. The nanostructures, on the other hand, do not contain strontium, and are only composed of titanium and oxygen. The small peak of Sr Lα visible for the structures is there due to the fact that X-rays come from a large depth that also includes the substrate below the nanowires. This was the preliminary result which pointed to the fact that the structures were titanium suboxides. A more powerful technique was necessary to obtain exact stoichiometry.

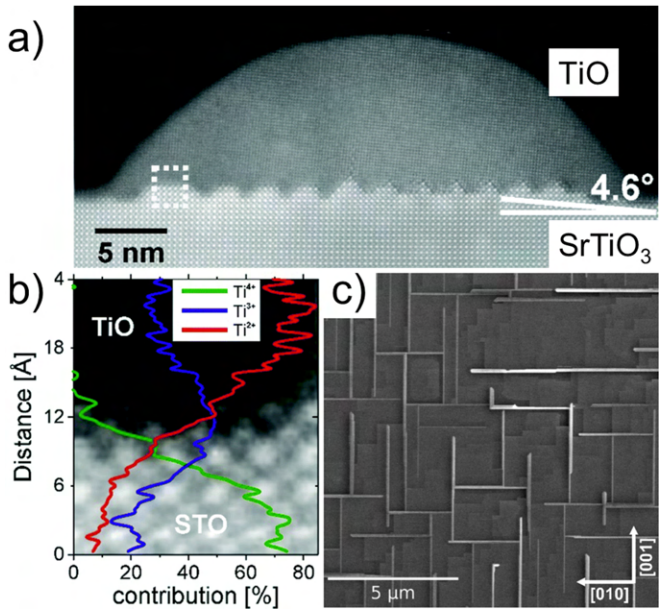

Figure 7.7: a) A HAADF STEM image of the nanowire on the $SrTiO_3$ substrate and b) the EELS spectrum superimposed on the area dotted out in a), demonstrating that the core of the nanowire was composed of TiO [99]. c) SEM image displaying that the nanowires form a grid following the crystallographic directions of $SrTiO_3$ [99].

Using HAADF STEM, a cross-section of the structure was imaged (see. Fig. 7.7a). As can be seen both the nanowire and the substrate show long-range ordering, with an atomically sharp, zig-zag-shaped interface between them. The nanowire is tilted at an angle of 4.6°, which is most likely a form of strain relaxation due to a mismatch between the lattice of $SrTiO_3$ and the nanowire. The EELS analysis (Fig. 7.7b) shows that the structure is composed mostly of titanium at the second oxidation state, in stark contrast to the substrate, which mostly has titanium at the fourth oxidation state. The nanowire has the crystallographic structure of rock salt with a lattice parameter of 4.18 Å. These results are in agreement with the published diffraction measurements for titanium monoxide (PDF: 89-3660).

The surface of the nanowires was investigated using both EBSD and HAADF STEM. Diffraction patterns were obtained from the nanowires (Fig. 7.8a) and were compared with simulated patterns for various titanium suboxide phases. The pattern which fit the most (a

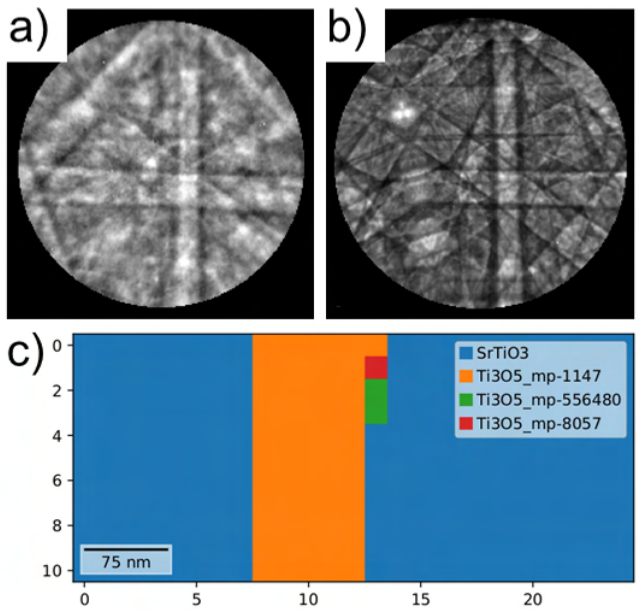

Figure 7.8: a) The EBSD diffraction pattern from the surface of the nanowire, b) the simulated diffraction pattern for Ti_3O_5, c) the calculated EBSD phase map (based on the maximal values of correlation coefficients) showing that the surface of the nanowire is composed of Ti_3O_5 and that the nanostructure grows on $SrTiO_3$.

correlation coefficient of 0.86), depicted in Fig. 7.8b), was the one for the monoclinic Ti_3O_5 phase. The correlation map in Fig. 7.8c) shows that the nanowire's surface is composed of this phase, while the substrate is still composed of $SrTiO_3$. Decomposition of the STEM EELS data (Fig. 7.9), demonstrates that the position of the edges of the Ti L3 peaks differs between the bulk and the surface of the nanowire. The results of the used methods indicate that the composition of the nanostructure is complex, i.e. its surface is Ti_3O_5 while the core of the nanowire is TiO.

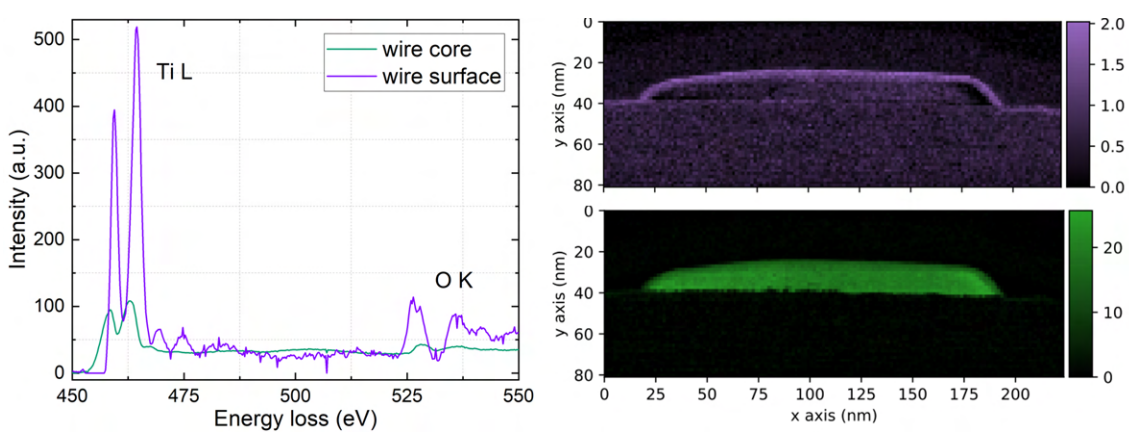

Figure 7.9: EELS spectra from the marked regions showing that the core and surface of the nanowires are composed of different titanium oxides.

7.2.3 The relationship between annealing temperature and morphology of nanowire-covered $SrTiO_3$

The chemical composition and morphology of the suboxides forming as a result of incongruent effusion can be controlled by changing the annealing temperature. Furthermore, more than one type of oxygen getter substance exists and depending on the getter substance used different morphologies can be obtained at the same temperatures.

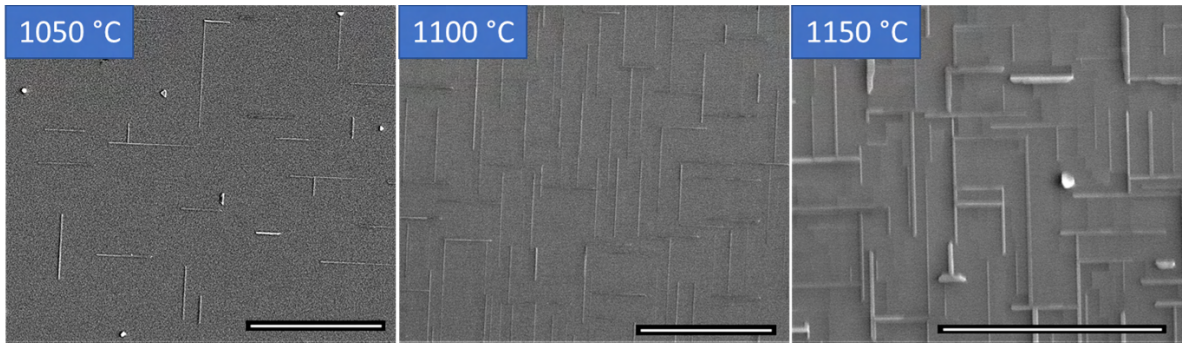

Figure 7.10: The morphology of the $SrTiO_3$ surface after annealing at increasing temperatures in UHV in the presence of a titanium oxygen getter. The scale bar corresponds to 5 µm.

When annealing $SrTiO_3$ in the vicinity of titanium foil nanowires begin to grow already at the temperature of 1050 °C, while increasing the temperature further leads to higher densities of structures, as can be seen in Fig. 7.10. The structures follow crystallographic directions and they have wire-like shapes. Investigations at higher temperatures were not possible, due to the fact that in higher temperature conditions, the titanium foil melted down and acted as a very efficient heat radiator, which made increasing the temperature of the $SrTiO_3$ monocrystal difficult.

The later stages of the suboxide layer evolution were investigated using silicon as an oxygen getter. As demonstrated in Fig. 7.11a), for the same temperature, i.e. 1100 °C, as in Fig. 7.10, the surface is not covered by nanowires, but with islands, which seem to be the first stage of the nanowire growth. With increasing temperature, nanowires appear at 1140 °C. They follow the crystallographic directions of $SrTiO_3$ and have sharp line-like edges. Increasing the temperature to 1170 °C leads to the nanowires growing in size and connecting with each other. Furthermore, their appearance now resembles melted-down nanowires. When the crystal reaches 1190 °C, it is difficult to distinguish individual structures, as most of them are tightly connected and are large in size. A porous structure begins to form, with the $SrTiO_3$ substrate being visible only in some places.

It is worth mentioning that experiments in crucibles and quartz tube were also performed in order to find systematically the effect of the getter temperature on the growth of structures. What was discovered was the fact that for the growth of the suboxide structures to occur, the oxygen getter must have a much higher temperature than the strontium titanate, which is impossible to accomplish with these annealing methods.

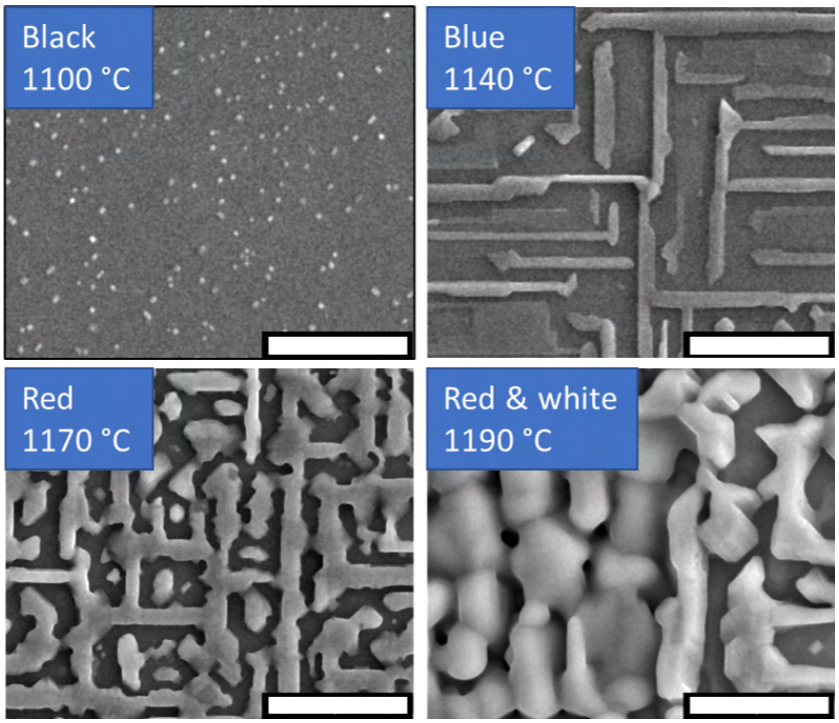

Figure 7.11: The evolution of morphology on the surface of $SrTiO_3$ as a function of temperature. The white scale bar corresponds to 2 µm. The colors in the description are indicative of the color of the crystal at the given location (see Fig. 7.12a). Si getter was used.

7.2.4 Chemical composition of the suboxide layer grown on $SrTiO_3$

These later stages of decomposition of strontium titanate lead to the formation of a layer that does not appear as crystalline and organized as the nanowires. These structures, present on the red and white region (Fig. 7.11), seem to form a thick, porous layer, which no longer strictly follows the substrate directions. SIMS measurements were undertaken, in order to establish how much the composition of this layer differs from the substrate and approximately how thick the layer is.

The monocrystal annealed at high temperatures in the presence of a silicon getter had a multitude of colors visible using the naked eye. These colors can be seen in the optical microscope image (Fig. 7.12a). Both SEM and SIMS measurements were performed on each section of the sample to correlate the colors to both morphology and chemical composition. The chemical composition was measured using SIMS profiling and, as can be seen in Fig. 7.12b), it differs significantly from region to region. As expected, the higher the temperature of annealing, the less strontium is present on the surface, as more and more of this element leaves the crystal due to incongruent effusion. Furthermore, the profiles show that the depth of the sub-oxide layer is profound and increase quickly with temperature. Stoichiometry was reached only after approximately 500 nm for the red part of the crystal, which was annealed at 1170 °C, while the blue part of the crystal annealed at the temperature lower only by 30 °C, stoichiometry was reached only after approximately 100 nm. The values of the $CsTi^+$ to $CsSr^+$ ratio also increase at higher annealing temperatures. The exact stoichiometry of the layer and

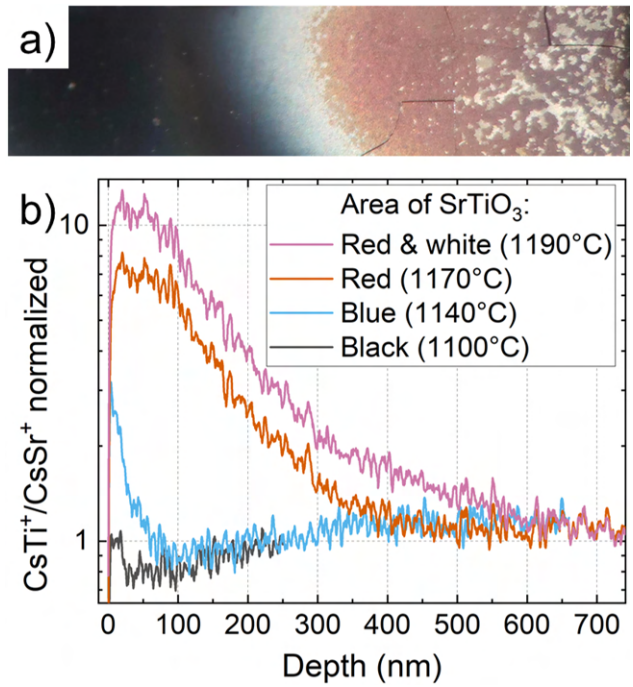

Figure 7.12: a) Optical microscope image of the crystal (scale approximately 1 mm by 6 mm). b) SIMS profiles of the different regions of the crystal. The profiles were normalized to a profile measured for an as-received $SrTiO_3$ crystal.

its chemical evolution with increasing temperature cannot be easily deduced from the profiles, as the rich morphology of the surface affects the measured, signal since the measured ions concurrently come to the detector from various depths of the porous sample.

7.3 Changes in electronic properties of the nanowire-covered $SrTiO_3$ surface after exposure to oxygen or air at RT

The obtained titanium monoxide nanowires, which differed so much from the strontium titanate substrate, were investigated in the context of their electronic properties. The effect of oxygen and air exposure on the properties of this system was also studied.

7.3.1 Experimental

The nanowire-covered substrate was prepared by annealing $SrTiO_3$ at 1050 °C for one hour in the presence of a silicon getter in UHV, using the current-through-sample method. Two such crystals were prepared, one was used to study the effects of oxygen and the other the impact of air exposure on the electronic properties.

The effect of oxygen exposure was initially investigated by imaging the surface, and then by exposing it to 450 L of oxygen in situ.

The effect of air exposure was studied by first measuring the properties of the sample and then exposing it to air in the load-lock of the UHV system. Subsequently, the properties

were measured again. In order to determine the impact of easily desorbing adsorbates, such as nitrogen molecules and water, the monocrystal was then annealed at 230 °C for one hour and subsequently studied again using KPFM.

7.3.2 The electronic properties of the nanowires on $SrTiO_3$ substrate

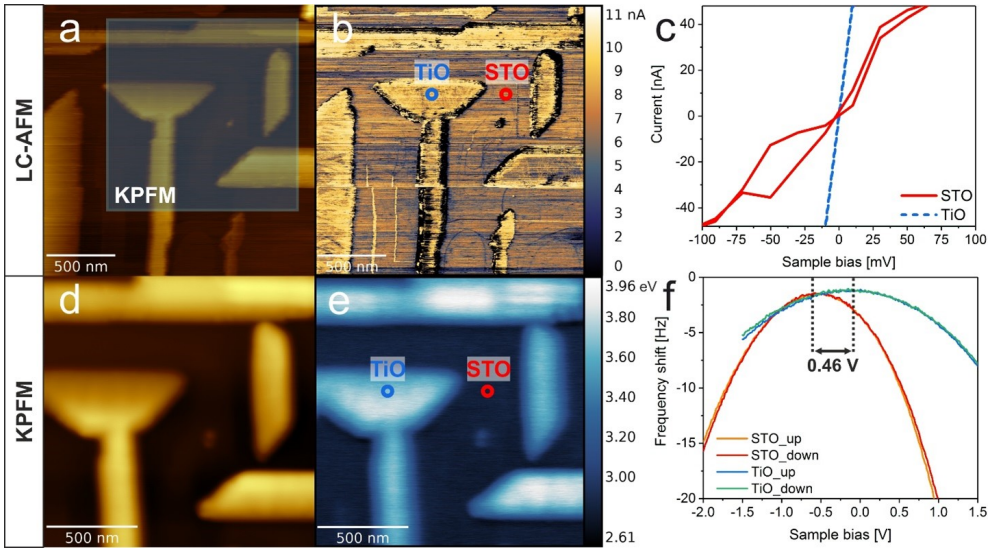

Figure 7.13: The electronic properties of the nanowires on $SrTiO_3$ as seen using LC-AFM a) topography and b) current maps) and KPFM d) topography and e) work function. The KPFM map was collected from the region marked in a). c) I-V curves measured on the spots depicted in b), and f) Kelvin parabolas from points in e). These results were published in [85].

It comes as no surprise that the electronic properties of the nanowires and the $SrTiO_3$ substrate differ. As demonstrated in Fig. 7.13b), the nanowires exhibit a higher conductance than the substrate. The I-V curves (Fig. 7.13c) measured on top of the nanowire and on the substrate show that the nanowires are more metallic-like than the reduced $SrTiO_3$, which by itself is also highly conductive. The higher conductance in the nanowires is most likely due to two factors. First of all, the titanium ions in the nanostructures are in the form of Ti^{2+}, which provides d-band electrons responsible for metallic conductivity [224]. Second of all, as it was described in [99], these nanowires form on top of a network of highly conductive dislocations. The d-band electrons in $SrTiO_3$ concentration are much lower, leading to lower conductance.

The work function of these structures also differs by 0.46 eV, as shown in the Kelvin parabolas (Fig. 7.13c). The value of the work function for the substrate is equal to 3.1(2) eV, and of the nanowire 3.3(3) eV. The value for nanowires is, within uncertainties, equal to the value published for TiO nanoparticles (size 14 nm), i.e. 3.01 eV[225]. It was assumed at this point that the nanoparticles studied by Chen et al. (2014) [225] were also covered with a layer of Ti_3O_5, just as the nanowires studied here. The work function of the $SrTiO_3$ substrate is much lower than in the case of stoichiometric strontium titanate (3.1(2) eV compared to 4.2 eV to 4.3 eV[222],[223]), which points to a high level of reduction of the crystal. Comparing this value to the work functions of systematically reduced $SrTiO_3$ (as depicted in Fig. 7.5),

it can be sees that the work function of $SrTiO_3$ reduced on silicon oscillates in the range of values from 2.8 eV to 3.3 eV. This leveling off at approximately 3.0(2) eV may indicate that the surface is reduced to a final concentration of oxygen vacancies, and further reduction occurs at the bulk, and therefore does not affect the value of the work function. The changes of the work function due to incongruent sublimation lead to the formation of structures at the expense of the surface, thus the effusion of strontium should, most likely, not affect the work function of the substrate in-between the nanowires.

As can be seen in Fig. 7.13e), the edges of nanowires have a slightly lower work function, with the value of the work function on the structures varying by up to 300 meV. Such variations are most likely due to the fact that at the different sides of the structure, diverse crystal surfaces are present. The work function differences between various surfaces of the same crystal have been observed in many cases, such as for TiO_2 [226], $SrTiO_3$ [227] and even on single grains of $CuGaSe_2$ [228]. The exact surfaces exposed are difficult to determine, as no high resolution STM images on the faces have been collected.

7.3.3 The effect of oxygen exposure at RT on the electronic properties of the nanowires on the $SrTiO_3$ substrate

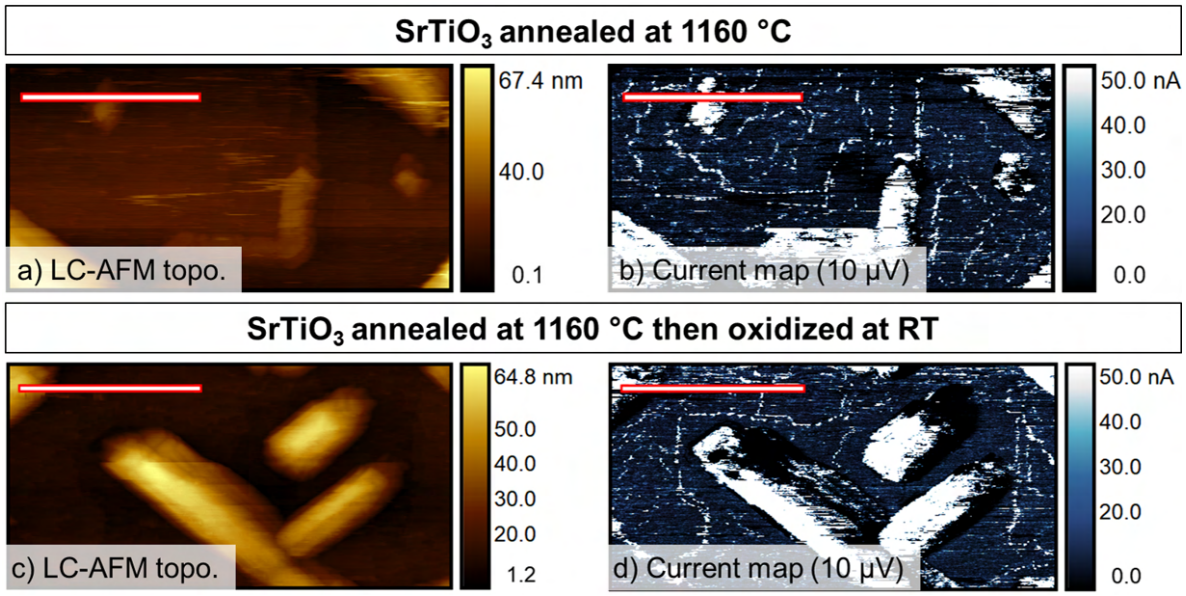

Figure 7.14: The LC-AFM topography and current maps of $SrTiO_3$ before and after oxidation at room temperature. The scale bar represents 400 nm.

The conductance of the nanowires does not change after exposure to oxygen, as can be seen in Fig. 7.14. The nanowires are so conductive that even an extremely low bias is enough to reach the maximal current measurable by the microscope. In the case of highly reduced $SrTiO_3$ substrate, it had been studied for higher biases by Wrana et al. (2018) [85] and demonstrated that exposure to 100 L is enough to switch the conductance of such a surface from high to low

conductivity. The fact that the nanowires remain conductive suggests that they are formed on highly conductive defects, such as dislocations, which provide a low-resistance pathway to the current flow.

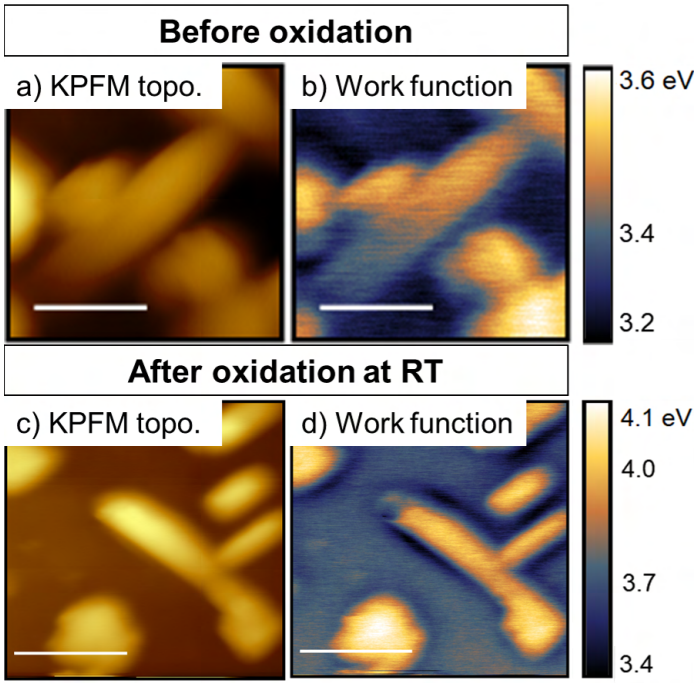

Figure 7.15: The KPFM topography and work function maps before a), b) and after c), d) oxidation at room temperature. The scale bar represents 400 nm.

The changes in the work function of the nanowire-covered $SrTiO_3$ can be seen in Fig. 7.15. The overall character of the surface did not change, as the nanowires still have a higher work function than the substrate. However, all of the values are shifted upwards. As depicted in the histograms in Fig. 7.16, oxidation at RT increases the work function of the system by approximately 0.5 eV. For $SrTiO_3$, an increase in the work function due to oxidation at RT has been shown for $SrTiO_3$ reduced at 1110 °C (increase by 0.6 eV - see Fig. 7.5), and $SrTiO_3$ reduced at 900 °C (increase by 0.55 eV) [85]. As described in Subsection 7.1.3, this change in the electronic property is due to the filling of oxygen vacancies which were present on the reduced strontium titanate. The change in the work function of the nanowires is not as easily explained. The nanowires are a complex system with a Ti_3O_5 layer covering the TiO core, and the subsequent exposure to oxygen could either lead to the healing of possible oxygen vacancies, or a further phase change of the surface layer to another titanium oxide. The fact that a similar change in values is observed suggests that a similar mechanism is taking place, i.e. the filling of vacancies, however without theoretical modeling, the answer cannot be established with confidence.

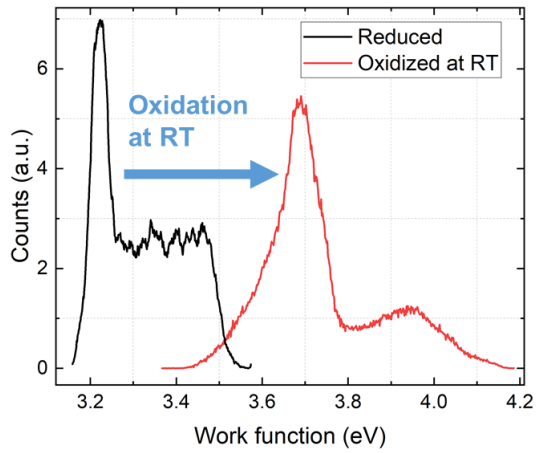

Figure 7.16: The histograms of the work function based on the maps from Fig. 7.15, showing the changes in this property after oxidation at room temperature.

7.3.4 The effect of air exposure at RT on the electronic properties of the nanowires on the $SrTiO_3$ substrate

Regardless of the system studied, most devices work at normal pressures and in air, and in order to bring the results closer to the application side, the effect of exposure to such conditions on the properties of the nanowire-covered $SrTiO_3$ system was also studied.

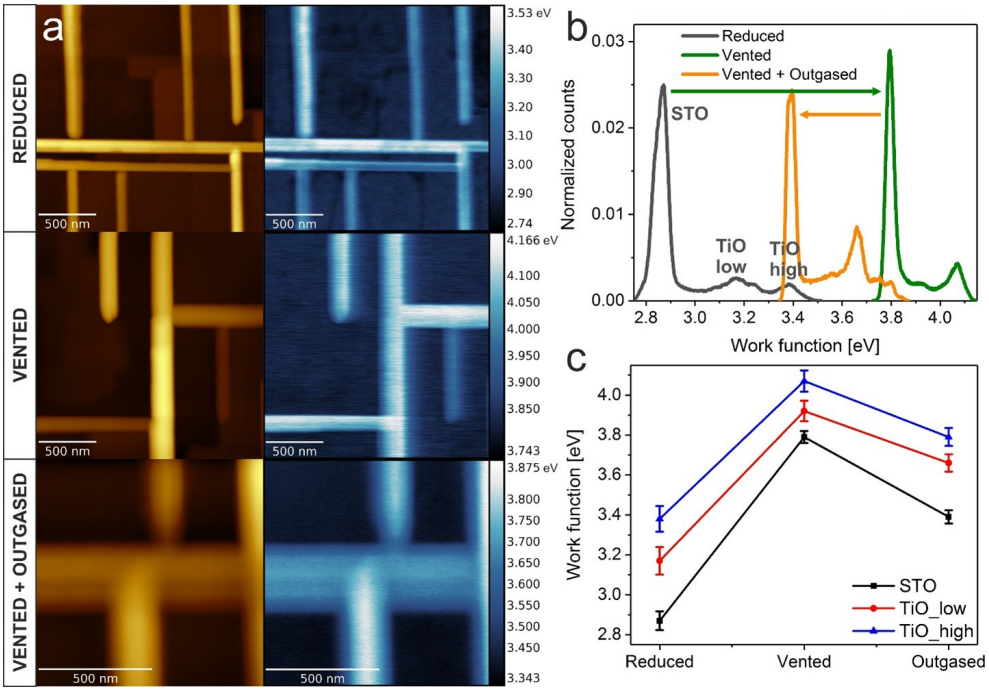

Figure 7.17: The effect of air exposure and the subsequent annealing at 230 °C on the work function of the nanowires and $SrTiO_3$ substrate as depicted by a) KPFM maps, b) work function histograms, and c) a graph. These results were published in [85].

A reduced sample was exposed to air at atmospheric pressure by venting it in the load-lock of the UHV system, and, as can be seen in Fig. 7.17a), no new structures appeared

on the surface. There were, however, changes in the electronic properties of the system, as demonstrated in the histogram in Fig. 7.17b). The work function of the whole system increased. The work function value of the nanowires increased from 3.3(3) eV to 3.9(2) eV, and for the substrate it increased from 3.1(2) eV to 3.84(8) eV. These increases may be due to the oxygen in the air, water or other adsorbates (such as organic adsorbates). Oxygen most likely plays the main role, as the increase in value is almost exactly the same as the increase discussed in the previous section, where samples were exposed to pure oxygen. To test this hypothesis, the sample was annealed at 230 °C in order to remove adsorbed water. In all cases, the removal of water from the surface led to a drop in the work function (by 0.17(28) eV for the nanowires and 0.43(19) eV for $SrTiO_3$). This demonstrated that the water which forms a dipole layer on the surface, increases the overall work function of these oxides, which was also reported for TiO_2 [229], [230]. The similarity of the work function values in the sample exposed to air and then annealed at 230 °C and the sample that was only exposed to oxygen, indicates that the effect of organic adsorbates on the work function in these short time frames is not that significant, and the influence of oxygen and water is the most important.

Chapter 8

Changes induced by annealing in oxygen on the nanowire-covered $SrTiO_3$ surface

The nanowire-covered $SrTiO_3$ is a unique system with two different crystallographic, well-defined phases coexisting on the surface. Furthermore, each of the phases has their own set of electronic properties. In this chapter the system will be studied in the context of very harsh oxidizing conditions, i.e. annealing in oxygen. As it will be shown, this will lead to changes not only in properties, such as was the case in RT-oxidized sample, but also to dramatic changes in composition of both $SrTiO_3$ and TiO. The changes in properties will be investigated using SPM techniques, while the structural and chemical changes will be studied using HAADF-TEM.

8.1 Growth of structures on the nanowire-covered $SrTiO_3$ due to oxidation

8.1.1 Experimental

The oxidation was performed in two different ways in order to study the early and late stages of the oxidation.

The initial stages of oxidation due to annealing in oxygen were performed in UHV by annealing the nanowire-covered monocrystal (obtained by annealing $SrTiO_3$ at 1160 °C for one hour in the presence of silicon) on a current-through-sample holder for one hour at 800 °C, at the oxygen pressure of 5×10^{-8} mbar. The surface crystallography was investigated using LEED, while changes in morphology and electronic properties were studied using KPFM and LC-AFM. STM was used as a supportive technique.

The later stages of oxidation were studied by annealing the crystal in a quartz tube at 800 °C at relatively high oxygen pressure of 2×10^{-2} mbar. The nanowire-covered sample was obtained by annealing $SrTiO_3$ at 1150 °C for 23 min in the presence of titanium foil on an electron-beam holder. The changes due to oxidation were studied using AFM and SEM. Subsequently, a lamella was made and a thorough HAADF-TEM measurement was performed. The chemical composition of the crystal was studied using EDX.

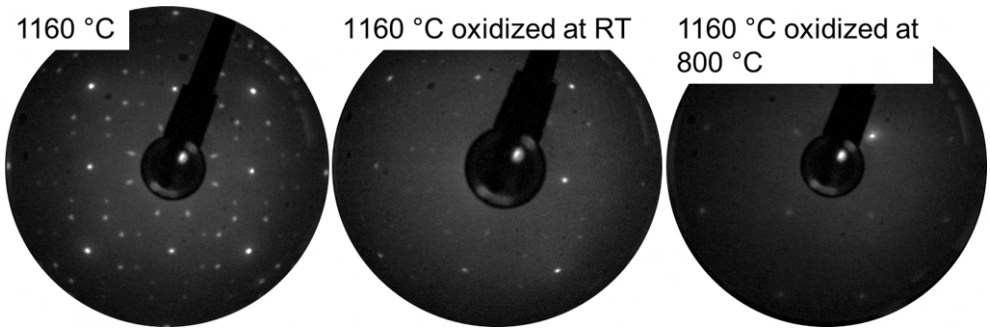

Figure 8.1: The LEED patterns for $SrTiO_3$ surfaces: a) annealed in UHV in 1160 °C, b) then oxidized at RT, c) then annealed at 800 °C in oxygen. The LEED pattern evolves from ($\sqrt{5}$x$\sqrt{5}$ R26.6°) for the reduced sample, through ($\sqrt{5}$x$\sqrt{5}$ R26.6°) with dominating (1x1) spots for the RT oxidized sample, to a very weak (1x1) reconstruction for the surface oxidized at 800 °C at the pressure of 5×10^{-8} mbar. All LEED patterns were collected for the electron energy of 106 eV.

8.1.2 Changes in morphology

Oxidation at 800 °C was first investigated in the context of surface crystallography. The LEED patterns change due to oxidation (Fig. 8.1). The reduced surface displays the clear ($\sqrt{5}$x$\sqrt{5}$ R26.6°), while oxidation at RT leads to the weakening of the spots of this reconstruction, with (1x1) showing the greatest intensity. Oxidation at 800 °C causes the surface to develop the basic (1x1) reconstruction with spots of weak signal-to-noise ratio.

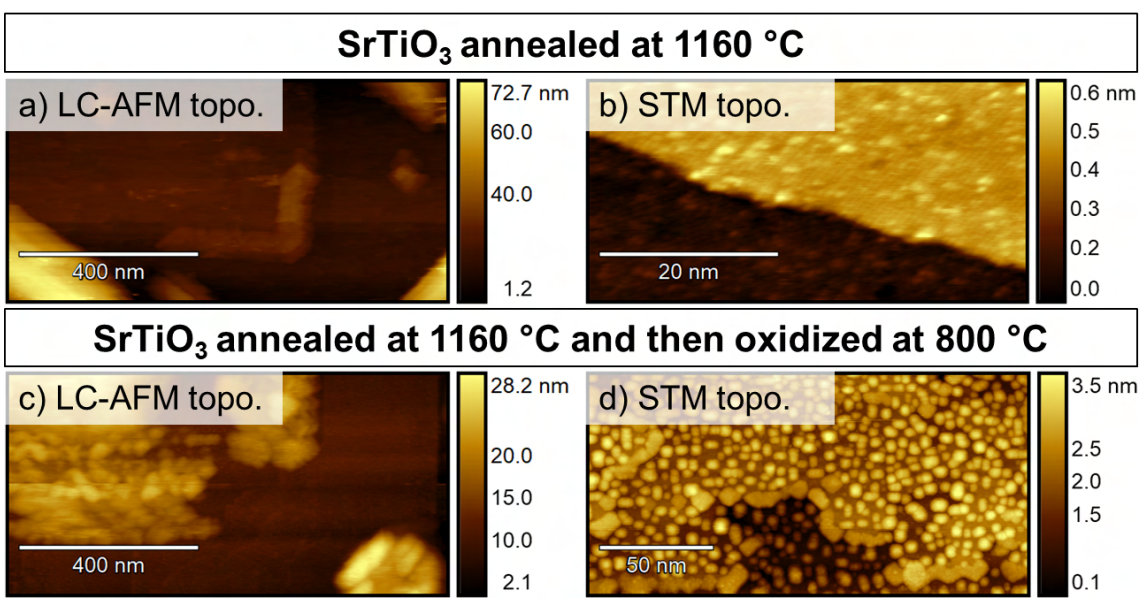

Figure 8.2: The LC-AFM and STM topography maps of $SrTiO_3$ before a), b) and after oxidation at 800 °C at the oxygen pressure of 5×10^{-8} mbar c), d). The STM images were collected for 1.1 V, 10 pA and 1.3 V, 10 pA in case of image b) and d) respectively.

As it was described in Subsection 7.1.2, the weakening of the reconstruction ($\sqrt{5}$x$\sqrt{5}$ R26.6°) implies that the oxygen deficiency is partially healed during exposure to oxygen at RT. When the surface is oxidized at 800 °C, the ($\sqrt{5}$x$\sqrt{5}$ R26.6°) reconstruction is not present,

and only the (1x1) reconstruction remains. However, the signal-to-noise ratio is very weak. In general, diffraction patterns with low signal-to-noise ratio may indicate that the surface is significantly defected, is covered by adsorbates, or that the domain sizes are very small.

The answer to the question of low-quality LEED patterns can be seen in the topography images taken before and after oxidation at 800 °C (Fig. 8.2). Oxidation at 800 °C leads to the formation of nanostructures on the surface. Before oxidation, the surface was nanowire-covered, but after oxidation, islands of a diameter of approximately 6 nm grew between and on the nanowires. The islands did not follow any crystallographic directions of the surface. The terraces appeared to be unchanged and most likely were the source of the (1x1) reconstruction that can be seen in the LEED pattern (Fig. 8.1). The islands which grew on the surface were too small to create their own diffraction pattern, even if they were crystalline. The low signal-to-noise ratio could be caused by the fact that the nanostructures mask most of the terraces, only leaving small parts of the surface, which may be the source of the (1x1) reconstruction.

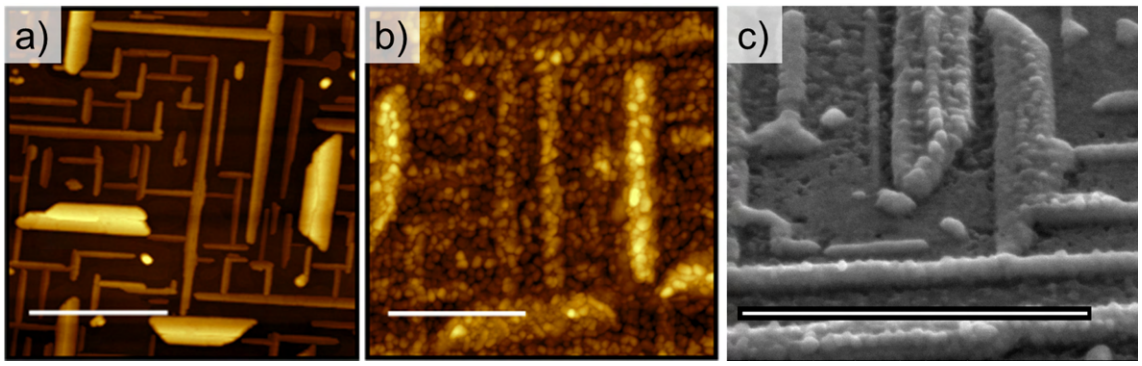

Figure 8.3: The AFM morphology a) before and b) after oxidation at 2×10^{-2} mbar of oxygen at 800 °C. c) SEM image of the oxidized surface collected at an angle of 50°. The scale bar corresponds to 1 µm.

The latter stages of oxidation were studied by annealing at the same temperature, but at higher oxygen pressures (2×10^{-2} mbar instead of 5×10^{-8} mbar). Such conditions led to even greater changes on the surface, as can be seen in Fig. 8.3. The surface was thoroughly covered by structures (Fig. 8.3b), and as can be seen in the SEM image (Fig. 8.3c), these structures protrude from a film of a new substance which grew on the surface. A comparison of the results for both oxygen partial pressures reveals that increasing the oxygen partial pressure leads to the change of the type of structures that cover the surface, from separate islands to a film of new material. In both cases, new objects form on both $SrTiO_3$ as well as the nanowires.

8.1.3 Changes in the structure and composition of the nanostructures

In order to establish what is the nature of the structures that grew during oxidation, i.e. their chemical composition and crystallographic structure, many analytical methods were employed. At first, simple SEM-EDX measurements were attempted, but a set of difficulties was encountered. First of all, the structures were too small for EDX mapping. Second of all, when the mapping of the film was attempted, the high roughness of the surface resulted in oxygen-to-titanium ratios that were high enough to be doubtful. The spectra for the nanowires

showed only titanium and oxygen, but their ratio indicated a titanium oxide of an oxidation state higher than 2 (even up to 5). This is due to the fact that the ZAF correction (atomic, absorption and fluorescence effect corrections) used during the quantification of the EDX signal assumes a flat surface and a uniform distribution of the elements in the investigated region, which was not the case. Moreover, the crystallography of the structures could not be studied using EBSD, as the lack of diffraction spots could be either due to an amorphous surface or because of the high roughness of the surface. Accordingly, it was necessary to use to HAADF-TEM in order to determine conclusively what grew on the surface.

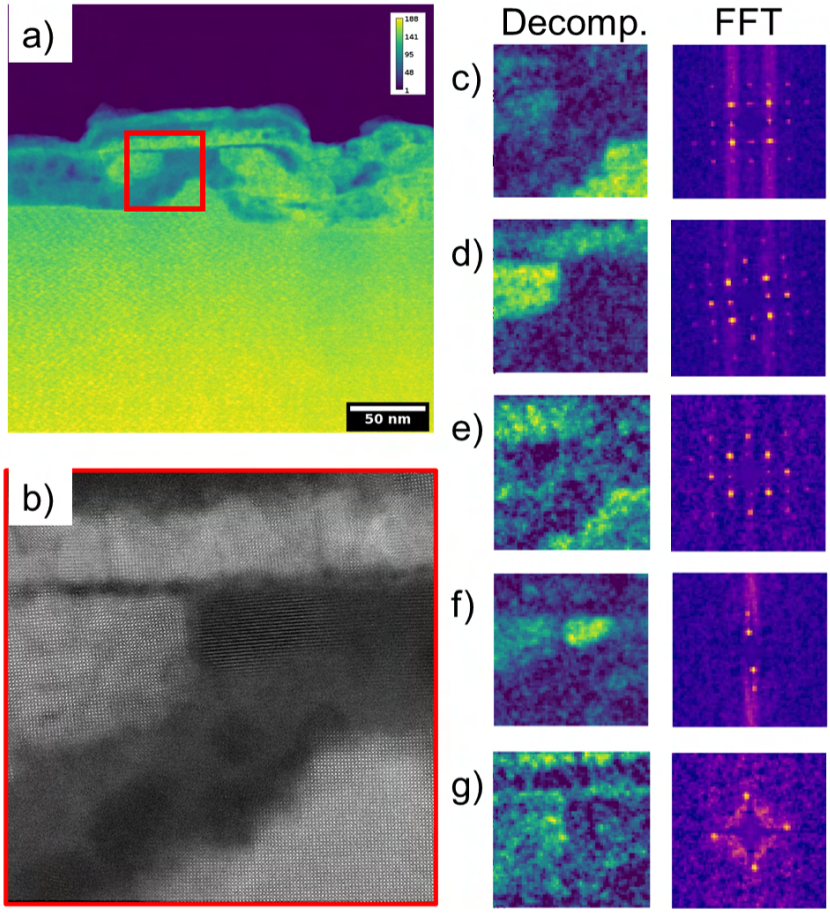

Figure 8.4: a) A colored HAADF-TEM image, where the red rectangle corresponds to the insert in b) from which FFT was obtained. c), d), e), f), g) show the phases identified using decomposition and their FFT patterns.

The HAADF-TEM image in Fig. 8.4a) indicates that significant changes occurred in the crystal, both in its composition and its structure, and that their scope was up to 100 nm in depth. Since this technique is extremely sensitive to changes in the atomic number, with greater intensity being associated with a greater atomic number, it can be seen that the newly formed layer is of lower density than $SrTiO_3$. Furthermore, the layer is not uniform with the existing regions of higher and lower intensity. An examination of the the magnified region in Fig. 8.4b) reveals, that some regions have a highly crystalline character, with noticeable atoms

and atomic planes, while other regions do not, as they only show a uniform color.

The crystalline structure of the regions was investigated using FFT of the region seen in Fig. 8.4b), and decomposition revealed that five regions could be identified. Three of them showed the same diffraction pattern, Fig. 8.4c), d), e). They are, however, rotated in relation to each other. The pattern is rectangular and characteristic of $SrTiO_3$. It can be safely assumed that the pattern corresponds to this crystal structure, as the bottom part of the image in Fig. 8.4c) is, in fact, the substrate. The FFT image of the region shown in Fig. 8.4f), is fragmentary and has just four spots, which suggests that the region at hand is not well-organized and may be polycrystalline. The last region, seen in Fig. 8.4g), is mostly located on the borders of the $SrTiO_3$ regions. Due to its low signal-to-noise ratio and spot location corresponding to $SrTiO_3$ symmetry, this region may correspond to highly defected strontium titanate. The nature of this region, however, cannot be clearly ascertained from the four spots alone, as such rectangular symmetry is common, and may be found in titanium oxides also (e.g. TiO).

The changes in chemical composition were also investigated in the same region as in Fig. 8.4 using EDX, with the results of the decomposition shown in Fig. 8.5. As can be seen, three main regions were separated. The first region, seen in Fig. 8.5b), depicts the crystal bulk and part of the changed region. The EDX spectrum indicates that it is composed of Sr, Ti and O, which, coupled with the FFT images (Fig. 8.4a, b, c), clearly reveals that this region is composed of $SrTiO_3$. The second region (Fig. 8.5c) covers most of the measured sample, with the exception of the bulk of the nanowire and a small part under it. The spectrum has no signs of titanium, only strontium and oxygen. This suggests that the region seen in Fig. 8.4e), g), f) is a mixed region with strontium titanate and a strontium oxide. The fact that this region also covers the area shown in Fig. 8.5b) means that the decomposition is not perfect, and that some overlap due to the similarity and high signal of these two components exists. The last region, seen in Fig. 8.5d), makes up the bulk of the nanowire and part of the modified area over the $SrTiO_3$ bulk. It is composed predominantly of titanium and oxygen, with a small peak of strontium. The FFT images from this region are represented in Fig. 8.4g) and correspond to a not-highly crystalline region, which could be polycrystalline titanium oxide.

The difficulty in clearly distinguishing the phases based on the FFT images and the EDX maps stems from the fact that the lamella is relatively thick, measuring more than 100 nm, which averages the signal over a great volume of material. These results therefore allow only for the preliminary observation of the processes which occur during the oxidation of the nanowire-covered strontium titanate. They point to the fact that great movement of atoms occurs in the surface and subsurface region, which gives rise to new oxide phases. A further, more detailed analysis will require a thinner sample.

The oxidation of strontium titanate has been studied extensively and many observations about the result of this process have been made. The formation of the following entities has been observed in oxidizing conditions on the $SrTiO_3$ crystal: SrO islands [231], a SrOx layer [232], SrO layer with a cover of $SrCO_3$ [233], SrO_x islands [234], plane defects in the form of $SrO \cdot n(SrTiO_3)$ or Ruddlesden-Popper phases [235], microcrystallites of SrO, $SrTi_{12}O_{19}$, or even TiO [236], SrO_x droplets that crystallize into SrO islands [237], SrO in a cubic $SrTiO_3$ phase [238], clustered islands of $Sr_{n+1}Ti_nO_{3n+1}$ composition [239], or even subsurface voids

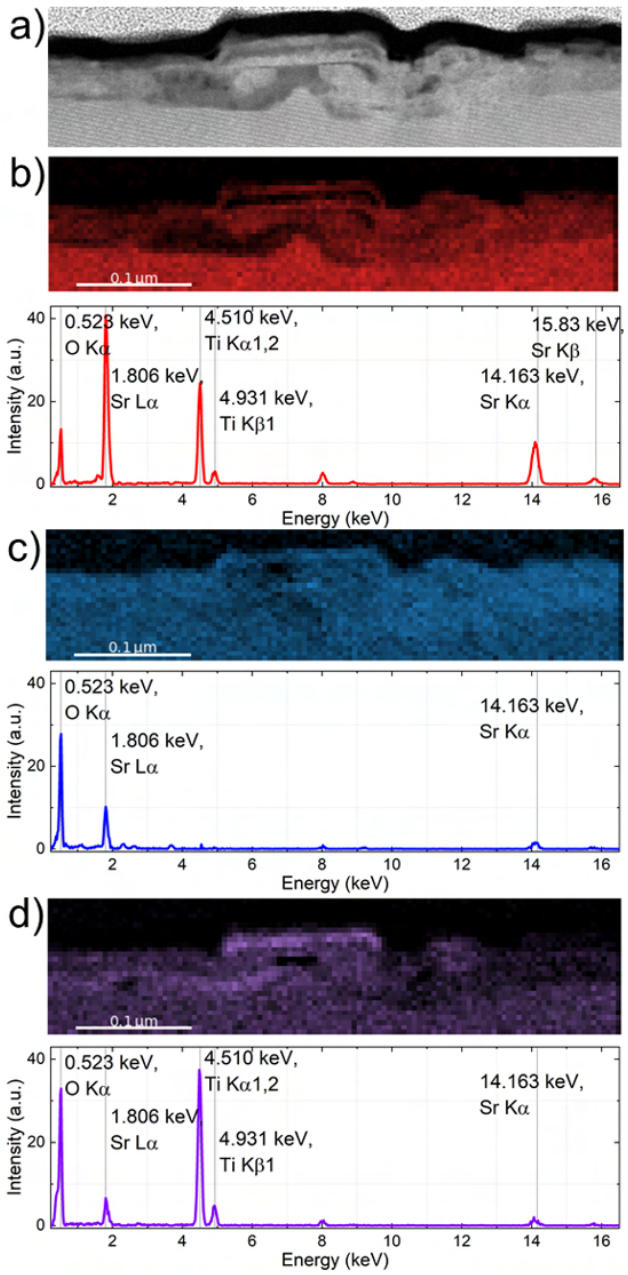

Figure 8.5: a) A HAADF-TEM image at 160k magnification, showing a cross-section of the oxide layer on top of previously nanowire-covered $SrTiO_3$. The results of the decomposition of EDX data showing three regions and their corresponding spectra: b) the $SrTiO_3$ substrate, c) strontium oxide, d) titanium oxide.

[240]. Oxidation has also been observed to change the reconstruction of the surface, with a (1x1) reconstruction during oxidation at 710 °C [241] to c(4x2), (2x1), c(6x2) at temperatures in range of 900 °C to 1100 °C [240]. Furthermore, it has been proposed that at the start of oxidation, up to 0.2 mol % of SrO is redistributed in the bulk in the form of a solid solution [242], and later separates on the surface leading to the growth of structures [238]. A wide range of existence of possible phases can be encountered, depending on the thermodynamic

conditions as the Sr-Ti-O phase diagram shows [243].

The above-mentioned changes in the structure and composition are a consequence of thermodynamically driven strontium segregation [238]. Such evolution of the surface layer of $SrTiO_3$ starts from temperatures as low as 600 °C [244], provided oxidizing conditions. The general equation describing the occurring reaction is [244]:

$$k \cdot \mathrm{SrTiO_3} \longrightarrow p \cdot \mathrm{SrTiO_3} + q \cdot \mathrm{SrO(SrTiO_3)_n} + q \cdot \mathrm{TiO_2}, \tag{8.1}$$

where $k = q \cdot (n + 1) + p$. Szot et al. (1996) [244] reported that the segregation leads to the formation of strontium-rich Ruddlesden-Popper phases at the surface, while under this a layer of titanium-rich Magnéli phases develops. The great variety of experimentally observed oxide phases stems from the discrepancies in the thermodynamic conditions in each of the experiments, which leads to the diversity of strontium oxides phases, due to the fact that oxide crystals can by their nature exist in many forms and stoichiometries. Moreover, the experiments may capture stages of the oxidation, as these experiments have different durations of annealing, as well as different heating and cooling rates. The oxidation of $SrTiO_3$ requires a systematic study in order to provide the general mechanism of the formation of these phases and structures. It seems likely, based on the various results lined out before, that the first stage is the formation of 2D plane defects in the form of Ruddlesden-Popper phases, which, once a critical density has been reached transform into more oxidized forms, such as SrO_x, and finally SrO islands, and layers on the surface. As shown in equation 8.1, the formation of titanium oxide phases is another process that invariably occurs (as this is a segregation reaction). The equation describes equilibrium conditions, but in short time frames, the formation of titanium oxides of lesser oxidation state, i.e. Magnéli phases, would occur.

The changes shown in the HAADF-TEM images and EDX maps can be explained in the context of segregation. The oxidizing conditions lead to changes in the top layer of the crystal, with a multitude of phases coexisting. The FFT images, seen in Fig. 8.4, show that the layer is polycrystalline, and that crystallites of the same pattern, but rotated by some angle, are present. Furthermore, these crystallites are separated from each other by regions of lower density, and worse crystalline order. Taking into account equation 8.1, as well as the conservation of mass, it can be deduced that this region is titanium rich and that it is most likely composed of titanium suboxides, such as Magnéli phases. Additional evidence is provided by the EDX results (Fig. 8.5d), which indicate that these regions tend to be titanium-rich. The exact nature of these phases is not known, due to the averaging related to the significant thickness of the lamella.

The nanowire changes drastically after oxidation, as can be seen in Fig. 8.6. Before oxidation, the nanowire was crystalline, and composed of titanium and oxygen, while after oxidation, the bulk of the nanowire was polycrystalline (Fig. 8.6a) and contained strontium (Fig. 8.6b). Furthermore, the top surface of the nanowire was also covered by strontium-rich oxides. There remains one region containing only titanium and oxygen and it was sandwiched between the previously mentioned regions (Fig. 8.6d). The composition of the titanium-oxygen layer is not known exactly, but it should be closer to titanium dioxide, as the oxidizing condition would certainly increase the oxidation state of titanium ions in the nanostructure. Since rutile

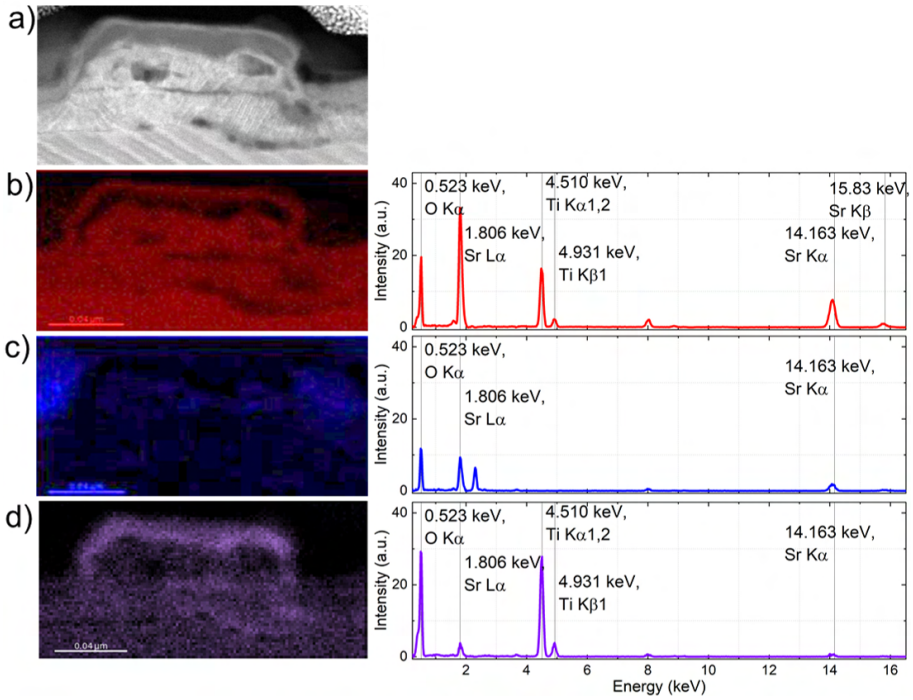

Figure 8.6: a) A HAADF-TEM image at 450k magnification showing a cross-section of the oxide layer on top of the previously nanowire-covered $SrTiO_3$. The results of the decomposition of EDX data showing three regions and their corresponding spectra: b) the $SrTiO_3$ substrate, c) strontium oxide, d) titanium oxide.

TiO_2 is the most stable form in oxygen rich conditions [32], it can be assumed that the end result of prolonged oxidation of TiO would be rutile. However, in the presence of strontium titanate this is not the only possible result and the process depends on the relative stability of rutile as compared to the phases that form in the vicinity.

8.1.4 The electronic properties of the structures grown during oxidation

The electronic properties of the oxidized at 800 °C at oxygen pressure 5×10^{-8} mbar was investigated in situ using KPFM and LC-AFM. As can be seen in Fig. 8.7, the oxidation changes the values of the work function. The low resolution in the KPFM images does not enable the imaging of the individual islands that cover the sample, but it provides the average work function of the surface and nanowire regions. The histogram obtained from this image was compared to the histograms from the reduced and oxidized at room temperature in Fig. 8.8. The surface oxidized at high temperatures has a much higher work function than the work function of the reduced crystal, but it has almost the same work function as the one oxidized at room temperature. The reported value of the work function of SrO is 3.3 eV [245], while the work function of $SrTiO_3$ is 4.2 eV to 4.3 eV[222], [223]. The chemical formula for the Ruddlesden-Popper phases is $SrO \cdot n(SrTiO_3)$, which in the first approximation is in between the ones for SrO and $SrTiO_3$. Accordingly, it may be assumed that the value of the work function is between the two, which would fit the data in histograms.

The changes in conductance are much more dramatic than the changes in work function,

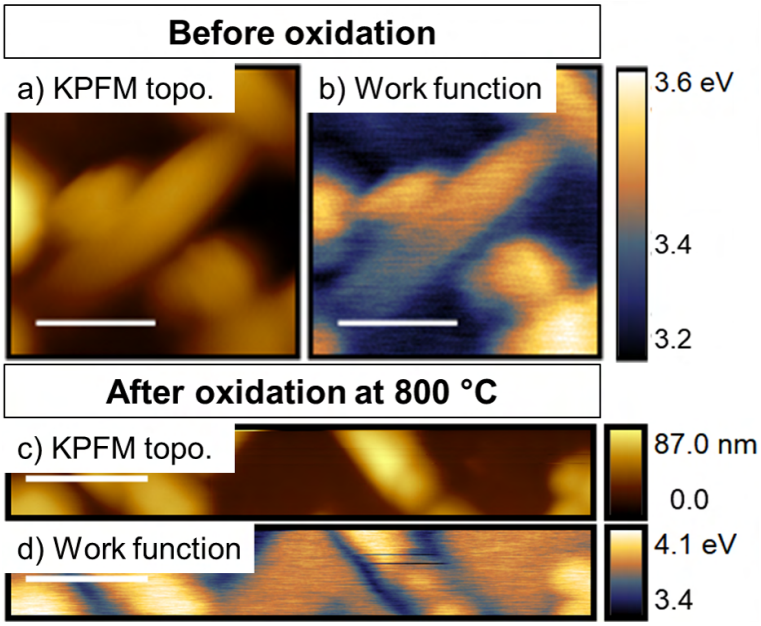

Figure 8.7: The KPFM topography and work function maps before a), b) and after c), d) oxidation at 800 °C at the oxygen pressure of 5×10^{-8} mbar. The scale bar represents 400 nm.

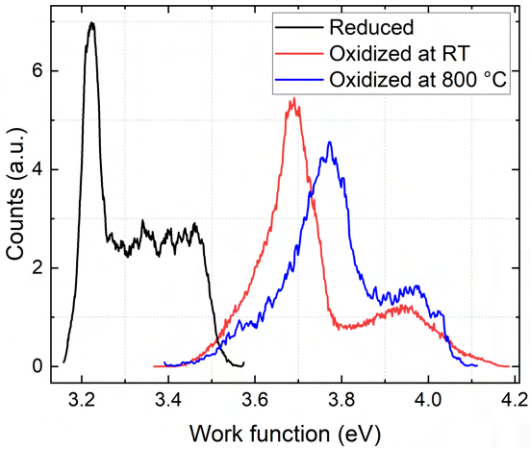

Figure 8.8: The histograms of the work function showing the changes due to oxidation at room temperature and during annealing at 800 °C at the oxygen pressure of 5×10^{-8} mbar. The histograms are based on the maps from Fig. 7.15 and Fig. 8.7.

as can be seen in Fig. 8.9. Oxidation at 800 °C changes the character of the nanowires, with a clear inversion of their properties seen in the current maps. The previously highly-conductive nanowires are nonconductive after oxidation. This is most likely tied to the phase changes in the nanowire bulk, seen in the TEM images (Fig. 8.6). The low conductance may be explained by a possible change of the composition of the bulk of the nanowire from titanium monoxide to a form close to titanium dioxide. The area between the nanowires appears to be highly conductive at large scales, but an investigation at bigger magnifications (Fig. 8.10) reveals that the substrate is not highly conductive, but the nanostructures that have grown on it are. Since from Fig. 8.5 and Fig. 8.9, it appears that structures also grow on the nanowires, the difference

in conductance most likely lies in the interfaces between these structures and the substrate. The STM image in Fig. 8.10a) shows that the changes in the substrate are not extensive, and it appears to be just covered by islands. Thus, the interface would most likely be composed of strontium oxide and $SrTiO_3$, while the interface between the islands and nanowires may be composed of strontium oxide and titanium oxides. Furthermore, the composition of the substrate may be different in the regions covered than in the regions not covered by the newly formed islands.

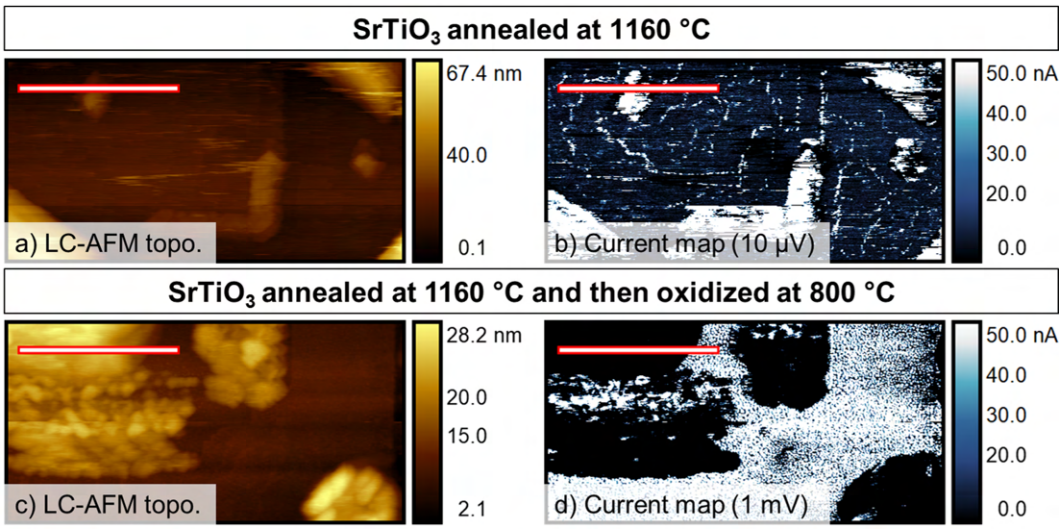

Figure 8.9: The LC-AFM topography and current maps of $SrTiO_3$ before and after oxidation at 800 °C at the oxygen pressure of 5×10^{-8} mbar. The scale bar represents 400 nm.

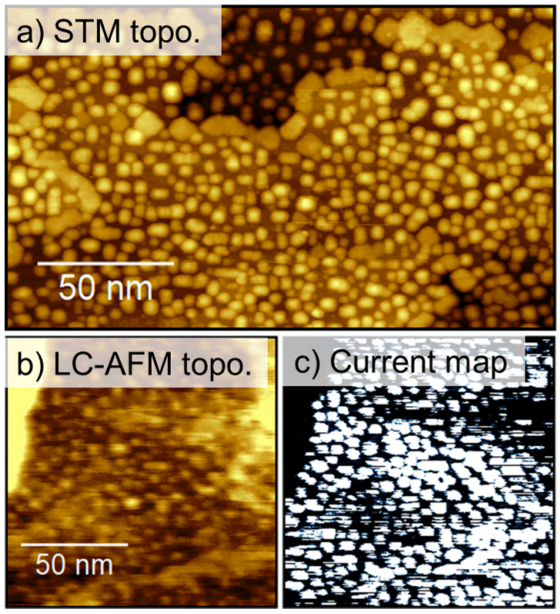

Figure 8.10: a) The STM topography showing nanostructures formed on the surface of $SrTiO_3$ as a result of oxidation at 800 °C at the oxygen pressure of 5×10^{-8} mbar. The LC-AFM b) topography and c) current maps showing the properties of these nanostructures. The STM image was acquired for the bias of 1.3 V and the set point of 10 pA, while the LC-AFM image was acquired for the bias of 1 mV.

The chemical nature of the islands grown during oxidation is difficult to ascertain. Published articles often describe SrO islands growing on the surface of $SrTiO_3$ in oxidizing conditions [231], [237], but SrO crystals are not highly conductive [246] (conductivity of $1 \times 10^{-8}\,\Omega^{-1}\,cm^{-1}$). The high conductance of the observed islands could be due to their small size, and therefore, a high defect density, or to the fact that they could be composed not of SrO, but of SrO_x or even represent a complex entity. The TEM results show a much more oxidized sample, while the LC-AFM results show the beginning stages of oxidation, and therefore, the structure of the islands and the layer studied using TEM could differ.

Chapter 9

Conclusions

The goal of this dissertation was to investigate the effect of reduction and oxidation at nanoscale on the electronic properties of transition metal oxides, i.e. titanium dioxide and strontium titanate. Understanding the redox processes and their effect on the transition metal oxides is deemed to be crucial for targeted design of applications. These processes can be induced in various ways, such as by ion sputtering, annealing in UHV, repeated sputtering and annealing, exposure to oxygen or air, or annealing in oxygen. All of these methods change the equilibrium state of the crystal, affecting its properties. It has been shown in this work that these methods can be used to introduce a significant extent of changes in the chemical composition, morphology, crystallography and electronic properties of the sample.

At first glance, annealing TiO_2 in UHV appears to be a straightforward process, but as the results presented in Chapter 5 demonstrate, this is not the case. The high temperature coupled with reducing conditions not only cause reduction to occur, but also introduce impurity segregation. It is evident even at the macroscopic scale that the crystal is reduced, as it changes color. However, another process, i.e. segregation, also takes place. The first indication of impurity segregation is the appearance of the new reconstruction, c(2x2), at 800 °C, then, at approximately 1100 °C, the well-known calcium-induced c(6x2) reconstruction develops. At the same temperature islands begin to grow, and at extreme temperatures, such as 1350 °C, areas of high roughness can also be seen. These changes in chemical composition are reflected in the sample's electronic properties. The conductance of the surface rises due to reduction, but at close to the temperature where segregation starts to play a significant role, the conductance drops and then rises slowly. LC-AFM maps indicate that calcium-rich islands have low conductivity compared to the terraces. This also suggests that the diffused in the crystal calcium lowers the conductance. The work function of the surface is also affected. The expected monotonic lowering of the work function due to the increasing oxygen defect density is not observed. However, a more complex process can be seen. The work function reacts both to the change in oxygen concentration and to the formation of new reconstructions on the surface. The oxidation at RT of TiO_2 annealed at 800 °C was also investigated, and the fact that both electronic properties react so strongly to the exposure to oxygen suggests that even though impurities are present on the surface, the oxygen deficiency defines the electronic properties of titanium dioxide. Chapter 5 demonstrates that annealing in UHV is a complex process which leads not only reduction, but also to the undesirable effect of segregation.

Chapter 6 described the changes that occur in titanium dioxide as a result of ion sputtering, following annealing and repeated sputtering and annealing. The repeated sputtering and annealing, commonly known as cleaning cycles, is a time-tested technique of obtaining a clean (1x1) reconstructed TiO_2 (110) surface. Accordingly, this method is used around the world as

a way of preparing the surface for experiments. The goal of the chapter was to investigate how these two reducing processes, sputtering and annealing, can lead to a stoichiometric surface. It was demonstrated that sputtering causes the surface to become rough, with no long-range ordering, and it leads to the surface being highly non-stoichiometric, with 35 % titanium ions at the third oxidation state and 5 % at the second. The changes in composition are present to up to the depth of 8 nm. The high number of reduced species on the surface leads to a high, metallic-like conductance and very low work function. The subsequent annealing changes the surface drastically: long-range order reappears in the form of the stoichiometric (1x1) reconstruction and the surface is covered with large terraces. Furthermore, the XPS spectrum show that all titanium ions are in the form of Ti^{4+}, however SIMS profiles indicate that the subsurface layer is affected by the CCs, up to the depth of 4 nm, a slight non-stoichiometry can be detected. The work function reflects the restoration of order and stoichiometry, as it increases drastically, and the conductance drops and displays semiconductor-like behavior. The investigations of repeated CCs show that even though the surface remains stoichiometric and has the (1x1) reconstruction, the electronic properties are not constant. The conductance increases, and the I-V curves become more and more metallic-like with the increase in the number of CCs, while the work function also increases and then levels out. This steep change then plateau behavior is the same for both properties, and stems from the fact that both of them are surface properties and even though sputtering and annealing keep on changing the crystal's composition, these properties are not sensitive to that. Accordingly, it can be concluded that after a critical number of cycles, regardless of the number of cycles that are performed, the same surface is obtained. The above-mentioned results indicate that the act of destroying the long-range order and stoichiometry during sputtering and the total recrystallization of the surface allows for better stoichiometry of the surface to be reached (regardless of the fact that this process leads more reduction of the whole crystal). This result indicates why cleaning cycles are preferential over only annealing as a surface-preparation method. Furthermore, the CC preparation method reliably removes the impurities that segregate during annealing, as it was shown on the SIMS spectra. As was shown in this work, impurities affect the work function drastically, so their removal is of utmost importance. This dissertation also demonstrated that the mechanism of reduction due to a single round of sputtering and annealing and of multiple cycles of equivalent fluence is not the same. This is because, sputtering in a single step reduces the crystal only up to a point and then simply thins it, while doing it in multiple cycles, makes further reduction possible. The crystal is annealed between the sputtering stages, thus the crystal's surface can recrystallize and reoxidize, therefore each time during sputtering, a quazi-stoichiometric surface is sputtered. This leads to the paradoxical situation where multiple cycles reduce and change the crystal to a greater extent than a single cycle of equivalent fluence, and yet the resulting surface is cleaner and more stoichiometric.

The effect of thermal annealing in UHV on the electronic properties and morphology of $SrTiO_3$ was described in Chapter 7. At the relatively low temperatures (up to 1100 °C), the dominant process during annealing of strontium titanate is reduction. In this regime, the effect of the presence of oxygen getter substance was studied. What was discovered was that even at such temperatures, the oxygen partial pressure, which is influenced by the getter

substance, affects the properties of the obtained surface. The lower oxygen pressure leads to a higher reduction of the crystal, which influences the reconstruction of the surface. The crystal annealed without a getter in the vicinity has the (1x1) reconstruction even at 1100 °C, while the crystal which was annealed on silicon evolves through the (2x2), to c(2x2) and finally the ($\sqrt{13}$x$\sqrt{13}$ R33.7°) reconstruction. These differences are reflected in the work function, with the $SrTiO_3$ annealed on TiO_2, maintaining approximately the same work function regardless of the temperature, while the surface annealed on Si shows a sudden drop in the work function of 0.8 eV, at temperatures higher than 800 °C. These results show that when designing experiments into the redox of transition metal oxides, an important consideration is that there are substances that will affect the oxygen partial pressure and therefore the rate of reduction, which may impact the results of the experiments.

The second part of Chapter 7 was concerned with higher annealing temperatures, which is a regime where not only reduction takes place but incongruent effusion also occurs. This process takes place at high temperatures and at low oxygen partial pressures, and leads to the decomposition of the crystal by means of intense strontium effusion. As a result, nanowires form on the surface of the crystal, with their bulk made up of TiO and their surface of Ti_3O_5, as shown for the first time using EBSD. Moreover, it has been presented that different oxygen getters lower the oxygen partial pressure with different intensity. This was proven by the observation that different stages of growth of the nanowires can be seen at the same temperature of the crystal in presence of titanium or silicon. When annealing in the presence of titanium, nanowires can be seen even at 1050 °C, while in the case of silicon getter, nanowires develop at approximately 1150 °C. This shows that titanium lowers the oxygen partial pressure much more than silicon. This chapter also described the end stages of the decomposition of strontium titanate. The manner in which nanowires grow and form a porous, titanium suboxide layer is demonstrated. The electronic properties of the nanowire-covered strontium titanate were studied in the context of oxidation. It was found that the nanowires remain highly conductive even after exposure to oxygen at RT. The work function, however, increased, which implies that some oxidation takes place, but not significantly enough to affect conductivity. During exposure to air, it was discovered that the work function increases by approx. the same amount as in the case of pure oxygen. The only difference was that water adsorbs on the surface, which increases the work function by approximately 0.4 eV. In the time frames of the experiment, organic adsorbates present in air do not seem to affect the properties of the sample.

Chapter 8 described the effect of annealing in oxygen on nanowire-covered strontium titanate. Two regimes were studied, i.e. low and high oxygen pressure. In both cases the morphology of the surface changes as new oxide structures grow on it. At low oxygen pressures, the surface becomes covered with nanostructures, but it retains some of its previous features. The $SrTiO_3$ diffraction pattern becomes weaker, but it is still present, which indicates that at this stage, the terraces are still made up of this crystal. The chemical composition of the nanostructures is not known, but based on published literature, it is most likely SrO_x. The electronic properties of the surface are affected by annealing in oxygen, as the nanowires switch off and are no longer conductive. The nanostructures, on the other hand, conduct electricity very well. Surprisingly, the work function remains almost exactly the same as for samples

oxidized at RT. This most likely means that the new structures which dominate the surface have a work function that is very close to the work function of strontium titanate. At high oxygen pressure, the situation changes, with the surface completely covered with an oxide film. A TEM investigation showed that the crystal was drastically changed, the $SrTiO_3$ substrate was covered with a layer composed of titanium oxides and strontium oxides, intertwined together. The film appears to be polycrystalline, with areas of very low crystallinity. The nanowires are completely changed by the harsh oxidation, leaving intact just their shape and the thin layer of titanium oxide in them.

The processes investigated in this dissertation can be considered as means of inducing change in the crystals by affecting the equilibrium concentration of oxygen vacancies. During reduction, vacancy formation is induced, while during oxidation, vacancy annihilation is induced. These changes occur, first and foremost, on the surface, but, given appropriate conditions, changes can occur in the whole crystal volume. Even though the presented experiments mostly modify the depth of only several nanometers of the crystal, the changes in properties are not minuscule, but drastic. What was observed was the complete switching of electric properties, from non-conductive to conductive, as well as extensive changes in the work function, by even 150 %. The changes in the equilibrium conditions led to movement of atoms leading to the formation of new phases, segregation of impurities and rearrangement of atoms on the surface. The reversal of some of the changes was possible through exposing the crystals to oxygen, as oxygen was incorporated into the reduced crystal. Furthermore, oxidation was shown to be a means of new phase formation. All of this demonstrates that redox processes can be used to modify transition metal oxides, in their composition, crystal structure and properties, in order to make them suitable for a variety of experiments and applications. It is hoped that this dissertation will be used as a road-map to other researchers investigating the redox processes at nanoscale.

Bibliography

[1] S. Cao, T.-s. Chan, Y.-r. Lu, X. Shi, B. Fu, Z. Wu, H. Li, K. Liu, S. Alzuabi, P. Cheng, M. Liu, T. Li, X. Chen, and L. Piao, "Nano Energy Photocatalytic pure water splitting with high efficiency and value by Pt/porous brookite TiO2 nanoflutes," *Nano Energy*, vol. 67, no. October 2019, p. 104287, 2020.

[2] T. H. Chiang, H. Lyu, T. Hisatomi, Y. Goto, T. Takata, M. Katayama, T. Minegishi, and K. Domen, "Efficient Photocatalytic Water Splitting Using Al-Doped SrTiO3 Coloaded with Molybdenum Oxide and Rhodium-Chromium Oxide," *ACS Catal.*, vol. 8, no. 4, pp. 2782–2788, 2018.

[3] C. Him, A. Tsang, K. Li, Y. Zeng, W. Zhao, T. Zhang, Y. Zhan, and R. Xie, "Titanium oxide based photocatalytic materials development and their role of in the air pollutants degradation: Overview and forecast," *Environ. Int.*, vol. 125, no. January, pp. 200–228, 2019.

[4] K. W. Shah and W. Li, "A review on catalytic nanomaterials for volatile organic compounds VOC removal and their applications for healthy buildings," *Nanomaterials*, vol. 9, no. 6, 2019.

[5] K. Misawa, Y. Sekine, Y. Kusukubo, and K. Sohara, "Photocatalytic degradation of atmospheric fine particulate matter (PM2.5) collected on TiO2 supporting quartz fibre filter," *Environ. Technol. (United Kingdom)*, vol. 41, no. 10, pp. 1266–1274, 2020.

[6] C. G. Lee, H. Javed, D. Zhang, J. H. Kim, P. Westerhoff, Q. Li, and P. J. Alvarez, "Porous Electrospun Fibers Embedding TiO2 for Adsorption and Photocatalytic Degradation of Water Pollutants," *Environ. Sci. Technol.*, vol. 52, no. 7, pp. 4285–4293, 2018.

[7] M. Hamerski, J. Grzechulska, and A. W. Morawski, "Photocatalytic purification of soil contaminated with oil using modified TiO2 powders," *Sol. Energy*, vol. 66, no. 6, pp. 395–399, 1999.

[8] M. Cheng, G. Zeng, D. Huang, C. Lai, P. Xu, C. Zhang, and Y. Liu, "Hydroxyl radicals based advanced oxidation processes (AOPs) for remediation of soils contaminated with organic compounds: A review," *Chem. Eng. J.*, vol. 284, pp. 582–598, 2016.

[9] O. Almora, L. G. Gerling, C. Voz, R. Alcubilla, and J. Puigdollers, "Solar Energy Materials and Solar Cells Superior performance of V2O5 as hole selective contact over other transition metal oxides in silicon heterojunction solar cells," *Sol. Energy Mater. Sol. Cells*, vol. 168, no. February, pp. 221–226, 2017.

[10] T. Mahmoudi, Y. Wang, and Y. B. Hahn, "SrTiO3/Al2O3-Graphene Electron Transport Layer for Highly Stable and Efficient Composites-Based Perovskite Solar Cells with 20.6% Efficiency," *Adv. Energy Mater.*, vol. 10, no. 2, pp. 1–9, 2020.

[11] X. Li, J. Yu, M. Jaroniec, and X. Chen, "Cocatalysts for selective photoreduction of CO2 into solar fuels," *Chem. Rev.*, vol. 119, no. 6, pp. 3962–4179, 2019.

[12] A. M. Abdalla, S. Hossain, A. T. Azad, P. M. I. Petra, F. Begum, S. G. Eriksson, and A. K. Azad, "Nanomaterials for solid oxide fuel cells: A review," *Renew. Sustain. Energy Rev.*, vol. 82, no. August 2017, pp. 353–368, 2018.

[13] Y. Wang, J. Guo, T. Wang, J. Shao, D. Wang, and Y. W. Yang, "Mesoporous transition metal oxides for supercapacitors," *Nanomaterials*, vol. 5, no. 4, pp. 1667–1689, 2015.

[14] Y. Li, Z. Wang, R. Midya, Q. Xia, and J. Joshua Yang, "Review of memristor devices in neuromorphic computing: Materials sciences and device challenges," *J. Phys. D. Appl. Phys.*, vol. 51, no. 50, 2018.

[15] F. M. Simanjuntak, T. Ohno, S. Chandrasekaran, T. Y. Tseng, and S. Samukawa, "Neutral oxygen irradiation enhanced forming-less ZnO-based transparent analog memristor devices for neuromorphic computing applications," *Nanotechnology*, vol. 31, no. 26, 2020.

[16] A. Happy, M. Soumya, S. Venkat Kumar, S. Rajeshkumar, N. D. Sheba Rani, T. Lakshmi, and V. Deepak Nallaswamy, "Phyto-assisted synthesis of zinc oxide nanoparticles using Cassia alata and its antibacterial activity against Escherichia coli," *Biochem. Biophys. Reports*, vol. 17, no. December 2018, pp. 208–211, 2019.

[17] B. L. da Silva, M. P. Abuçafy, E. B. Manaia, J. A. O. Junior, B. G. Chiari-Andréo, R. C. Pietro, and L. A. Chiavacci, "Relationship between structure and antimicrobial activity of zinc oxide nanoparticles: An overview," *Int. J. Nanomedicine*, vol. 14, pp. 9395–9410, 2019.

[18] R. Pemmada, X. Zhu, M. Dash, Y. Zhou, S. Ramakrishna, X. Peng, V. Thomas, S. Jain, and H. S. Nanda, "Science-based strategies of antiviral coatings with viricidal properties for the COVID-19 like pandemics," *Materials (Basel).*, vol. 13, no. 18, pp. 1–18, 2020.

[19] D. Wang, C. Huang, J. He, X. Che, H. Zhang, and F. Huang, "Enhanced Superconductivity in Rock-Salt TiO," *ACS Omega*, vol. 2, no. 3, pp. 1036–1039, 2017.

[20] W. Zhong, C. T. Au, and Y. W. Du, "Review of magnetocaloric effect in perovskite-type oxides," *Chinese Phys. B*, vol. 22, no. 5, pp. 0–11, 2013.

[21] R. Zhu and R. Yang, "Separation of the piezotronic and piezoresistive effects in a zinc oxide nanowire," *Nanotechnology*, vol. 25, no. 34, 2014.

[22] S. Walia, S. Balendhran, H. Nili, S. Zhuiykov, G. Rosengarten, Q. H. Wang, M. Bhaskaran, S. Sriram, M. S. Strano, and K. Kalantar-zadeh, "Transition metal oxides - Thermoelectric properties," *Prog. Mater. Sci.*, vol. 58, no. 8, pp. 1443–1489, 2013.

[23] C. Rodenbücher, P. Meuffels, G. Bihlmayer, W. Speier, H. Du, A. Schwedt, U. Breuer, C. L. Jia, J. Mayer, R. Waser, and K. Szot, "Electrically controlled transformation of

memristive titanates into mesoporous titanium oxides via incongruent sublimation," *Sci. Rep.*, vol. 8, no. 1, pp. 1–9, 2018.

[24] M. A. Henderson, "A surface science perspective on TiO2 photocatalysis," *Surf. Sci. Rep.*, vol. 66, no. 6-7, pp. 185–297, 2011.

[25] F. H. Jones, "Teeth and bones: Applications of surface science to dental materials and related biomaterials," *Surf. Sci. Rep.*, vol. 42, no. 3-5, pp. 75–205, 2001.

[26] A. M. Samoylov and V. N. Popov, *Titanium Dioxide (TiO2) and Its Applications*. Elsevier, 2021.

[27] K. Möls, L. Aarik, H. Mändar, A. Kasikov, A. Niilisk, R. Rammula, and J. Aarik, "Influence of phase composition on optical properties of TiO2: Dependence of refractive index and band gap on formation of TiO2-II phase in thin films," *Opt. Mater. (Amst).*, vol. 96, no. August, p. 109335, 2019.

[28] A. J. Haider, Z. N. Jameel, and I. H. Al-Hussaini, "Review on: Titanium dioxide applications," *Energy Procedia*, vol. 157, pp. 17–29, 2019.

[29] D. Frederichi, M. H. N. O. Scaliante, and R. Bergamasco, "Structured photocatalytic systems: photocatalytic coatings on low-cost structures for treatment of water contaminated with micropollutants - a short review," *Environ. Sci. Pollut. Res.*, vol. 28, no. 19, pp. 23610–23633, 2021.

[30] U. Diebold, "The surface science of titanium dioxide," *Surf. Sci. Rep.*, vol. 48, no. 5-8, pp. 53–229, 2003.

[31] X. Mao, Z. Wang, X. Lang, Q. Hao, B. Wen, D. Dai, C. Zhou, L. M. Liu, and X. Yang, "Effect of surface structure on the photoreactivity of TiO2," *J. Phys. Chem. C*, vol. 119, no. 11, pp. 6121–6127, 2015.

[32] H. Zhang and J. F. Banfield, "Structural characteristics and mechanical and thermodynamic properties of nanocrystalline TiO2," *Chem. Rev.*, vol. 114, no. 19, pp. 9613–9644, 2014.

[33] D. A. Hanaor and C. C. Sorrell, "Review of the anatase to rutile phase transformation," *J. Mater. Sci.*, vol. 46, no. 4, pp. 855–874, 2011.

[34] C. Rodenbücher, D. Wrana, P. Meuffels, M. Rogala, F. Krok, and K. Szot, "Electrical nanopatterning of TiO2 single crystal surfaces in situ via local resistance and potential switching," *APL Mater.*, vol. 6, no. 6, 2018.

[35] J. K. Burdett, T. Hughbanks, G. J. Miller, J. V. Smith, and J. W. Richardson, "Structural-Electronic Relationships in Inorganic Solids: Powder Neutron Diffraction Studies of the Rutile and Anatase Polymorphs of Titanium Dioxide at 15 and 295 K," *J. Am. Chem. Soc.*, vol. 109, no. 12, pp. 3639–3646, 1987.

[36] D. Mardare, M. Tasca, M. Delibas, and G. I. Rusu, "On the structural properties and optical transmittance of TiO2 r.f. sputtered thin films," *Appl. Surf. Sci.*, vol. 156, no. 1, pp. 200–206, 2000.

[37] J. R. DeVore, "Refractive Indices of Rutile and Sphalerite," *J. Opt. Soc. Am.*, vol. 41, no. 6, p. 416, 1951.

[38] P. W. Tasker, "The stability of ionic crystal surfaces," *J. Phys. C Solid State Phys.*, vol. 12, no. 22, pp. 4977–4984, 1979.

[39] H. Onishi and Y. Iwasawa, "Reconstruction of TiO2(110) surface: STM study with atomic-scale resolution," *Surf. Sci.*, vol. 313, no. 1-2, 1994.

[40] K. Nassau and A. E. Miller, "Strontium titanate: An index to the literature on properties and the growth of single crystals," *J. Cryst. Growth*, vol. 91, no. 3, pp. 373–381, 1988.

[41] M. Neophytou, M. De Bastiani, N. Gasparini, E. Aydin, E. Ugur, A. Seitkhan, F. Moruzzi, Y. Choaie, A. J. Ramadan, J. R. Troughton, R. Hallani, A. Savva, L. Tsetseris, S. Inal, D. Baran, F. Laquai, T. D. Anthopoulos, H. J. Snaith, S. De Wolf, and I. McCulloch, "Enhancing the Charge Extraction and Stability of Perovskite Solar Cells Using Strontium Titanate (SrTiO3) Electron Transport Layer," *ACS Appl. Energy Mater.*, 2019.

[42] K. Szot, W. Speier, G. Bihlmayer, and R. Waser, "Switching the electrical resistance of individual dislocations in single-crystalline SrTiO3," *Nat. Mater.*, vol. 5, no. 4, pp. 312–320, 2006.

[43] H. Yang, F. Yan, Y. Lin, and T. Wang, "Novel Strontium Titanate-Based Lead-Free Ceramics for High-Energy Storage Applications," *ACS Sustain. Chem. Eng.*, vol. 5, no. 11, pp. 10215–10222, 2017.

[44] T. K. Townsend, N. D. Browning, and F. E. Osterloh, "Nanoscale strontium titanate photocatalysts for overall water splitting," *ACS Nano*, vol. 6, no. 8, pp. 7420–7426, 2012.

[45] N. K. Pervez, P. J. Hansen, and R. A. York, "High tunability barium strontium titanate thin films for rf circuit applications," *Appl. Phys. Lett.*, vol. 85, no. 19, pp. 4451–4453, 2004.

[46] K. Shibuya, T. Ohnishi, M. Kawasaki, H. Koinuma, and M. Lippmaa, "Metallic LaTiO3 / SrTiO3 superlattice films on the SrTiO3 (100) surface," *Japanese J. Appl. Physics, Part 2 Lett.*, vol. 43, no. 9 AB, 2004.

[47] R. K. Singh, J. Narayan, A. K. Singh, and J. Krishnaswamy, "In situ processing of epitaxial Y-Ba-Cu-O high Tc superconducting films on (100) SrTiO3 and (100) YS-ZrO2 substrates at 500-650 °C," *Appl. Phys. Lett.*, vol. 54, no. 22, pp. 2271–2273, 1989.

[48] U. Aschauer and N. A. Spaldin, "Competition and cooperation between antiferrodistortive and ferroelectric instabilities in the model perovskite SrTiO3," *J. Phys. Condens. Matter*, vol. 26, no. 12, 2014.

[49] R. Merkle and J. Maier, "How is oxygen incorporated into oxides? A comprehensive kinetic study of a simple solid-state reaction with SrTiO3 as a model material," *Angew. Chemie - Int. Ed.*, vol. 47, no. 21, pp. 3874–3894, 2008.

[50] K. Szot, C. Rodenbücher, G. Bihlmayer, W. Speier, R. Ishikawa, N. Shibata, and Y. Ikuhara, "Influence of dislocations in transition metal oxides on selected physical and chemical properties," *Crystals*, vol. 8, no. 6, 2018.

[51] B. L. Phoon, C. W. Lai, J. C. Juan, P. L. Show, and W. H. Chen, "A review of synthesis and morphology of SrTiO3 for energy and other applications," *Int. J. Energy Res.*, vol. 43, no. 10, pp. 5151–5174, 2019.

[52] Y. Ma, Z. Wu, H. Wang, G. Wang, Y. Zhang, P. Hu, Y. Li, D. Gao, H. Pu, B. Wang, and X. Qi, "Synthesis of nanocrystalline strontium titanate by a sol-gel assisted solid phase method and its formation mechanism and photocatalytic activity," *CrystEngComm*, vol. 21, no. 26, pp. 3982–3992, 2019.

[53] M. R. Castell, "Scanning tunneling microscopy of reconstructions on the SrTiO3(0 0 1) surface," *Surf. Sci.*, vol. 505, pp. 1–13, 2002.

[54] D. B. Mitzi, "Introduction: Perovskites," *Chem. Rev.*, vol. 119, no. 5, pp. 3033–3035, 2019.

[55] C. R. Kalaiselvi, N. Muthukumarasamy, D. Velauthapillai, M. Kang, and T. S. Senthil, "Importance of halide perovskites for next generation solar cells – A review," *Mater. Lett.*, vol. 219, pp. 198–200, 2018.

[56] R. A. Cowley, "The phase transition of strontium titanate," *Philos. Trans. R. Soc. A Math. Phys. Eng. Sci.*, vol. 354, no. 1720, pp. 2799–2814, 1996.

[57] W. Sigle, C. Sarbu, D. Brunner, and M. Rühle, "Dislocations in plastically deformed SrTiO3," *Philos. Mag.*, vol. 86, no. 29-31, pp. 4809–4821, 2006.

[58] H. W. Eng, P. W. Barnes, B. M. Auer, and P. M. Woodward, "Investigations of the electronic structure of d0 transition metal oxides belonging to the perovskite family," *J. Solid State Chem.*, vol. 175, no. 1, pp. 94–109, 2003.

[59] L. F. Zagonel, M. Bäurer, A. Bailly, O. Renault, M. Hoffmann, S. J. Shih, D. Cockayne, and N. Barrett, "Orientation-dependent work function of insitu annealed strontium titanate," *J. Phys. Condens. Matter*, vol. 21, no. 31, 2009.

[60] A. Ohtomo and H. Y. Hwang, "A high-mobility electron gas at the LaAlO3/SrTiO3 heterointerface," *Nature*, vol. 427, no. January, pp. 423–427, 2004.

[61] A. Cavallaro, B. Ballesteros, R. Bachelet, and J. Santiso, "Heteroepitaxial orientation control of YSZ thin films by selective growth on SrO-, TiO2-terminated SrTiO3 crystal surfaces," *CrystEngComm*, vol. 13, no. 5, pp. 1625–1631, 2011.

[62] G. Koster, B. L. Kropman, G. J. Rijnders, D. H. Blank, and H. Rogalla, "Quasi-ideal strontium titanate crystal surfaces through formation of strontium hydroxide," *Appl. Phys. Lett.*, vol. 73, no. 20, pp. 2920–2922, 1998.

[63] M. Kawasaki, K. Takahashi, T. Maeda, R. Tsuchiya, M. Shinohara, O. Ishiyama, T. Yonezawa, M. Yoshimoto, and H. Koinuma, "Atomic control of the SrTiO3 crystal surface," *Science (80-.).*, vol. 266, no. 5190, pp. 1540–1542, 1994.

[64] M. Radovic, N. Lampis, F. M. Granozio, P. Perna, Z. Ristic, M. Salluzzo, C. M. Schlepütz, and U. S. Di Uccio, "Growth and characterization of stable SrO-terminated SrTiO3 surfaces," *Appl. Phys. Lett.*, vol. 94, no. 2, pp. 1–4, 2009.

[65] D. H. Blank, G. Koster, G. Rijnders, E. Van Setten, P. Slycke, and H. Rogalla, "Imposed layer-by-layer growth by pulsed laser interval deposition," *Appl. Phys. A Mater. Sci. Process.*, vol. 69, no. 7, pp. 223–226, 1999.

[66] F. C. Walsh and R. G. Wills, "The continuing development of Magnéli phase titanium sub-oxides and Ebonex electrodes," *Electrochim. Acta*, vol. 55, no. 22, pp. 6342–6351, 2010.

[67] E. Verrelli and D. Tsoukalas, "Cluster beam synthesis of metal and metal-oxide nanoparticles for emerging memories," *Solid. State. Electron.*, vol. 101, pp. 95–105, 2014.

[68] A. Skopp, N. Kelling, M. Woydt, and L. M. Berger, "Thermally sprayed titanium suboxide coatings for piston ring/cylinder liners under mixed lubrication and dry-running conditions," *Wear*, vol. 262, no. 9-10, pp. 1061–1070, 2007.

[69] J. F. Baumard, D. Panis, and A. M. Anthony, "A study of TiO system between Ti3O5 and TiO2 at high temperature by means of electrical resistivity," *J. Solid State Chem.*, vol. 20, no. 1, pp. 43–51, 1977.

[70] M. V. Ganduglia-Pirovano, A. Hofmann, and J. Sauer, "Oxygen vacancies in transition metal and rare earth oxides: Current state of understanding and remaining challenges," *Surf. Sci. Rep.*, vol. 62, no. 6, pp. 219–270, 2007.

[71] G. V. Samsonov, *the Oxide Handbook*. IFI/Plenum, first ed., 1973.

[72] K. T. Jacob, S. M. Hoque, and Y. Waseda, "Synergistic use of thermogravimetric and electrochemical techniques for thermodynamic study of TiOx (from 1.67 to 2.0) at 1573 K," *Mater. Trans. JIM*, vol. 41, no. 6, pp. 681–689, 2000.

[73] R. Roy and W. B. White, "Growth of titanium oxide crystals of controlled stoichiometry and order," *J. Cryst. Growth*, vol. 13-14, no. C, pp. 78–83, 1972.

[74] K. Szot, M. Rogala, W. Speier, Z. Klusek, A. Besmehn, and R. Waser, "TiO2 - A prototypical memristive material," *Nanotechnology*, vol. 22, no. 25, 2011.

[75] C. Kittel, *Introduction To Solid State Physics.* John Wiley and Sons, Inc, eighth ed., 2005.

[76] L. A. Bursill and B. G. Hyde, "On the Aggregation of Wadsley Defects in Slightly Reduced Rutile," *Philos. Mag.*, vol. 2, no. 1, pp. 277–287, 1970.

[77] D. M. Smyth, "The role of impurities in insultating transition metal oxides," *Prog. Solid State Chem.*, vol. 15, no. 3, pp. 145–171, 1984.

[78] J. S. Anderson and B. G. Hyde, "On the possible role of dislocations in generating ordered and disordered shear structures," *J. Phys. Chem. Solids*, vol. 28, no. 8, pp. 1393–1408, 1967.

[79] M. Rogala, G. Bihlmayer, W. Speier, Z. Klusek, C. Rodenbücher, and K. Szot, "Resistive Switching of a Quasi-Homogeneous Distribution of Filaments Generated at Heat-Treated TiO2 (110)-Surfaces," *Adv. Funct. Mater.*, vol. 25, no. 40, pp. 6382–6389, 2015.

[80] K. Szot, G. Bihlmayer, and W. Speier, "Nature of the resistive switching phenomena in TiO2 and SrTiO3. origin of the reversible insulator-metal transition," *Solid State Phys. - Adv. Res. Appl.*, vol. 65, pp. 353–559, 2014.

[81] P. Gumbsch, S. Taeri-Baghbadrani, D. Brunner, W. Sigle, and M. Rühle, "Plasticity and an inverse brittle-to-ductile transition in strontium titanate," *Phys. Rev. Lett.*, vol. 87, no. 8, pp. 85505–1–85505–2, 2001.

[82] P. Hirel, P. Carrez, and P. Cordier, "From glissile to sessile: Effect of temperature on (110) dislocations in perovskite materials," *Scr. Mater.*, vol. 120, pp. 67–70, 2016.

[83] R. Wang and S. M. Shapiro, "Structural defects and the origin of the second length scale in SrTiO3," *Phys. Rev. Lett.*, vol. 80, no. 11, pp. 2370–2373, 1998.

[84] B. Magyari-Köpe, S. G. Park, H. D. Lee, and Y. Nishi, "First principles calculations of oxygen vacancy-ordering effects in resistance change memory materials incorporating binary transition metal oxides," *J. Mater. Sci.*, vol. 47, no. 21, pp. 7498–7514, 2012.

[85] D. Wrana, C. Rodenbücher, W. Bełza, K. Szot, and F. Krok, "In situ study of redox processes on the surface of SrTiO3 single crystals," *Appl. Surf. Sci.*, vol. 432, pp. 46–52, 2018.

[86] W. Göpel, J. A. Anderson, D. Frankel, M. Jaehnig, K. Phillips, J. A. Schäfer, and G. Rocker, "Surface defects of TiO2(110): A combined XPS, XAES AND ELS study," *Surf. Sci.*, vol. 139, no. 2-3, pp. 333–346, 1984.

[87] D. J. Smith, M. R. McCartney, and L. A. Bursill, "The electron-beam-induced reduction of transition metal oxide surfaces to metallic lower oxides," *Ultramicroscopy*, vol. 23, no. 3-4, pp. 299–303, 1987.

[88] L. Andronic and A. Enesca, "Black TiO2 Synthesis by Chemical Reduction Methods for Photocatalysis Applications," *Front. Chem.*, vol. 8, no. November, pp. 1–8, 2020.

[89] D. Wrana, C. Rodenbücher, M. Krawiec, B. R. Jany, J. Rysz, M. Ermrich, K. Szot, and F. Krok, "Tuning the surface structure and conductivity of niobium-doped rutile TiO2 single crystals via thermal reduction," *Phys. Chem. Chem. Phys.*, vol. 19, no. 45, pp. 30339–30350, 2017.

[90] M. Li, W. Hebenstreit, U. Diebold, A. M. Tyryshkin, M. K. Bowman, G. G. Dunham, and M. A. Henderson, "The Influence of the Bulk Reduction State on the Surface Structure and Morphology of Rutile TiO2(110) Single Crystals," *J. Phys. Chem. B*, vol. 104, no. 20, pp. 4944–4950, 2000.

[91] M. Bowker and R. A. Bennett, "The role of Ti3+ interstitials in TiO2(110) reduction and oxidation," *J. Phys. Condens. Matter*, vol. 22, no. 5, 2010.

[92] M. Rogala, G. Bihlmayer, P. Dabrowski, C. Rodenbücher, D. Wrana, F. Krok, Z. Klusek, and K. Szot, "Self-reduction of the native TiO2 (110) surface during cooling after thermal annealing – in-operando investigations," *Sci. Rep.*, vol. 9, no. 1, pp. 1–9, 2019.

[93] W. J. Lo, Y. W. Chung, and G. A. Somorjai, "Electron spectroscopy studies of the chemisorption of O2, H2 and H2O on the TiO2(l00) surfaces with varied stoichiometry: evidence for the photogeneration of Ti3+ and for its importance in chemisorption," *Surf. Sci.*, vol. 71, pp. 199–219, 1978.

[94] E. Asari and R. Souda, "Study of TiO2(110)-p(1x1), p(1x2) and p(1x3) surface structures by impact collision ion scattering spectroscopy (ICISS)," *Nucl. Instruments Methods Phys. Res. B*, vol. 163, pp. 396–400, 2000.

[95] H. Onishi and Y. Iwasawa, "STM observation of surface reactions on a metal oxide," *Surf. Sci.*, vol. 358, pp. 773–776, 1996.

[96] R. A. Bennett, P. Stone, N. J. Price, and M. Bowker, "Two (1x2) Reconstructions of TiO2 (110): Surface Rearrangement and Reactivity Studied Using Elevated Temperature Scanning Tunneling Microscopy," *Phys. Rev. Lett.*, vol. 2, no. 110, pp. 3831–3834, 1999.

[97] C. Rodenbücher, P. Meuffels, W. Speier, M. Ermrich, D. Wrana, F. Krok, and K. Szot, "Stability and Decomposition of Perovskite-Type Titanates upon High-Temperature Reduction," *Phys. Status Solidi - Rapid Res. Lett.*, vol. 11, no. 9, pp. 1–4, 2017.

[98] C. Guguschev, C. Guguschev, D. J. Kok, Z. Galazka, D. Klimm, R. Uecker, R. Bertram, M. Naumann, U. Juda, A. Kwasniewski, and M. Bickermann, "Influence of oxygen partial pressure on SrTiO3 bulk crystal growth from non-stoichiometric melts," *CrystEngComm*, vol. 17, no. 17, 2015.

[99] D. Wrana, C. Rodenbücher, B. R. Jany, O. Kryshtal, G. Cempura, A. Kruk, P. Indyka, K. Szot, and F. Krok, "A bottom-up process of self-formation of highly conductive

titanium oxide (TiO) nanowires on reduced SrTiO3," *Nanoscale*, vol. 11, no. 1, pp. 89–97, 2019.

[100] T. Bak, J. Nowotny, M. K. Nowotny, and L. R. Sheppard, "Defect engineering of titanium dioxide," *J. Aust. Ceram. Soc.*, vol. 44, no. 2, pp. 63–67, 2008.

[101] K. Cieślik, D. Wrana, K. Szajna, W. Bełza, M. Rogala, C. Rodenbücher, P. Dąbczyński, K. Szot, and F. Krok, "Tuning the electronic properties of a clean TiO2(1 1 0) surface via repeated sputtering and annealing: A KPFM and LC-AFM study," *Appl. Surf. Sci.*, vol. 571, no. September 2021, 2022.

[102] B. R. Jany, K. Szajna, M. Nikiel, D. Wrana, E. Trynkiewicz, R. Pedrys, and F. Krok, "Energy dependence of nanopillars formation on InSb semiconductor surfaces under gallium FIB and noble gas ions beam irradiation," *Appl. Surf. Sci.*, vol. 327, pp. 86–92, 2015.

[103] Y. Serruys, M. O. Ruault, P. Trocellier, S. Henry, O. Kaïtasov, and P. Trouslard, "Multiple ion beam irradiation and implantation: JANNUS project," *Nucl. Instruments Methods Phys. Res. Sect. B Beam Interact. with Mater. Atoms*, vol. 240, no. 1-2, pp. 124–127, 2005.

[104] M. Rogala, Z. Klusek, C. Rodenbücher, R. Waser, and K. Szot, "Quasi-two-dimensional conducting layer on TiO2 (110) introduced by sputtering as a template for resistive switching," *Appl. Phys. Lett.*, vol. 102, no. 13, pp. 1–5, 2013.

[105] B. M. Pabón, J. I. Beltrán, G. Sánchez-Santolino, I. Palacio, J. López-Sánchez, J. Rubio-Zuazo, J. M. Rojo, P. Ferrer, A. Mascaraque, M. C. Munõz, M. Varela, G. R. Castro, and O. R. De La Fuente, "Formation of titanium monoxide (001) single-crystalline thin film induced by ion bombardment of titanium dioxide (110)," *Nat. Commun.*, vol. 6, no. 001, pp. 1–6, 2015.

[106] V. S. Lusvardi, M. A. Barteau, J. G. Chen, J. Eng, B. Frühberger, and A. Teplyakov, "An NEXAFS investigation of the reduction and reoxidation of TiO2(001)," *Surf. Sci.*, vol. 397, no. 1-3, pp. 237–250, 1998.

[107] S. Hashimoto and A. Tanaka, "Alteration of Ti 2p XPS spectrum for titanium oxide by low-energy Ar ion bombardment," *Surf. Interface Anal.*, vol. 34, no. 1, pp. 262–265, 2002.

[108] R. Shimizu, K. Iwaya, T. Ohsawa, T. Hasegawa, T. Hashizume, and T. Hitosugi, "Simplified method to prepare atomically-ordered TiO2 (1 1 0)-(1 × 1) surfaces with steps and terraces," *Appl. Surf. Sci.*, vol. 257, no. 11, pp. 4867–4869, 2011.

[109] M. Setvin, J. Hulva, G. S. Parkinson, M. Schmid, and U. Diebold, "Electron transfer between anatase TiO2 and an O2 molecule directly observed by atomic force microscopy," *Proc. Natl. Acad. Sci. U. S. A.*, vol. 114, no. 13, pp. E2556–E2562, 2017.

[110] D. S. Humphrey, C. L. Pang, Q. Chen, and G. Thornton, "Electron induced nanoscale engineering of rutile TiO2 surfaces," *Nanotechnology*, vol. 30, no. 2, 2019.

[111] Y. Du, N. A. Deskins, Z. Zhang, Z. Dohnalek, M. Dupuis, and I. Lyubinetsky, "Formation of O adatom pairs and charge transfer upon O2 dissociation on reduced TiO2(110)," *Phys. Chem. Chem. Phys.*, vol. 12, no. 24, pp. 6337–6344, 2010.

[112] D. Katsube, S. Ojima, E. Inami, and M. Abe, "Atomic-resolution imaging of rutile TiO2(110)-(1 × 2) reconstructed surface by non-contact atomic force microscopy," *Beilstein J. Nanotechnol.*, vol. 11, no. 110, pp. 443–449, 2020.

[113] N. G. Petrik and G. A. Kimmel, "Electron- and hole-mediated reactions in UV-irradiated O2 adsorbed on reduced rutile TiO2(110)," *J. Phys. Chem. C*, vol. 115, no. 1, pp. 152–164, 2011.

[114] A. Borodin and M. Reichling, "Characterizing TiO2(110) surface states by their work function," *Phys. Chem. Chem. Phys.*, vol. 13, no. 34, pp. 15442–15447, 2011.

[115] C. M. Yim, C. L. Pang, and G. Thornton, "Oxygen vacancy origin of the surface band-gap state of TiO2(110)," *Phys. Rev. Lett.*, vol. 104, no. 3, pp. 2–5, 2010.

[116] Y. K. Kim and C. C. Hwang, "Photoemission study on the adsorption of ethanol on clean and oxidized rutile TiO2(110)-1 × 1 surfaces," *Surf. Sci.*, vol. 605, no. 23-24, pp. 2082–2086, 2011.

[117] S. D. Sohn, S. H. Kim, S. K. Kwak, and H. J. Shin, "Defect-associated adsorption of monoethanolamine on TiO 2 (1 1 0): An alternative way to control the work function of oxide electrode," *Appl. Surf. Sci.*, vol. 467-468, no. July 2018, pp. 1213–1218, 2019.

[118] C. Zhou, Z. Ma, Z. Ren, X. Mao, D. Dai, and X. Yang, "Effect of defects on photocatalytic dissociation of methanol on TiO 2(110)," *Chem. Sci.*, vol. 2, no. 10, pp. 1980–1983, 2011.

[119] Z. Wu, F. Xiong, Z. Wang, and W. Huang, "Thermal-, photo- and electron-induced reactivity of hydrogen species on rutile TiO2(110) surface: Role of oxygen vacancy," *Chinese Chem. Lett.*, vol. 29, no. 6, pp. 752–756, 2018.

[120] Z. Dohnálek, J. Kim, O. Bondarchuk, J. Mike White, and B. D. Kay, "Physisorption of N2, O2, and CO on fully oxidized TiO2(110)," *J. Phys. Chem. B*, vol. 110, no. 12, pp. 6229–6235, 2006.

[121] R. A. Bennett, "The re-oxidation of the substoichiometric TiO2(110) surface in the presence of crystallographic shear planes," *PhysChemComm*, vol. 3, no. 110, pp. 1–6, 2000.

[122] S. Kashiwaya, J. Morasch, V. Streibel, T. Toupance, W. Jaegermann, and A. Klein, "The Work Function of TiO2," *Surfaces*, vol. 1, no. 1, pp. 73–89, 2018.

[123] H. Onishi and Y. Iwasawa, "Dynamic visualization of a metal-oxide-surface/gas-phase reaction: Time-resolved observation by scanning tunneling microscopy at 800 K," *Phys. Rev. Lett.*, vol. 76, no. 5, pp. 791–794, 1996.

[124] M. Li, W. Hebenstreit, L. Gross, U. Diebold, M. A. Henderson, D. R. Jennison, P. A. Schultz, and M. P. Sears, "Oxygen-induced restructuring of the TiO2(110) surface: a comprehensive study," *Surf. Sci.*, vol. 437, no. 1, pp. 173–190, 1999.

[125] P. Gorai, A. G. Hollister, K. Pangan-Okimoto, and E. G. Seebauer, "Kinetics of oxygen interstitial injection and lattice exchange in rutile TiO2," *Appl. Phys. Lett.*, vol. 104, no. 19, pp. 2–6, 2014.

[126] E. Lira, J. Hansen, P. Huo, R. Bechstein, P. Galliker, E. Lægsgaard, B. Hammer, S. Wendt, and F. Besenbacher, "Dissociative and molecular oxygen chemisorption channels on reduced rutile TiO2(110): An STM and TPD study," *Surf. Sci.*, vol. 604, no. 21-22, pp. 1945–1960, 2010.

[127] S. Wendt, P. T. Sprunger, E. Lira, G. K. Madsen, Z. Li, J. Hansen, J. Matthiesen, A. Blekinge-Rasmussen, E. Lægsgaard, B. Hammer, and F. Besenbacher, "The role of interstitial sites in the Ti3d defect state in the band gap of titania," *Science (80-.).*, vol. 320, no. 5884, pp. 1755–1759, 2008.

[128] A. G. Thomas, W. R. Flavell, A. K. Mallick, A. R. Kumarasinghe, D. Tsoutsou, N. Khan, C. Chatwin, S. Rayner, G. C. Smith, R. L. Stockbauer, S. Warren, T. K. Johal, S. Patel, D. Holland, A. Taleb, and F. Wiame, "Comparison of the electronic structure of anatase and rutile TiO2 single-crystal surfaces using resonant photoemission and x-ray absorption spectroscopy," *Phys. Rev. B - Condens. Matter Mater. Phys.*, vol. 75, no. 3, pp. 1–12, 2007.

[129] M. Setvín, B. Daniel, V. Mansfeldova, L. Kavan, P. Scheiber, M. Fidler, M. Schmid, and U. Diebold, "Surface preparation of TiO2 anatase (101): Pitfalls and how to avoid them," *Surf. Sci.*, vol. 626, pp. 61–67, 2014.

[130] L. P. Zhang, M. Li, and U. Diebold, "Characterization of Ca impurity segregation on the TiO2(110) surface," *Surf. Sci.*, vol. 412-413, pp. 242–251, 1998.

[131] A. Fujishima and K. Honda, "Electrochemical Photolysis of Water at a Semiconductor Electrode," *Nature*, vol. 240, pp. 226–229, 1972.

[132] Y. Xu, S. Wang, J. Yang, B. Han, R. Nie, J. Wang, J. Wang, and H. Jing, "In-situ grown nanocrystal TiO2 on 2D Ti3C2 nanosheets for artificial photosynthesis of chemical fuels," *Nano Energy*, vol. 51, no. June, pp. 442–450, 2018.

[133] M. V. Dozzi and E. Selli, "Doping TiO2 with p-block elements: Effects on photocatalytic activity," *J. Photochem. Photobiol. C Photochem. Rev.*, vol. 14, no. 1, pp. 13–28, 2013.

[134] Y. Ma, X. Wang, Y. Jia, X. Chen, H. Han, and C. Li, "Titanium dioxide-based nanomaterials for photocatalytic fuel generations," *Chem. Rev.*, vol. 114, no. 19, pp. 9987–10043, 2014.

[135] P. S. Basavarajappa, S. B. Patil, N. Ganganagappa, K. R. Reddy, A. V. Raghu, and C. V. Reddy, "Recent progress in metal-doped TiO2, non-metal doped/codoped TiO2 and TiO2 nanostructured hybrids for enhanced photocatalysis," *Int. J. Hydrogen Energy*, vol. 45, no. 13, pp. 7764–7778, 2020.

[136] J. Zhang, Q. Xu, Z. Feng, M. Li, and C. Li, "Importance of the relationship between surface phases and photocatalytic activity of TiO2," *Angew. Chemie - Int. Ed.*, vol. 47, no. 9, pp. 1766–1769, 2008.

[137] Y. K. Kho, A. Iwase, W. Y. Teoh, L. Mädler, A. Kudo, and R. Amal, "Photocatalytic H2 evolution over TiO2 nanoparticles. The synergistic effect of anatase and rutile," *J. Phys. Chem. C*, vol. 114, no. 6, pp. 2821–2829, 2010.

[138] X. Chen, L. Liu, P. Y. Yu, and S. S. Mao, "Increasing solar absorption for photocatalysis with black hydrogenated titanium dioxide nanocrystals," *Science (80-.).*, vol. 331, no. 6018, pp. 746–750, 2011.

[139] P. Ren, M. Song, J. Lee, J. Zheng, Z. Lu, M. Engelhard, X. Yang, X. Li, D. Kisailus, and D. Li, "Edge Dislocations Induce Improved Photocatalytic Efficiency of Colored TiO2," *Adv. Mater. Interfaces*, vol. 6, no. 17, pp. 1–6, 2019.

[140] S. I. Cha, K. H. Hwang, Y. H. Kim, M. J. Yun, S. H. Seo, Y. J. Shin, J. H. Moon, and D. Y. Lee, "Crystal splitting and enhanced photocatalytic behavior of TiO2 rutile nano-belts induced by dislocations," *Nanoscale*, vol. 5, no. 2, pp. 753–758, 2013.

[141] M. Macyk, K. Cieślik, D. Wrana, J. Kuncewicz, K. F., and W. Macyk, "Tuning photoreduction properties of rutile TiO2 through the partial, thermal reduction of Ti IV to Ti III," *Manuscr. preperation*, 2022.

[142] X. Chen and S. S. Mao, "Titanium dioxide nanomaterials: Synthesis, properties, modifications and applications," *Chem. Rev.*, vol. 107, no. 7, pp. 2891–2959, 2007.

[143] Q. Ferreira, G. Brotas, L. Alcácer, and J. Morgado, "Characterization of self-assembled monolayers of thiols on gold using scanning tunneling microscopy," *Proc. Conf. Telecommun. - ConfTele*, vol. 1, no. June 2014, pp. 1149–152, 2009.

[144] N. D. Tersoff, J., Lang, "Theory of Scanning Tunneling Microscopy," *Scanning Tunneling Microsc.*, vol. 27, 1993.

[145] W. A. Hofer, A. S. Foster, and A. L. Shluger, "Theories of scanning probe microscopes at the atomic scale," *Rev. Mod. Phys.*, vol. 75, no. 4, pp. 1287–1331, 2003.

[146] C. Bai, *Scanning Tunneling Microscopy and Its Application.* Springer, second ed., 2000.

[147] M. Ashino, T. Uchihashi, K. Yokoyama, Y. Sugawara, S. Morita, and M. Ishikawa, "Atomic-scale structures on a non-stoichiometric TiO2(110) surface studied by noncontact AFM," *Appl. Surf. Sci.*, vol. 157, no. 4, pp. 212–217, 2000.

[148] G. Mandi, N. Nagy, and K. Palotas, "Arbitrary tip orientation in STM simulations: 3D WKB theory and application to W(110)," 2013.

[149] V. Oura K., V. G. Lifshits, A. A. Saranin, A. V. Zotov, and Ktayama M., *Surface science: An Introduction*, vol. 284. Springer US, 2003.

[150] F. J. Giessibl, "Advances in atomic force microscopy," *Rev. Mod. Phys.*, vol. 75, no. 3, pp. 949–983, 2003.

[151] U. Maver, T. Velnar, M. Gaberšček, O. Planinšek, and M. Finšgar, "Recent progressive use of atomic force microscopy in biomedical applications," *TrAC - Trends Anal. Chem.*, vol. 80, pp. 96–111, 2016.

[152] U. Hartmann, "Magnetic force microscopy," *Mod. Tech. Charact. Magn. Mater.*, pp. 411–451, 2005.

[153] J. A. Christman, H. Maiwa, S. H. Kim, A. I. Kingon, and R. J. Nemanich, "Piezoelectric measurements with atomic force microscopy," *Mater. Res. Soc. Symp. - Proc.*, vol. 541, pp. 617–622, 1999.

[154] W. Melitz, J. Shen, A. C. Kummel, and S. Lee, "Kelvin probe force microscopy and its application," *Surf. Sci. Rep.*, vol. 66, no. 1, pp. 1–27, 2011.

[155] M. Nonnenmacher, M. O'Boyle, and H. K. Wickramasinghe, "Kelvin probe force microscopy," *Appl. Phys. Lett.*, vol. 58, no. 1, 1991.

[156] L. Kelvin, " V. Contact electricity of metals ," *London, Edinburgh, Dublin Philos. Mag. J. Sci.*, vol. 46, no. 278, pp. 82–120, 1898.

[157] F. Krok, K. Sajewicz, J. Konior, M. Goryl, P. Piatkowski, and M. Szymonski, "Lateral resolution and potential sensitivity in Kelvin probe force microscopy: Towards understanding of the sub-nanometer resolution," *Phys. Rev. B - Condens. Matter Mater. Phys.*, vol. 77, no. 23, pp. 1–9, 2008.

[158] T. Hochwitz, "Capacitive effects on quantitative dopant profiling with scanned electrostatic force microscopes," *J. Vac. Sci. Technol. B Microelectron. Nanom. Struct.*, vol. 14, no. 1, p. 457, 1996.

[159] C. C. Williams, "Two-dimensional dopant profiling by scanning capacitance force microscopy," *Annu. Rev. Mater. Sci.*, vol. 210, no. 1-2 SPEC., pp. 93–98, 1999.

[160] S. Sadewasser and M. C. Lux-Steiner, "Correct height measurement in noncontact atomic force microscopy," *Phys. Rev. Lett.*, vol. 91, no. 26, pp. 1–4, 2003.

[161] I. Stich, J. Tobik, R. Perez, K. Terakura, and S. H. Ke, "Tip-surface interactions in noncontact atomic force microscopy on reactive surfaces," *Prog. Surf. Sci.*, vol. 64, no. 3, pp. 179–191, 2000.

[162] C. Rodenbücher, G. Bihlmayer, W. Speier, J. Kubacki, M. Wojtyniak, M. Rogala, D. Wrana, F. Krok, and K. Szot, "Local surface conductivity of transition metal oxides mapped with true atomic resolution †," *Nanoscale*, vol. 10, p. 11498, 2018.

[163] U. Celano, T. Hantschel, G. Giammaria, R. C. Chintala, T. Conard, H. Bender, and W. Vandervorst, "Evaluation of the electrical contact area in contact-mode scanning probe microscopy," *J. Appl. Phys.*, vol. 117, no. 21, 2015.

[164] J. I. Goldstein, D. E. Newbury, R. Michael, J, N. Ritchie, J. J. Scott, and D. C. Joy, *Scanning electron microscopy and X-ray microanalysis.* Kluwer Academic / Plenum Publishers, third ed., 2003.

[165] W. Zhou and Z. L. Wang, *Scanning microscopy for nanotechnology: Techniques and applications.* Springer, 2007.

[166] K. W. Kolasinski, *Surface Science: Foundations of Catalysis and Nanoscience.* Wiley, second ed., 2012.

[167] F. A. Shah, K. Ruscsák, and A. Palmquist, "50 Years of Scanning Electron Microscopy of Bone—a Comprehensive Overview of the Important Discoveries Made and Insights Gained Into Bone Material Properties in Health, Disease, and Taphonomy," *Bone Res.*, vol. 7, no. 1, pp. 1–15, 2019.

[168] B. R. Jany, A. Janas, and F. Krok, "Retrieving the Quantitative Chemical Information at Nanoscale from Scanning Electron Microscope Energy Dispersive X-ray Measurements by Machine Learning," *Nano Lett.*, vol. 17, no. 11, pp. 6520–6525, 2017.

[169] "Electron Backscatter Diffraction, EBSD - Glossary of SEM Terms - JEOL; Date Accessed: 2022-02-02;." https://www.jeol.co.jp/en/words/semterms/search_result.html?keyword=electron backscatter diffraction%2C EBSD.

[170] R. R. Keller and R. H. Geiss, "Transmission EBSD from 10 nm domains in a scanning electron microscope," *J. Microsc.*, vol. 245, no. 3, pp. 245–251, 2012.

[171] M. Faryna, *Dyfrakcja elektronów wstecznie rozproszonych w skaningowym mikroskopie elektronowym - elementy teorii i praktyki.* Krakow: Wydawnictwo AGH, 2012.

[172] K. Sohlberg, T. J. Pennycook, W. Zhou, and S. J. Pennycook, "Insights into the physical chemistry of materials from advances in HAADF-STEM," *Phys. Chem. Chem. Phys.*, vol. 17, no. 6, pp. 3982–4006, 2015.

[173] L. Lambert and T. Mulvey, "Designer Extraordinaire of the Electron Microscope: A Memoir," *Adv. Imaging Electron Phys.*, vol. 95, 1906.

[174] V. J. Keast, "Application of EELS in materials science," *Mater. Charact.*, vol. 73, pp. 1–7, 2012.

[175] A. Klump, C. Zhou, F. A. Stevie, R. Collazo, and Z. Sitar, "Improvement in detection limit for time-of-flight SIMS analysis of dopants in GaN structures," *J. Vac. Sci. Technol. B, Nanotechnol. Microelectron. Mater. Process. Meas. Phenom.*, vol. 36, no. 3, p. 03F102, 2018.

[176] P. Dąbczyński, *Engineering of interfaces in hybrid-organic electronic devices.* PhD thesis, 2019.

[177] L. R. Sheppard, T. Dittrich, and M. K. Nowotny, "The impact of niobium surface segregation on charge separation in niobium-doped titanium dioxide," *J. Phys. Chem. C*, vol. 116, no. 39, pp. 20923–20929, 2012.

[178] J. Likonen, M. Hautala, and I. Koponen, "The effect of ion beam mixing on SIMS depth resolution," *Nucl. Inst. Methods Phys. Res. B*, vol. 64, no. 1-4, pp. 149–152, 1992.

[179] N. Winograd, Z. Postawa, J. Cheng, C. Szakal, J. Kozole, and B. J. Garrison, "Improvements in SIMS continue. Is the end in sight?," *Appl. Surf. Sci.*, vol. 252, no. 19, pp. 6836–6843, 2006.

[180] M. A. Henderson, "A surface perspective on self-diffusion in rutile TiO2," *Surf. Sci.*, vol. 419, no. 2-3, pp. 174–187, 1999.

[181] V. R. Deline, W. Katz, C. A. Evans, and P. Williams, "Mechanism of the SIMS matrix effect," *Appl. Phys. Lett.*, vol. 33, no. 9, pp. 832–835, 1978.

[182] Y. Gao, "A new secondary ion mass spectrometry technique for III-V semiconductor compounds using the molecular ions CsM+," *J. Appl. Phys.*, vol. 64, no. 7, pp. 3760–3762, 1988.

[183] V. Mazel and P. Richardin, "ToF-SIMS Study of Organic Materials in Cultural Heritage: Identification and Chemical Imaging," *Org. Mass Spectrom. Art Archaeol.*, pp. 433–457, 2009.

[184] K. Cieslik, *The studies of thermal stability of molecular structures grown on oxide metal crystals by means of temperature programmed desorption (TPD).* PhD thesis, 2018.

[185] R. Waser, T. Baiatu, and K. Hardtl, "dc Electrical Degradation of Perovskite-Type Titanates: I, Ceramics," *J. Am. Ceram. Soc.*, vol. 73, no. 6, pp. 1645–1653, 1990.

[186] F. Krok, J. J. Kolodziej, B. Such, P. Czuba, P. Struski, P. Piatkowski, and M. Szymonski, "Dynamic force microscopy and Kelvin probe force microscopy of KBr film on InSb (001) surface at submonolayer coverage," *Surf. Sci.*, vol. 566-568, no. 1-3 PART 1, pp. 63–67, 2004.

[187] W. Melitz, J. Shen, S. Lee, J. S. Lee, A. C. Kummel, R. Droopad, and E. T. Yu, "Scanning tunneling spectroscopy and Kelvin probe force microscopy investigation of Fermi energy level pinning mechanism on InAs and InGaAs clean surfaces," *J. Appl. Phys.*, vol. 108, no. 2, 2010.

[188] H. K. Jeong, C. Yang, B. S. Kim, and K. J. Kim, "Valence band of graphite oxide," *Epl*, vol. 92, no. 3, 2010.

[189] U. Diebold, "The surface science of titanium dioxide," *Surf. Sci. Rep.*, vol. 48, no. 1, pp. 53–229, 2002.

[190] M. Kamaratos and D. Vlachos, "Potassium adsorption on TiO 2 (100)," *J. Phys. Condens. Matter*, vol. 2, no. 100, 1991.

[191] G. Thornton, "Poisons and promoters on TiO2 surfaces," *Vacuum*, vol. 43, no. 11, pp. 1133–1135, 1992.

[192] H. Nörenberg and J. H. Harding, "Formation of highly ordered Ca-overlayers on TiO2(110) surfaces studied by scanning tunneling microscopy and atomistic simulation," *Appl. Surf. Sci.*, vol. 142, no. 1, pp. 174–176, 1999.

[193] O. Bikondoa, C. L. Pang, C. A. Muryn, B. G. Daniels, S. Ferrero, E. Michelangeli, and G. Thornton, "Ordered overlayers of Ca on TiO2(110)-1×1," *J. Phys. Chem. B*, vol. 108, no. 43, pp. 16768–16771, 2004.

[194] G. Serrano, B. Bonanni, T. Kosmala, M. D. Giovannantonio, U. Diebold, K. Wandelt, and C. Goletti, "In situ scanning tunneling microscopy study of Ca-modified rutile TiO2(110) in bulk water," *Beilstein J. Nanotechnol.*, vol. 6, no. 1, pp. 438–443, 2015.

[195] L. E. David, N. C. MacDonald, P. W. Palmberg, G. E. Riach, and R. E. Weber, *Handbook of Auger Electron Spectroscopy.* Physical Electronics Division, Perkin-Elmer Corporation, second ed., 1976.

[196] K. Onda, B. Li, and H. Petek, "Two-photon photoemission spectroscopy of TiO2(110) surfaces modified by defects and O2 or H2O adsorbates," *Phys. Rev. B - Condens. Matter Mater. Phys.*, vol. 70, no. 4, pp. 1–11, 2004.

[197] V. Mansfeldova, M. Zlamalova, H. Tarabkova, P. Janda, M. Vorokhta, L. Piliai, and L. Kavan, "Work Function of TiO2(Anatase, Rutile, and Brookite) Single Crystals: Effects of the Environment," *J. Phys. Chem. C*, vol. 2, 2021.

[198] K. D. Schierbaum, S. Fischer, M. C. Torquemada, J. L. De Segovia, E. Román, and J. A. Martín-Gago, "The interaction of Pt with TiO2(110) surfaces: A comparative XPS, UPS, ISS, and ESD study," *Surf. Sci.*, vol. 345, no. 3, pp. 261–273, 1996.

[199] S. Facsko, T. Dekorsy, C. Koerdt, C. Trappe, H. Kurz, A. Vogt, and H. L. Hartnagel, "Formation of ordered nanoscale semiconductor dots by ion sputtering," *Science (80-.).*, vol. 285, no. 5433, pp. 1551–1553, 1999.

[200] M. R. McCartney and D. J. Smith, "Studies of electron irradiation and annealing effects on TiO2 surfaces in ultrahigh vacuum using high-resolution electron microscopy," *Surf. Sci.*, vol. 250, no. 1-3, pp. 169–178, 1991.

[201] A. K. See and R. A. Bartynski, "Inverse photoemission study of the defective TiO2(110) surface," *J. Vac. Sci. Technol. A*, vol. 2, no. February 1992, 1998.

[202] A. Nakamura, K. Matsunaga, J. Tohma, T. Yamamoto, and Y. Ikuhara, "Conducting nanowires in insulating ceramics," *Nat. Mater.*, vol. 2, no. 7, pp. 453–456, 2003.

[203] S. Hashimoto and A. Tanaka, "Alteration of Ti 2p XPS spectrum for titanium oxide by low-energy Ar ion bombardment," *Surf. Interface Anal.*, vol. 34, no. 1, pp. 262–265, 2002.

[204] M. A. Henderson, "Mechanism for the bulk-assisted reoxidation of ion sputtered TiO2 surfaces: diffusion of oxygen to the surface or titanium to the bulk?," *Surf. Sci.*, vol. 343, no. 1-2, 1995.

[205] M. K. Nowotny, T. Bak, and J. Nowotny, "Electrical properties and defect chemistry of TiO2 single crystal. I. Electrical conductivity," *J. Phys. Chem. B*, vol. 110, no. 33, pp. 16292–16301, 2006.

[206] C. Lun Pang, R. Lindsay, and G. Thornton, "Chemical reactions on rutile TiO2(110)," *Chem. Soc. Rev.*, vol. 37, no. 10, pp. 2328–2353, 2008.

[207] H. H. Pieper, K. Venkataramani, S. Torbrugge, S. Bahr, J. V. Lauritsen, F. Besenbacher, A. Kuhnle, and M. Reichling, "Unravelling the atomic structure of cross-linked (1 x 2) TiO 2(110)," *Phys. Chem. Chem. Phys.*, vol. 12, no. 39, pp. 12436–12441, 2010.

[208] S. Wendt, R. Schaub, J. Matthiesen, E. K. Vestergaard, E. Wahlström, M. D. Rasmussen, P. Thostrup, L. M. Molina, E. Lægsgaard, I. Stensgaard, B. Hammer, and F. Besenbacher, "Oxygen vacancies on TiO2(1 1 0) and their interaction with H2O and O2: A combined high-resolution STM and DFT study," *Surf. Sci.*, vol. 598, no. 1-3, pp. 226–245, 2005.

[209] R. Schaub, P. Thostrup, N. Lopez, E. Lægsgaard, I. Stensgaard, J. K. Nørskov, and F. Besenbacher, "Oxygen vacancies as active sites for water dissociation on rutile TiO2(110)," *Phys. Rev. Lett.*, vol. 87, no. 26, pp. 266104–1–266104–4, 2001.

[210] F. Rieboldt, L. B. Vilhelmsen, S. Koust, J. V. Lauritsen, S. Helveg, L. Lammich, F. Besenbacher, B. Hammer, and S. Wendt, "Nucleation and growth of Pt nanoparticles on reduced and oxidized rutile TiO2 (110)," *J. Chem. Phys.*, vol. 141, no. 21, 2014.

[211] Z. T. Wang, Y. G. Wang, R. Mu, Y. Yoon, A. Dahal, G. K. Schenter, V. A. Glezakou, R. Rousseau, I. Lyubinetsky, and Z. Dohnálek, "Probing equilibrium of molecular and deprotonated water on TiO2(110)," *Proc. Natl. Acad. Sci. U. S. A.*, vol. 114, no. 8, pp. 1801–1805, 2017.

[212] A. Borodin and M. Reichling, "Characterizing TiO2(110) surface states by their work function," *Phys. Chem. Chem. Phys.*, vol. 13, no. 34, pp. 15442–15447, 2011.

[213] H. Onishi, T. Aruga, and C. Egawa, "Adsorption of CH3OH, HCOOH and SO2 on TiO2(110) and stepped TiO2(441) surfaces," *Surf. Sci.*, vol. 193, pp. 33–46, 1988.

[214] P. Gorai, A. G. Hollister, K. Pangan-Okimoto, and E. G. Seebauer, "Kinetics of oxygen interstitial injection and lattice exchange in rutile TiO2," *Appl. Phys. Lett.*, vol. 104, no. 19, pp. 2–6, 2014.

[215] F. Silly, D. T. Newell, and M. R. Castell, "SrTiO3(0 0 1) reconstructions: the (2 × 2) to c(4 × 4) transition," *Surf. Sci.*, vol. 600, no. 17, pp. 219–223, 2006.

[216] T. Kubo and H. Nozoye, "Surface structure of SrTiO3(1 0 0)," *Surf. Sci.*, vol. 542, no. 3, pp. 177–191, 2003.

[217] D. M. Kienzle, A. E. Becerra-Toledo, and L. D. Marks, "Vacant-site octahedral tilings on SrTiO3 (001), the (sqrt13×sqrt13)R33.7° surface, and related structures," *Phys. Rev. Lett.*, vol. 106, no. 17, pp. 27–30, 2011.

[218] M. B. Hesselberth, S. J. Van Der Molen, and J. Aarts, "The surface structure of SrTiO3 at high temperatures under influence of oxygen," *Appl. Phys. Lett.*, vol. 104, no. 5, 2014.

[219] M. S. Martin Gonzalez, M. H. Aguirre, E. Moran, M. A. Alario-Franco, V. Perez-Dieste, J. Avila, and M. C. Asensio, "In situ reduction of (100) SrTiO3," *Solid State Sci.*, vol. 2, no. 5, pp. 519–524, 2000.

[220] J. E. Andersen and P. J. Møller, "Impurity-induced 900 °C (2×2) surface reconstruction of SrTiO3(100)," *Appl. Phys. Lett.*, vol. 56, no. 19, pp. 1847–1849, 1990.

[221] T. Ma, R. Jacobs, J. Booske, and D. Morgan, "Understanding the interplay of surface structure and work function in oxides: A case study on SrTiO3," *APL Mater.*, vol. 8, no. 7, 2020.

[222] W. Maus-Friedrichs, M. Frerichs, A. Gunhold, S. Krischok, V. Kempter, and G. Bihlmayer, "The characterization of SrTiO3(0 0 1) with MIES, UPS(HeI) and first-principles calculations," *Surf. Sci.*, vol. 515, no. 2-3, pp. 499–506, 2002.

[223] T. Susaki, A. Makishima, and H. Hosono, "Work function engineering via LaAlO3/SrTiO3 polar interfaces," *Phys. Rev. B - Condens. Matter Mater. Phys.*, vol. 84, no. 11, pp. 2–6, 2011.

[224] D. Wrana, K. Cieślik, W. Belza, C. Rodenbücher, K. Szot, and F. Krok, "Kelvin probe force microscopy work function characterization of transition metal oxide crystals under ongoing reduction and oxidation," *Beilstein J. Nanotechnol.*, vol. 10, 2019.

[225] Z. Chen, W. Zhong, Z. Liang, W. Li, W. Li, G. He, Y. Wang, Y. Xie, and Q. He, "Photocatalytic activity enhancement of anatase TiO2 by using TiO," *J. Nanomater.*, vol. 2014, 2014.

[226] A. Imanishi, E. Tsuji, and Y. Nakato, "Dependence of the work function of TiO2 (Rutile) on crystal faces, studied by a scanning auger microprobe," *J. Phys. Chem. C*, vol. 111, no. 5, pp. 2128–2132, 2007.

[227] Y. W. Chung and W. B. Weissbard, "Surface spectroscopy studies of the SrTiO3 (100) surface and the platinum-SrTiO3 (100) interface," *Phys. Rev. B*, vol. 20, no. 8, pp. 3456–3461, 1979.

[228] S. Sadewasser, T. Glatzel, M. Rusu, A. Jäger-Waldau, and M. C. Lux-Steiner, "High-resolution work function imaging of single grains of semiconductor surfaces," *Appl. Phys. Lett.*, vol. 80, no. 16, pp. 2979–2981, 2002.

[229] A. Rothschild, A. Levakov, Y. Shapira, N. Ashkenasy, and Y. Komem, "Surface photovoltage spectroscopy study of reduced and oxidized nanocrystalline TiO2 films," *Surf. Sci.*, vol. 532-535, pp. 456–460, 2003.

[230] H. Kim and D. W. Kim, "Transport characteristics and surface potential distribution of electrically stressed TiO2 single crystals," *Appl. Phys. A Mater. Sci. Process.*, vol. 102, no. 4, pp. 949–953, 2011.

[231] R. Meyer, R. Waser, J. Helmbold, and G. Borchardt, "Cationic surface segregation in donor-doped SrTiO3 under oxidizing conditions," *J. Electroceramics*, vol. 9, no. 2, pp. 101–110, 2002.

[232] Y. Chen, W. Jung, Z. Cai, J. J. Kim, H. L. Tuller, and B. Yildiz, "Impact of Sr segregation on the electronic structure and oxygen reduction activity of SrTi1-xFexO3 surfaces," *Energy Environ. Sci.*, vol. 5, no. 7, pp. 7979–7988, 2012.

[233] Y. Yu, K. F. Ludwig, J. C. Woicik, S. Gopalan, U. B. Pal, T. C. Kaspar, and S. N. Basu, "Effect of Sr Content and Strain on Sr Surface Segregation of La1-xSrxCo0.2Fe0.8O3-δ as Cathode Material for Solid Oxide Fuel Cells," *ACS Appl. Mater. Interfaces*, vol. 8, no. 40, pp. 26704–26711, 2016.

[234] A. Gunhold, K. Gömann, L. Beuermann, M. Frerichs, G. Borchardt, V. Kempter, and W. Maus-Friedrichs, "Geometric structure and chemical composition of SrTiO3 surfaces heated under oxidizing and reducing conditions," *Surf. Sci.*, vol. 507-510, pp. 447–452, 2002.

[235] K. Szot and W. Speier, "Surfaces of reduced and oxidized SrTiO3 from atomic force microscopy," *Phys. Rev. B - Condens. Matter Mater. Phys.*, vol. 60, no. 8, pp. 5909–5926, 1999.

[236] A. Kazimirov, D. M. Goodner, M. J. Bedzyk, J. Bai, and C. R. Hubbard, "X-ray surface diffraction analysis of structural transformations on the (0 0 1) surface of oxidized SrTiO3," *Surf. Sci.*, vol. 492, no. 1-2, 2001.

[237] K. Szot, W. Speier, U. Breuer, R. Meyer, J. Szade, and R. Waser, "Formation of microcrystals on the (100) surface of SrTiO3 at elevated temperatures," *Surf. Sci.*, vol. 460, no. 1-3, pp. 112–128, 2000.

[238] B. Koo, K. Kim, J. K. Kim, H. Kwon, J. W. Han, and W. C. Jung, "Sr Segregation in Perovskite Oxides: Why It Happens and How It Exists," *Joule*, vol. 2, no. 8, pp. 1476–1499, 2018.

[239] Y. Liang and D. A. Bonnell, "Atomic structures of reduced SrTiO3(001) surfaces," *Surf. Sci.*, vol. 285, no. 3, pp. 510–516, 1993.

[240] N. Erdman and L. D. Marks, "SrTiO3(0 0 1) surface structures under oxidizing conditions," *Surf. Sci.*, vol. 526, no. 1-2, pp. 107–114, 2003.

[241] T. Nishimura, A. Ikeda, H. Namba, T. Morishita, and Y. Kido, "Structure change of TiO2-terminated SrTiO3(001) surfaces by annealing in O2 atmosphere and ultrahigh vacuum," *Surf. Sci.*, vol. 421, no. 3, pp. 273–278, 1999.

[242] S. Witek, D. M. Smyth, and H. Piclub, "Variability of the Sr/Ti Ratio in SrTiO3," *J. Am. Ceram. Soc.*, vol. 67, no. 5, pp. 372–375, 1984.

[243] G. J. McCarthy, W. B. White, and R. Roy, "Phase Equilibria in the 1375 ° C Isotherm of the System Sr - Ti - 0," *J. Am. Ceram. Soc.*, vol. 52, no. 9, 1969.

[244] K. Szot, W. Speier, J. Herion, and F. Ch., "Restucturing of the surface region in SrTiO3," *Appl. Phys. A*, vol. 64, no. 4, pp. 55–59, 1997.

[245] D. A. Wright, "Work function and energy levels in insulators," *Proc. Phys. Soc.*, vol. 60, no. 1, pp. 13–22, 1948.

[246] N. A. Surplice, "The electrical conductivity of calcium and strontium oxides," *Br. J. Appl. Phys.*, vol. 17, no. 2, pp. 175–180, 1966.

[247] D. Wrana, T. Gensch, B. R. Jany, K. Cieślik, C. Rodenbücher, G. Cempura, A. Kruk, and F. Krok, "Photoluminescence imaging of defects in TiO2: The influence of grain boundaries and doping on charge carrier dynamics," *Appl. Surf. Sci.*, vol. 569, no. August, 2021.

[248] W. Belza, K. Szajna, M. Kratzer, D. Wrana, K. Cieslik, M. Krawiec, C. Teichert, and F. Krok, "Molecular Structure and Electronic Properties of para-Hexaphenyl Monolayer on Atomically Flat Rutile TiO2(110)," *J. Phys. Chem. C*, vol. 124, no. 10, 2020.

Appendix: Academic achievements

Parts of the results obtained during the PhD programme were published in the following publications and presented at conferences in the form of oral presentations and one poster.

- **K. Cieślik**, D. Wrana, K. Szajna, W. Bełza, M. Rogala, C. Rodenbücher, P. Dąbczyński, K. Szot and F. Krok Tuning the electronic properties by repeated sputtering and annealing of clean $TiO_2(110)$ surface: a KPFM and LC-AFM study, *Appl. Surf. Sci.*, vol. 571, no. September 2021, 2022 [101];
- D. Wrana, T. Gensch, B. J. Jany, **K. Cieślik**, C. Rodenbucher, G. Cempura, A. Kruk and F. Krok, Photoluminescence imaging of defects in TiO_2: The influence of grain boundaries and doping on charge carrier dynamics, *Appl. Surf. Sci.*, vol. 569, no. August 2021 [247];
- W. Belza, K. Szajna, M. Kratzer, D. Wrana, **K. Cieślik**, M. Krawiec, C. Teichert and F. Krok., Molecular Structure and Electronic Properties of para-Hexaphenyl Monolayer on Atomically Flat Rutile $TiO_2(110)$. *J. Phys. Chem. C*, col. 124, no 10, 2020 [248];
- D. Wrana, **K. Cieślik**, W. Belza, C. Rodenbücher, K. Szot and F. Krok, Kelvin probe force microscopy work function characterization of transition metal oxide crystals under ongoing reduction and oxidation, *Beilstein J. Nanotechnol.* vol 10, (2019). [224].

Table 1: List of conferences at which I presented the results of investigations in the form of an oral presentation.

Date	Place	Conference	Title of contribution
12.2021	virtual	Physics and Chemistry of Advanced Materials Seminar	Tuning the electronic properties of TiO2(110) surface by repeated sputtering and annealing
06.2021	virtual	NanoTech Poland – 11th International Conference	Tuning the electronic properties by repeated sputtering and annealing of clean TiO2(110) surface: a KPFM and LC-AFM study
08.2019	Regensburg	The 22nd International Conference on Non-contact Atomic Force Microscopy	Sputtering and annealing impact on the electronic properties of TiO2(110) surface: a KPFM and LC-AFM study
07.2019	Malmö	21st International Vacuum Conference	Self-formation of heterogeneous nanostructures on transition metal oxide perovskite surfaces by thermal reduction and incongruent sublimation
12.2018	Zakopane	X Seminarium NANOSAM	Badanie stabilności struktur molekularnych para-heksafenylu na powierzchni (110) TiO2 metodą spektroskopii termicznej desorpcji (TDS)

Table 2: Conference on which I presented the results of investigations in a form of a poster.

Date	Place	Conference	Title of contribution
08.2021	virtual	Nanotechnology and Innovation in the Baltic Sea Region 2021	Modification of the electronic properties of the TiO2(110) surface by sputtering and annealing